PETROLOGY OF ULTRAMAFIC AND RELATED ROCKS ALONG IRAQI ZAGROS THRUST ZONE

A Thesis

Submitted to the Council of the Faculty of Science, Graduate School of Science, Osaka Prefecture University, in Partial Fulfillment of the Requirements for the Degree of

Doctor of Science (D.Sc)
In
Geology

By

YOUSIF OSMAN MOHAMMAD

Supervised by

Prof. Dr. HIROKAZU MAEKAWA

May, 2008

I certify that this thesis was prepared under my supervision at Osaka Prefecture University, Faculty of Science, Graduated School of Science, as a partial requirements for the Degree of Doctor of Science in Igneous and Metamorphic Petrology.

Signature:
Supervisor: Professor Dr. H. Maekawa
Date:

In the view of available recommendation I forward this thesis for debate by examining committee.

Signature:
Supervisor: Prof. Dr. Satoshi Tanaka
Head of the Departmental
Committee on the Graduate
Studies in Physical Science
Date:

We certify that we read this thesis and as examining committee examined the student in its contents and that in our adequate with Excellent standing as a thesis for the degree of Doctor of Science in Geology / Igneous and Metamorphic Petrology.

Signature:
Name: Prof. Dr. Hideo Ogawa
Date:

Signature:
Name: Prof. Dr. Kazuhiko Ishii
Date:

Signature:
Name: Prof. Dr. Satoshi Tanaka
Date:

Signature:
Name: Prof. Dr.Hirokazu Maekawa
Date:

Approved for the faculty committee of graduate school of Science.

Signature:
Name: Prof. Dr. Yoshihiro Teraoka
Dean of the Faculty of Science
Date:

Acknowledgements

I would like to thank my supervisor Professor H. Maekawa for his support and wisdom throughout the years of study. I have learn more than I ever thought imaginable. I will never forget the skills you made me learn on my own. Ministry of Higher Education and Scientific Research of Kurdistan Regional Government are highly appreciated for covering my expense during the entire time of this study.

I would like to offer special thanks to Prof. Dr Kazuhiko Ishii, Prof Dr. Hideo Ogawa, and Prof. Dr. Satoshi Tanaka for their discussions and comments.

Many thanks to my wonderful family who helped me through the hardest of times to make it to where I am today:
Father and Mother: You are factory of graet persons. I love you lots!
Brothers and sister: You have been so supportive of me these past three years; I couldn't have done it without you! Thank you!

Many thank to my wife family for taking care of her instead of me, while I was busy with my study.

I hope we all keep in touch and never forget what a great experience this was!

ABSTRACT

Four main ultramafic rock bodies are distributed along the Iraqi Zagros Thrust Zone. They are Penjwin, Mawat, Pauza, and Qalander ultramafic bodies, in the order from southeast to northeast. They are typical lithological markers of the suture zone between Arabian and Iranian plates. Mineralogical and petrological investigation of Iraqi Zagros Thrust Zone peridotites indicates that they are mantle tectonite, rather than cumulate or replacive rock. They are mainly depleted harzburgite and dunite, along with restricted occurrence of spinel lherzolite to the Pauza ultramafic body, and consist of olivine, diopside, enstatite, spinel, serpentine, amphibole, and chromian chlorite. In dunite and harzburgite chromian spinel occurs as a coarse subhedral to euhedral grain. Chromian spinel in dunite commonly has Cr-rich core and Cr-poor ones. Chromian spinel in harzburgite rarely shows peculiar zoning of Cr-rich core and Al-rich rim. The lherzolite contains aluminous spinel which occurs as fine subhedral to anhedral grains with lobate boundaries.

On the basis of their Cr# [Cr# = Cr/ (Cr + Al)] of spinel, the spinels in lherzolite are chemically analogous to those from abyssal peridotites, whereas the chromian spinels in dunite and harzburgite resemble those from arc-related peridotites. Variations of mineral modal proportions and mineral chemistry; in addition low TiO_2 contents of spinel in lherzolite with gradual linear increasing of TiO_2 in spinels toward harzburgite and dunite, are consisting with 15 %, 30%, and more than 40 % partial melting for spinel lherzolite, harzburgite and dunite, respectively.

For the first time, albitite was found in the Iraqi Zagros thrust zone near the village of Mlakawa, 60 km northeast of Sulaimani City, Kurdistan region, northeastern Iraq. It occurs as a white pod within the massive tectonized and serpentinitized part of Penjwin ophiolite sequence. The preserved texture and mineralogical, petrological, and geochemical data from the core of the albitite pod suggest that protolith of Mlakawa

albitite is plagiogranite. It has undergone rodingitization and blackwall formation along its rim.

The occurrence of barium aluminoslicate (celsian), cymrite, barium muscovite, and a high Na_2O concentration (11 wt.%) of albitite suggests that barium-sodium-rich fluid was involved during the albitization process of plagiogranite. Evidence of the progressive albitization includes the metasomatic replacement of Ca-plagioclase to albite and grossular, celsian to cymrite, replacement of tremolite by edenite, and new formation of sheaf-like barium muscovite. The presence of analcime and multiple generations of chlorite suggest that the albitite protolith was accompanied by chloritization and retrograde metamorphism before and after the albitization process.

Ca-amphibole thermobarometry and modes of occurrence of polygenetic metamorphic titanite, along with the occurrence of strontium apatite and cymrite, suggest that the albitization of plagiogranite occurred at < 650 °C and 1.5 GPa.

CONTENTS

List of figures

List of tables

Chapter 1

Background, Aim, and Methodology

1 BACKGROUND

1-1 Ultramafic rocks

Ultramafic rocks have received considerable attention in recent years, in part because some of them are considered to represent samples of normally inaccessible mantle. Ultramafic rocks characterized by high magnesian olivine (Mg_2SiO_4) and low SiO_2 content (less than 45 wt. %) are found in a variety of igneous environments throughout the world. Most ultramafic rocks have characteristics as either plutonic igneous rocks or metamorphic rocks. Those found in the crust include both igneous and metamorphic types, whereas those from the mantle are metamorphic. Many ultramafic rocks presently exposed at the Earth's surface have been mildly to extremely recrystallized or serpentinized during tectonic emplacement or uplift.

The major goals in the study of ultramafic rocks are to understand the process of how the Earth mantle develops, how it contributes to the formation of the crust and what such rocks can tell us about tectonic process. Interpretation of ultramafic rocks and their origins requires mineralogical, chemical, and structural investigation as well as an understanding of the compositional variations that occur in association with mantle melts and magmatism in different environments. Ultramafics, ranging in composition from dunite through harzburgite to lherzolite, tend to exhibit either cumulate, tectonite (Raymond, 2002) or replacive texture (Kubo, 2002).

Olivine and pyroxene are the principal mineralogical components in most unmetamorphosed ultramafic rocks. Olivine $(Mg, Fe)_2SiO_4$ is an orthorhombic nesosilicate mineral with high birefringence and distinctive fracturing, often associated with high temperature crystallization (Nesse, 1999). Pyroxene is a group of important rock-forming inosilicate minerals. It shares common structure composed of single chains of silica tetrahedral and crystallizes in monoclinic and orthorhombic systems. Pyroxenes have a general formula $XY(Si, Al)_2O_6$ [where X represents Ca, Na, Fe^{2+}, Mg, and

more rarely Zn, Mn, and Li; and Y represents ion of smaller size such as Cr, Al, Fe^{3+}, Mg, Mn, Ti, V and even Fe^{2+}].

1-1-1 Mode of occurrence of ultramafic rocks

In the crust, ultramafic rocks are presented mainly in six major kinds. These are (1) layered igneous bodies, (2) zoned to irregularly shaped intrusion, (3) ultramafic lava flows (komatiites) and their differentiates, (4) kimberlite pipes and related intrusives, (5) Alpine type ultramafic rock bodies, and (6) nodules (including xenolith) in volcanic rocks. The major ultramafic bodies assigned to the one of two major groups, the layered and zoned to irregular bodies. Layered bodies include ophiolites. Zoned to irregularly shaped bodies include Alaska-type zoned complex and appinite-type ultramafic bodies. Each of these types has distinctive chemical, structural, and petrographic characteristics. These characteristics distinguish the individual type of ultramafic body, one from the other, as well as igneous bodies from metamorphic ultramafic rock bodies.

The common metamorphic bodies of the crust are signed to the category of alpine-type ultramafic bodies, which are found commonly as irregular to elliptical bodies in mountain belts. The rocks in these bodies may have been formed initially as magmatic crystal cumulates, crystallized or recrystallized from mantle diapirs, and mantle tectonite. They are emplaced as mantle slab into the crust by faulting. Alpine-type ultramafic rocks in general have tectonic fabrics, and are characterized by olivines and orthopyroxenes with moderate to high Mg number. The rock bodies lack chilled margin and do not give circumference contact metamorphism. Perhaps more than other ultramafic bodies, alpine-type ultramafic rocks have severly undergone serpentinization.

Alpine-type ultramafic rocks of crustal heritage may reveal the early histories of intrusion and crystallization, metamorphism, and deformation in the mountain belts as well as a synorogenic history, which also portrayed by the texture, structure, and minerals of the more common

rocks of the belt. These attributes provide an ample incentive for the study of alpine-type ultramafic rocks.

1-1-2 Genetic classification of ultramafic rocks

1-1-2-1 Cumulate ultramafics

Cumulate ultramafics, typically dunites or pyroxenites, can form in layered intrusions as the bottommost "strata" of a fractionally crystallized melt (Winter, 2001). In a slowly cooling magma chamber, heavy crystallized minerals settle at the bottom of the chamber and accumulate much like sediment settling out of the water column in a pond. Because olivine is heavier and tends to crystallize at higher temperatures, it is more likely to fractionally crystallize out of a magma in the early stages of cooling, forming a layer of cumulate olivine crystals on the magma chamber floor (Winter, 2001). Some of the best examples of cumulate ultramafics in layered intrusions can be found in the ultramafic series of the Stillwater Complex in southwestern Montana. In these series, layers of olivine and chromian spinel are overlain by layers of olivine mixed with orthopyroxene, grading upward into orthoproxenite, and eventually into orthopyroxene and plagioclase (Winter, 2001). This succession of compositionally distinct layers grading upward from silica-poor minerals to silica-rich minerals represents a pattern in the cooling of mafic magmas which forms ostensibly stratified igneous plutons when exposed (Wyllie 1967, Winter, 2001, Buming et. al., 1997).

1-1-2-2 Tectonite ultramafics

Mantle tectonite is a type of non-cumulate ultramafic rock often interpreted as an exposed fragment of primary or depleted mantle, which has been tectonically emplaced on the surface of the earth. These rocks are often associated with the basal layer of ophiolite; rocks interpreted as exposed sequence of oceanic plate emplaced on the surface of the Earth as a result of tectonic collision and thrust faulting (Winter, 2001).

Typical ophiolite sequences are composed of a thin layer of deep-sea sediments, overlying a sequence of basaltic pillow lavas, sheeted dike complexes, foliated to layered gabbro, and finally an ultramafic complex, which can have an exposed thickness of up to 7 km. This ultramafic section of ophiloite can vary in composition, however, it is most commonly dominated by varieties of peridotite typically associated with the mantle such as harzburgite (olivine and orthopyroxene rich), lherzolite (olvine, orthopyroxene, and clinopyroxene rich), and wehrlite (olivine and clinopyroxene rich), and dunite (olivine rich).

1-1-2-3 Replacive ultramafics

Another non-cumulate mechanism for the formation of ultramafic rocks involves the replacement of pyroxene minerals with olivine through chemical reactions between a silica-poor magma and a pyroxene-rich host rock (Kubo, 2002). This replacement occurs as the process that silica-poor magma rises through the mantle and saturates pyroxene-rich mantle lherzolite or harzburgite during its ascent. As silica-rich minerals generally have a lower melting temperature than silica-poor minerals, the pyroxene minerals are partially dissolved by the magma, leaving behind olivine in place of pyroxene (Kubo, 2002).

Because replacive processes have only recently been defined, there are few studies which focus on the extent to which replacement plays a role in the formation of dunites (Kubo, 2002). At this time, replacive processes are thought to occur most commonly in the transition zone of ophiolite sequences, between ultramafic tectonite and ultramafic cumulate units (Arai, 1994).

1-1-3 Metamorphism of ultramafics

Metamorphism of ultramafic rocks occurs both at depth and near the surface of the earth during tectonic uplift and emplacement. Because the mantle is under high lithostatic pressure, most mantle rocks have been partially metamorphosed even before their uplift and emplacement (Winter, 2001). Chemical alteration and metamorphism of rocks in the upper mantle are associated with partial melting, fractional crystallization of partially melted magmas, and localized ductile deformation. The primary metamorphic features are difficult to distinguish from features caused by subsequent metamorphism during exhumation stage. The distinctions, however, can be made by geochemical and petrologic analysis to reveal the presence or absence of high pressure mantle mineral fabrics and chemical compositions (Raymond, 2002, Gaetani et al, 1998, Jameieson, 1981). For example, olivine grains which were originally formed in the mantle would be expected to show evidence of ductile deformation. Therefore, the presence of undulatory extinction or zoning in large olivine grains in ultramafic tectonites is often interpreted as an indication of the absence of recrystallization. Accordingly, chemistry of olivine grains with undulatory extinction in ultramafic tectonites is often interpreted as reflecting the composition of the rocks as they existed in the mantle before exhumation (Winter, 2001, Raymond, 2002, Downes, 2001).

1-1-3-1 Serpentinization

Metamorphism of ultramafic rocks during uplift and emplacement commonly involves serpentinization, a process by which water is introduced into the system, causing recrystallization of ultramafic minerals into serpentine (Gaetani et. al, 1998). Serpentine $Mg_3Si_2O_5(OH)_4$ is a metamorphic phyllosilicate with monoclinic, triclinic, orthorhombic or hexagonal structure, depending on the mineral species and environment of crystallization. The three main varieties of serpentine are lizardite, chrysotile, and antigorite (Nesse, 1999). These species are practically

polymorphs; however slight chemical differences do distinguish them from one another (Winter, 2001; Mohammad and Maekawa, 2007). Antigorite, the most chemically and structurally distinct type within the three species, tends to be stable at higher temperatures than the other two phases of serpentine (Raymond, 2002; Mohammad and Maekawa, 2007). Because of their structural differences, quantitative x-ray diffraction can be used to distinguish the different varieties of serpentine present in a given body of rock.

Serpentinization often occurs within subduction zone because ocean water in a trench has the ability to seep down into the mantle wedge causing hydration of ultramafic minerals into serpentine. However, serpentinization also occurs on the ocean floor as a result of the reaction between ocean water and basalt formed at mid-ocean ridges (Winter, 2001, Gaetani et. al., 1998). Different degrees of serpentinization can occur even within a single rock body, with the highest degrees of metamorphism typically found in association with fractures and cracks, along which water can more easily travel (Gaetani et.al., 1998).

Serpentinization can be isochemical (constant chemistry) or allochemical (constant volume). During isochemical serpentinization, the bulk composition of the rock plus the introduced water is not changed. The isochemical serpentinization reaction between peridotite and water typically results in a net increase in volume because of the less structurally condensed nature of serpentine with respect to olivine and pyroxene. As a result of this volume increase, serpentinization can cause extensive internal fracturing within a rock body (see reaction 1). Allochemical serpentinization occurs as a constant volume process in which large positively charged ions such as Mg^{2+}, Ca^{2+}, Fe^{2+}, and Si^{4+}, are released into solution during the serpentinization process, and transported away by fluids (see reaction 2)

Reaction 1: Isochemical serpentinization

Olivine + silica in solution → Serpentinite

$3Mg_2SiO_4 + H_4SiO_4 + 2H_2O \rightarrow 2Mg_3Si_2O_5(OH)_4$

(131cc) introduced → (220cc)

(Raymond, 2002)

Reaction 2: Allochemical serpentinization

Olivine + water → serpentine + Mg ion + hydroxyl ion + silica in solution

$5Mg_2SiO_4 + 10H_2O \rightarrow 2Mg_3Si_2O_5(OH)_4 + 4Mg^{2+} + 8(OH) + H_4SiO_4$

(219 cc) introduced → (220 cc) removed in solution

(Raymond, 2002)

1-1-3-2 Ultrahigh-pressure metamorphism (UHP)

Recently exsolution microstructures in minerals have been identified in ultrahigh-pressure (UHP) ultramafic rocks from several orogenic belts including Western Gneiss Region, Norway; Alpe Arami, Switzerland; Centeral Sulawies, Indonesia; Dabie-Sulu UHP terrane in East-Centeral China (Smith, 1988; Dobrzhinetskaya et al., 1996; Harcker et al., 1997; Zhang and Liou 1998; Zhang et al., 1999). The most common exsolution features in olivine from UHP garnet peridotite are ilmenite lamella or rods; magnetite lamella is minor. Exsolution lamella in diopside includes K-feldspar, ilmenite, Mg-Al-Cr titanomagnetite, and garnet. Quartz lamellae is also found in both omphacite and diopside. Exsolution lamellae in garnet includes both Al-pyroxene and rutile rods. Exsolution lamellae in UHP minerals may have formed during nearly isothermal decompression, in contrast to exsolution with falling temperature in primary igneous minerals. Mineral exsolution from breakdown of a solid-solution phase is a subsolidus reaction. A principle characteristic of UHP solid-solution phases, such as majoritic garnet and supersilicic clinopyroxene, is the substitution of sixfold coordinated Si for Al, Fe and Mg in octahedral sites. For example, the tschermakite substitution of [2 Al

(+Cr)]VI by [M^{2+} Si^{4+}]VI, where M = Mg and Fe, occurs in majoritic garnet and [$Mg^{2+}Na^{1+}Al^{3+}$]VI-VIII by [$1.5Si^{4+}$] occur in supersilicic clinopyroxene. The effect of pressure drops on the genesis of exsolution lamellae, and significance of their occurrences need to be systematically investigated. Detailed characterization and experimental investigations regarding exsolution microstructures of these minerals in UHP rocks will improve our understanding of mantle processes and continental subduction.

1-2 Associated rocks with serpentinized ultramafic rocks

Rocks intimately associated with serpentinitized ultramafic rocks or found as inclusion in serpentinite are of quite different types and sizes, but are recognized as an integrated product of the serpentinization process; they are rodingite, jadeitite and albitite (e.g., Coleman, 1980, Harlow, 1994; Dubińska et al., 2004; Mohammad et al., 2007).

1-2-1 Rodingite

Rodingite is a Ca-rich, and SiO_2-undersaturated rock, consisting of Ca-Al and Ca-Mg silicates. It was formed by metasomatism of varied rock types during serpentinization of host peridotite (e.g., Coleman, 1977; Laech and Rodgers, 1978; Evans et al., 1979; Schandl et al., 1989; OHanley et al., 1992; Mohammad et al., 2007). The protolith of rodingite ranges from gabbro to quartzite (OHanley, 1996). Rodingite has been reported from several ophiolite complexs (e.g., Carpedri et al., 1978; Dubińska et al., 2004; Hatzipanagiotou and Tsikouras, 2001, Mohammad, 2004), as well as from Archean mafic sequences and present day ocean floors (Honnorez and Kirst, 1975; Anhaeusser, 1979; Schandle et at., 1989). In general rodingite is enveloped by chlorite shell labeled as blackwall (e.g., Forst, 1975; Laech and Rodgers, 1978; Evans et al., 1979; OHanley et al., 1992; OHanley, 1996; Mohammad et al., 2007).

1-2-2 Jadeitites

Jadeitite is composed principally of jadeite. It occurs either as individual tectonic blocks or as pods, lenses or veins in other blocks within serpentinite. Jadeitite is rare, described from a handful of localities: the Moguong and Lokin area of northern Maynmar (Chhibber, 1934); Kotakai District, Okayama Prefecture, Hokkaido, Japan (Osada et al., 2007); California (Coleman, 1961); the Pay-Yer massif, Polars Urals, Russia (Morkovkina, 1960); Kazakhstan (Dobretsov and Ponomareva, 1965) and Guatemala (Harlow, 1994). Jadeitite is archaeologically and commercially important as a jade.

1-2-3 Albitites

Albitite is a high-pressure and low-temperature metasomatic rock that occur as inclusions or pods in serpentinite. Albitite has received little attention due to rare occurrence. It consists almost entirely of albite and contains subordinate amounts of muscovite and quartz. Albitites are found in several geological settings, one of which is in association with ultramafic rocks of blueschist, and amphibolite to granulite facies. Albitites in high grade rocks are associated with quartz–plagioclase, plagioclase–tourmaline pegmatites, kayanite–biotite and corundum–tourmaline rocks. The mineralogical assemblages in albitite are arrayed in a zone parallel to the contact between the albitite protolith and serpentinized peridotite. Many of the origins of albitite have been discussed; the first is ascribed to the actions of metasomatic-hydrothermal fluid on the granitic rocks (Kovalenko, 1978, Cathelineau, 1988), the second is direct precipitations from solution (Harlow, 1994, Johnson and Harlow, 1999), the third is direct crystallization from Na-rich magma

(Schwartz, 1992), and the fourth action of barium-sodium-rich fluids on plagiogranite (Mohammad et al., 2007)

2- Aim of the study

In north and north-eastern Iraq, several serpentinized ultramafic and related rocks are exposed along the Iraqi Zagros Thrust Zone; they are from southeast to northesat, Penjwin, Mawat, Pauza and Qalander ultramafic bodies. These bodies are considered to have been fragments of consumed Thethyan oceanic lithosphere between Arabian and Iranian plates (Mahmmod, 1978; Al-Hassan, 1982; Aqrawi, 1990; Mohammad, 2004, Mohammad and Maekawa, 2007). However, on origin of these serpentiniteized ultramafic bodies, whether these serpentinized ultramafic bodies represent a remnant serpentinized peridotite of ophiolite sequences or serpentinized mantle wedge peridotite is still debated due to the absence of critical petrological and geochemical data.

This study tries to answer the following questions in regard to the serpentinzed peridotite and related rocks along Iraqi Zagros Thrust Zone:

1. What kind of mineralogical and petrological features characterize the serpentinized ultramafic bodies?
2. What types of ultramafic rocks are representative in serpentinized peridotite along the Iraqi Zagros Thrust Zone?
3. How were serpentinized peridotites emplaced in the present position?
4. What kind of tectonic settings were these bodies situated?
5. How did the serpentinization take place in the formation process of theses rocks?
6. What kinds of rocks are associated with the serpentinzed peridotites, and what are their mineralogy and origin?
7. What is the relation between serpentinization, rodingitization, and albitization processes during evolution of peridotite?

In combining the new data on the serpentiniteized peridotite can draw the picture of the overall evolution history of the Tethyian ocean lithosphere between Arabian and Iranian plates.

3- Methods of analysis

The serpentinized ultramafic bodies were studied in the field using normal interpretative mapping method and compass. In the laboratory, handspecimen-slab examination of the structure and thin section petrography were performed. Mineral compositions were determined by electron microprobe analysis. Analyses were made with a JEOL-840A scanning electron microscope, which is equipped with an Oxford energy-dispersive detector (EDX) analytical system (Link ISIS series L200I-S) at Osaka Prefecture University, operating at 15.0 kV and 0.5 nA. Raw data were ZAF corrected. Total iron was measured as FeO and was recalculated assuming ideal stoichiometry for FeO and Fe_2O_3 values. Whole-rock analyses for major and trace elements were done by ALSChemex Analytical Laboratories, Canada. Rare earth element (REE) analyses were done by Elan 6000 ICP-MS using the $LiBO_2$ fusion method. Mineral species identification for the serpentine mineral polymorphs lizardite, chrysotile, and antigorite was done by XRD and mXRD using a Rigaku RINT-RAPID diffractometer at the Department of Physical Science at Osaka Prefecture University

Chapter 2

Geology and Tectonic setting

2-1 Regional geology

The Iraq Zagros Thrust Zone in the north and northeastern Iraq represents a suture zone between the Arabian and Iranian plates to the northeast and the Turkish plate to the north. It occupies an area of about 5000 km^2 along the Turkey-Iraq-Iran border. The Iraqi Zagros Thrust Zone represents a part of the larger Zagros orogen belt which extends about 2000 km from southeastern Turkey through northern Syria and Iraq to western and southern Iran (Mohammad et al., 2007).

Bolton (1957) subdivided Iraqi Zagros thrust zone into four structural units from southwest to northeast as follows:

1. **Folded foreland zone**, about 200 km wide consisting of sedimentary rocks of Paleozoic to Tertiary and Quaternary ages.
2. **Transitional zone**, which is the site of accumulation of molasse sediments from marine to continental environments.
3. **Qulqula zone**, consisting of radiolarian mudstone, shale, thinly beded limestone.
4. **Thrust zone**, which is subdivided into three unit (Bolton, 1955, 1958), they are from bottom to top as follows:
    A. Naopurdan or Outer Zone (Palaeocene-Oligocene). It is represented by flysh sediment which was thrust over Qulqula serries without any dynamic metamorphism reaching a total thickness of 2000 m.
    B. Walash series or Intermediate Zone. It consists of three red bed units intercalated by two volcanic units, and is associated with some intraformational serpentinite bodies, with a total thickness of 3.7 km. The volcanic unit consists of metavolcanic spilite and andesite. The sedimentary beds are composed of red mudstone, siltstone, and shale.
    C. Qandil series or Inner Zone (Palaeocene-Eocene). It is represented by para-autochthons and regional metamorphic rocks (phyllite and calc-schist).

Buday (1973) studied the geology of north-eastern Iraq and divided it into:

1. Zagros thrust zone, which comprises both Inner zone and Outer zone, represented by Qandil unit, Qulqula and Walash-Naopurdan Series, respectively.
2. Imbricate zone, represented by Red Bed Series and eastern part of folded zone.

Buday and Jassim (1987) modified above bipartite subdivision of Buday (1973) into a tripartite subdivision on the basis of main sedimentary sequence, as follows:

1. External zone, which comprises both Balambo-Tanjero and the Northern thrust subzone represented by unmetamorphosed rocks that were deposited in miogeosynclinal depositional environment and affected by Laramide and Late-Alpine orogeny.
2. Central zone, represented by sediments of Mesozoic and Tertiary ages associated with volcanic activity, comprises both Qulqula – Khwakurk subzone and the Penjwin – Walash subzone.
3. Internal zone, composed of metamorphosed Cretaceous shale and volcano-sedimentary sequences.

Five ultramafic rock bodies occur as linear arrays in the Iraqi Zagros Thrust Zone. They are from southwest to northeast as follow, Penjwin ultramafic bodies, Mawat ultramafic bodies, Betwat serpentinized ultramafic bodies, Puza ultramafic bodies and Qalander serpentized ultramafic bodies (Fig. 2-1). We subdivide them according to the associated rocks into two groups (Mohammad and Meakawa, 2007). Ultramafic bodies associated with ophiolite rocks including both Mawat and Penjwin ultramafic rocks and isolated serpentinized peridotites including Pauza, Betwat and Qalander. Nowadays such linear array of metamorphosed ultramafic rocks is lithological marker of suture zone between plates within orogens (Ditez, 1963; Moores, 1981; Dewey and Bird, 1970; Brewer an Woodward, 1988; Adam et. al., 1995; Raymond et. al. 2001)

2-1-1 Geology of Penjwin area

2-1-1-1 Penjwin ophiolite

The Penjwin igneous complex represents an ophiolite sequence within the larger Zagros belt. It is a northwest-southeast trending elongated body (35 km^2) within the Iraqi territories. The remnant parts were located within adjacent Iranian territories (Mahmmod, 1978). The Penjwin ophiolite sequence is bounded on the east by phyllite and calc-schist of the Qandeil unit and on the west by the Merga Red Bed of the Tertiary Red Bed Series (Fig. 2-2). The Penjwin ophiolite sequence consists of alpine-type peridotite overlain by banded gabbro and diorite with a small dyke of pyroxenite. Field relations show that the complex is a continuous sequence from peridotite (dunite, harzburgite, websterite, and bronzitite) at the bottom, through amphibolitized gabbro, to diorite at the top. A large part of the ophiolite extends into the Iranian territories. The Penjwin igneous complex is separated from the Tertiary Red Bed Series to the west by a high angle reverse fault. The complex is in contact with metamorphosed limestone of the Qandiel unit at the northeastern end, and the boundary passes just south of the town of Penjwin.

2-1-1-2 Qandil sequence

Buday (1973) subdivided Qandil sequence into upper sedimentary Qandil unit and lower metamorphosed unit. The latter one is subdivided into an upper metamorphosed sedimentary Serginil unit and a lower metamorphosed volcano-sedimentary Gimo unit. Buday (1987) subdivided Gimo unit into two subunits, the upper one is metamorphosed volcano-sedimentary subunit and lower metavolcanic subunit. Volcano-sedimentary subunit comprises metabasalt, pillow lava interbeded with marbles, phyllite, and calc-schist. Meta-volcanic unit consists of olivine theolites and spilites metamorphosed to greenschist facies.

2-1-1-3 Red Bed Series

Red Bed Series consist of molasse sediments and is subdivided into four units :

1. **Suwais I** consists of fossiliferous, detrital, conglomeratic limestone. The unit is massive in lower part and iterbedded with shale in upper unit. The total thickness is 50 m.
2. **Suwais II** consists of red ferrogeneous siliceous, and slity shale with siltstone and conglomeratic beds which contain reworked Cretaceous fossils. The total thickness is 300 m.
3. **Suwais III** consists of coarse, partly cobble-sized cherty conglomerate. The total thickness is 350 m.
4. **Suwais IV** consists of red shale and sandstone, with reddish nummulitic limestone.

The **Suwais I** was deposited in shallow marine environment and the other three units were deposited in deltaic to fluviodelatic depositional environments.

2-1-2 Geology of Mawat - Chwarta area

2-1-2-1 Mawat Ophiolite

The Mawat igneous complex represents one of ophiolitic sequence within the Iraqi Zagros Thrust Zone. It shows north-south trending longitudinal shape (Fig. 2-3), with 25 km length and 7–12 km width. The complex consists of peridotite overlaid by banded gabbro and volcanic rocks. Peridotite is composed mostly of harzburgite and dunite. Some lherzolite pods are found in the harzburgite portion. It covers an area about 15 km^2 with total thickness of 1500 m. Different types of gabbro are recognized. They are pyroxene gabbro and banded gabbro. Pyroxene gabbro is restricted to the east part of the Mawat ophiolite sequence near the village

of Luta-Rash. Volcanic rocks are exposed to the north and south of the Mawat ophiolite sequence, and comprise spilitic basalt and metabasalt.

2-1-2-2 Walash – Nouprdan Group

Al-Mehidi (1975) subdivided the Walash-Nouprdan Group into two isolated rock units, which are Walash and Nouprdan Formations. Nouprdan Formation represents the outer zone of Mawat ophiolite sequence, with a total thickness of about 700 m. It consists of grayshale, graywake, and shaly limestone with some acidic and basic volcanic intrusions, of Plaeocene-Oligocene ages. Walash Formation consists of three red bed units intercalated by two volcanic ones, and the total thickness is 3700 m. Basal red bed unit consists of red mudstone, cherty limestone and shale, with lower volcanic unit of basic rocks, and is accompanied with a few acidic pillow lava. The middle red bed unit consists of red mudstone, shale, sandstone and conglomerate. The upper volcanic unit consists of metabasic rocks with a few andesitic lava; the upper red bed unit consists of red mudstone and clastic sediment, composed of conglomerates, siltstone and graywakes.

2-1-2-3 Betwat-Kunjren serpentinite belt

Betwat-Kunjren serpentinite belt represented by a chain of isolated serpentinite bodies extends from the village of Betwat toward north of the Mawat subdistrict. Isolate serpentinites of 500 m wide and 1 km long are aligned to form an array parallel to the main Mawat ophiolite body. It resprsents typical diapiric serpentinite in forearc tectonic setting (Mohammad and Maekawa, 2007). It consists of massive type serpentinite surrounded by metavolcanic rock unit of Walash Formation.

2-1-2-4 Gimo unit

Gimo unit is located in the northern part of Mawat ophiolite sequence. It consists of marble, and the total thickness is about 600 m at Gimo Mountain (Fig. 2-4)

2-1-3 Geology of Bulfat igneous complex

The Bulfat igneous complex is situated within the Iraqi Zagros Thrust Zone along Iraq-Iran border, covering an area of about 100 km^2 that straddles the Iran-Iraq border. The Bulfat igneous complex comprises mafic and ultramafic igneous rocks (Fig. 2-5). Mafic rock comprises four types as follow:

1. **Olivine gabbro** occupies about 26 vol.% of the Bulfat igneous complex by area. The large intrusion is characterized by gray to brownish gray color, and consist of fine to medium granulated plagioclase (67 vol.%, An_{57}–An_{72}), olivine (12 vol.%, Fo_{64}), and pyroxene (1–27 vol.%, $Wo_{45}En_{39}Fs_{16}$). Pyroxene contains two perpendicular sets of exsolution lamella of ilmenite, suggesting that the rock underwent ultrahigh-pressure metamorphism.
2. **Pyroxene gabbro** is restricted to high peaks along Iraqi-Iran border. It consists of coarse-grained pyroxene ($Wo_{50}En_{29}Fs_{20}$) and plagioclase (An_{52}–An_{77}).
3. **Pyroxene-amphibole gabbro** consists of medium grained plagioclase (An_{76}), amphibole, and uralitized pyroxene.
4. **Syenites, nepheline syenites**, and pegmatite gabbro are found in shear zones, forming dyke-like bodies.

The ultramafic rocks form about 8 vol. % of igneous rocks, always occupying southern and western margins of the Bulfat igneous complex. The ultramafic rocks can be divided into following two occurrences:

1. **Serpentinite belt** in the Bulfat area occurs as chain of isolated intraformational bodies of serpentinite within the volcano-sedimentary rock unit of the Walash-Nupordan Group (Fig. 2-5). It has a total thickness of 300–500 m, length of 1–1.5 km, and is surrounded on all sides by metavolcanic rocks of spilite, andesite,

and a sandstone unit of the Paleocene–Eocene Walsh Formation. It is highly probable that serpentinite belt in Bulfat area represents the extension of serpentinite chain in Mawat area.

2. **Pauza ultramafic body**: The Pauza ultramafic rocks form about 8 vol.% of the Bulfat igneous complex, occupying southern and western margins of the Bulfat complex. Pauza ultramafic rocks show layering, which could be inherited from primary igneous layering such as seen in layered cumulate, but also can be of metamorphic origin. The ultramafic body about 1 km thick and 1.5–2km wide has both lower and upper contacts. The contacts are chacterized by tectonic bericcia. In the field dunite either occur as podiform(30 × 40 cm in size) with spheroidal weathering or as tabular sills. Dunite occupies the upper part of Puzau ultramafic body, whereas the lower part consists of the harzburgite and lherzolite (mostly spinel lherzolite). Spinel lherzolite has characteristically contained coarse-grained clinopyroxene with garnet exsolution lamellae. The Pauza ultramafic body is cut by sills or vein of pyroxeneite and hornblendite with typical flow textures.

2-2 Regional tectonic setting

Zagros orogenic belt was formed by the collision of Eurasia Continent with dispersed fragments of Gondwana Continent (Arabian plate). It is interpreted as the product of three major sequential geotectonic events: (1) subduction of the Neo-Tethyan oceanic plate beneath the Iranian lithospheric plate during early to late Cretacouse time, (2) emplacement of a number of Neo-Tethyan oceanic slivers (ophiolites) over the Arabian continental margin in late Cretaceous (Turonian – Campanian) time, and (3) collision of Arabian plate with Iranian plate in Miocene. The Zagros orogen is bounded to the northwest

by the East Anatolian left-lateral strike slip fault and to the southeast by the Oman line. The orogen consists of three parallel belts (Fig. 2-6): (1) the Urumieh-Dokhtor Magmatic Assembalage (UDMA), which forms a distinct linear intrusive-extrusive complex, extends along the entire length of Zagros orogenic belt, with width of over 4 km. The UDMA comprises various lithologic units including gabbro, diorites, granodiorites and granite bodies of different size. It also contains widely distributed basaltic lava flow; (2) Zagros Imbricate Zone (ZIZ), which is a zone of thrust faults that have transported numerous slices of metamorphoses and non metamorphosed Phanerozoic stratigraphic unit of Arabian continental margin, as well as ophiolites, from the collisional suture zone on the northeast toward interior parts of the Arabian craton to the southwest. The ZIZ comprises both Sanandaj-Sirjan Zone (SSZ) in Iran and Iraqi Zagros Thrust Zone in Iraq; and (3) the Zagros fold-thrust belt, which forms the less strained part of the orogen, and consists of a pile of folded and faulted rocks composed of 4 to 7 kilometres of mainly Paleozoic and Mesozoic successions overlain by 3 to 5 kilometres of Cenozoic sliciclastic and carbonate rocks resting on highly metamorphosed Proterozoic Pan-African basement that was affected by the late Neoproterozoic-Cambrian Najd strike-slip faults (Alavi, 2004).

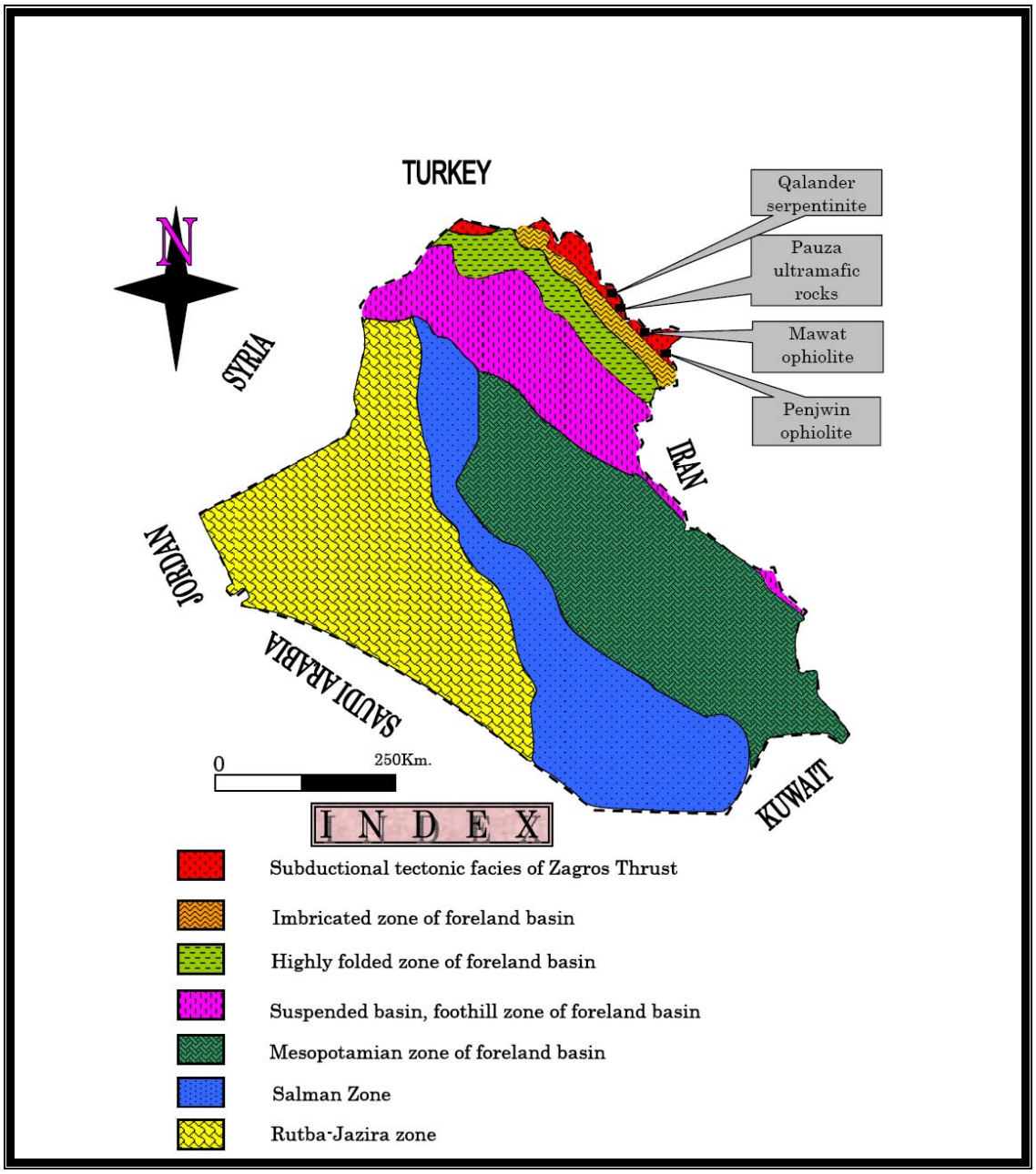

Fig. 2-1: Tectonic subdivision of Iraq (after Numan, 2001), showing the location of the serpentinized peridotite.

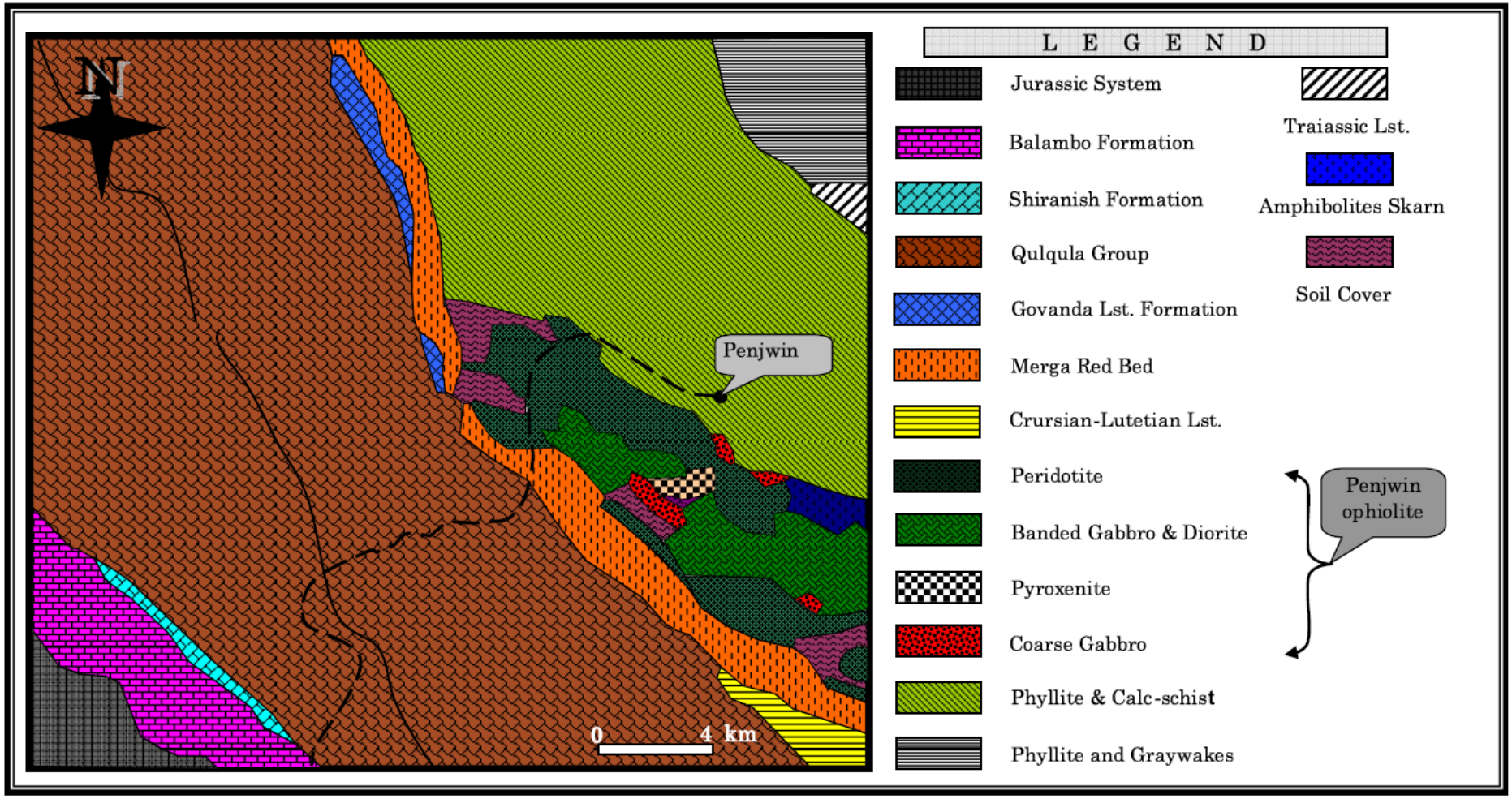

Fig. 2-2: Geological map of Penjwin area. Modified after Buday and Jassim, (1987). Lst-limestone

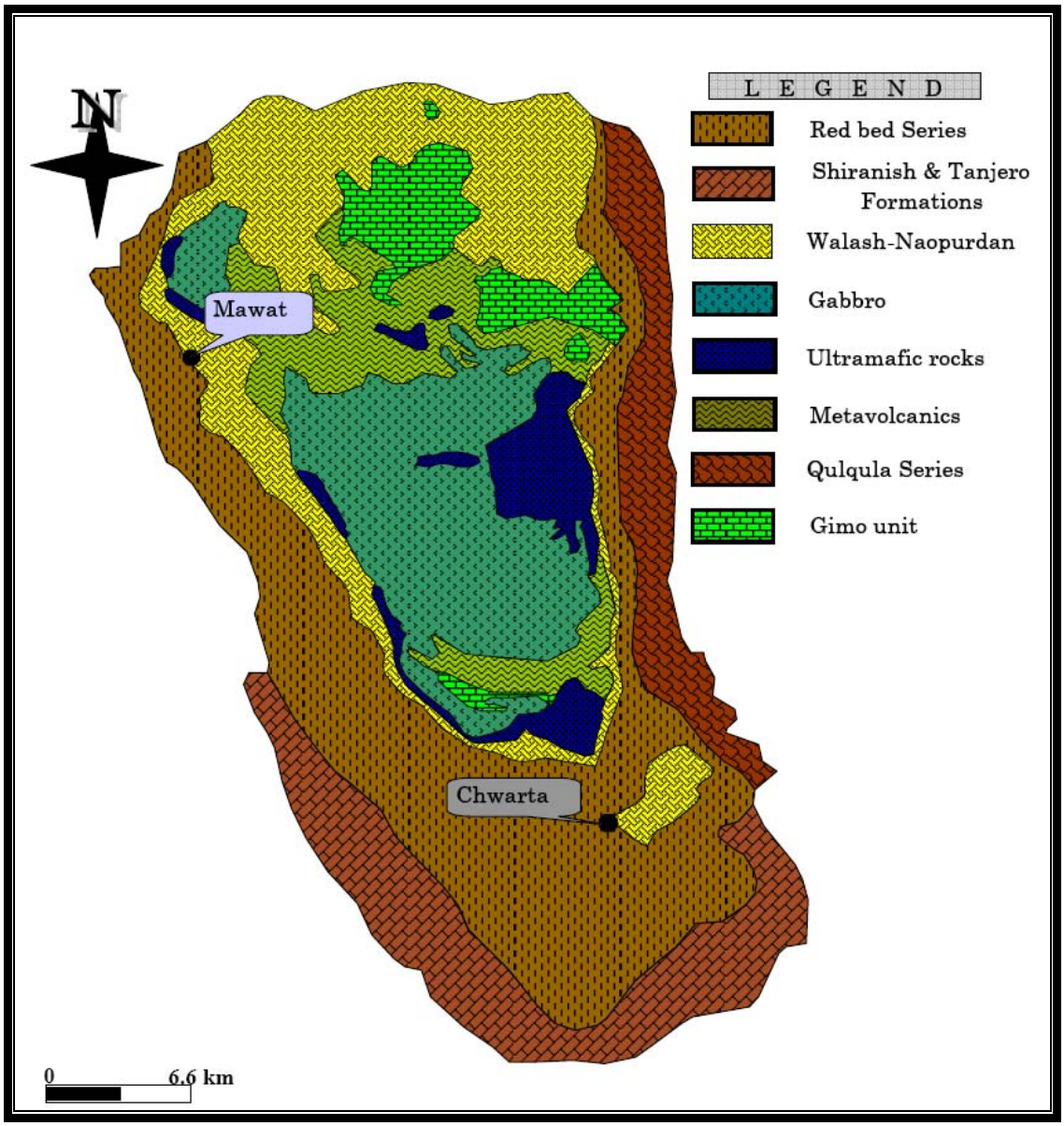

Fig. 2-3: Geological map of the Mawat-Chwarta areas. Modified after Al-Mehidi (1975).

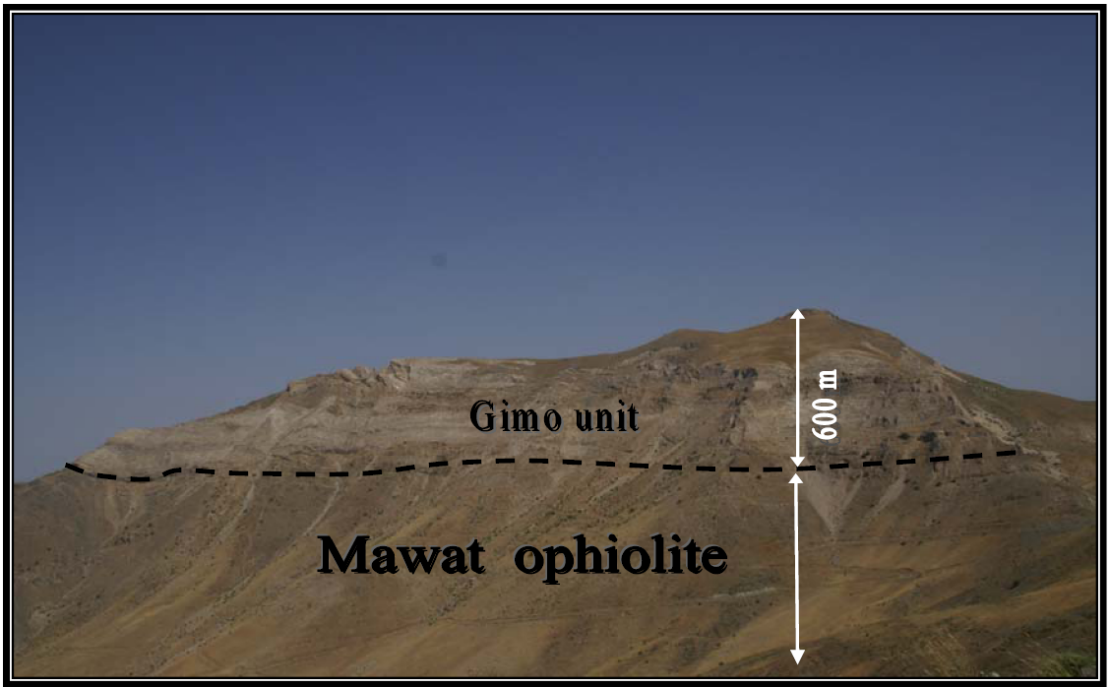

Fig. 2-4: Field photograph of Gimo unit of Qandiel Series occurs as a cap on the Mawat ophiolite.

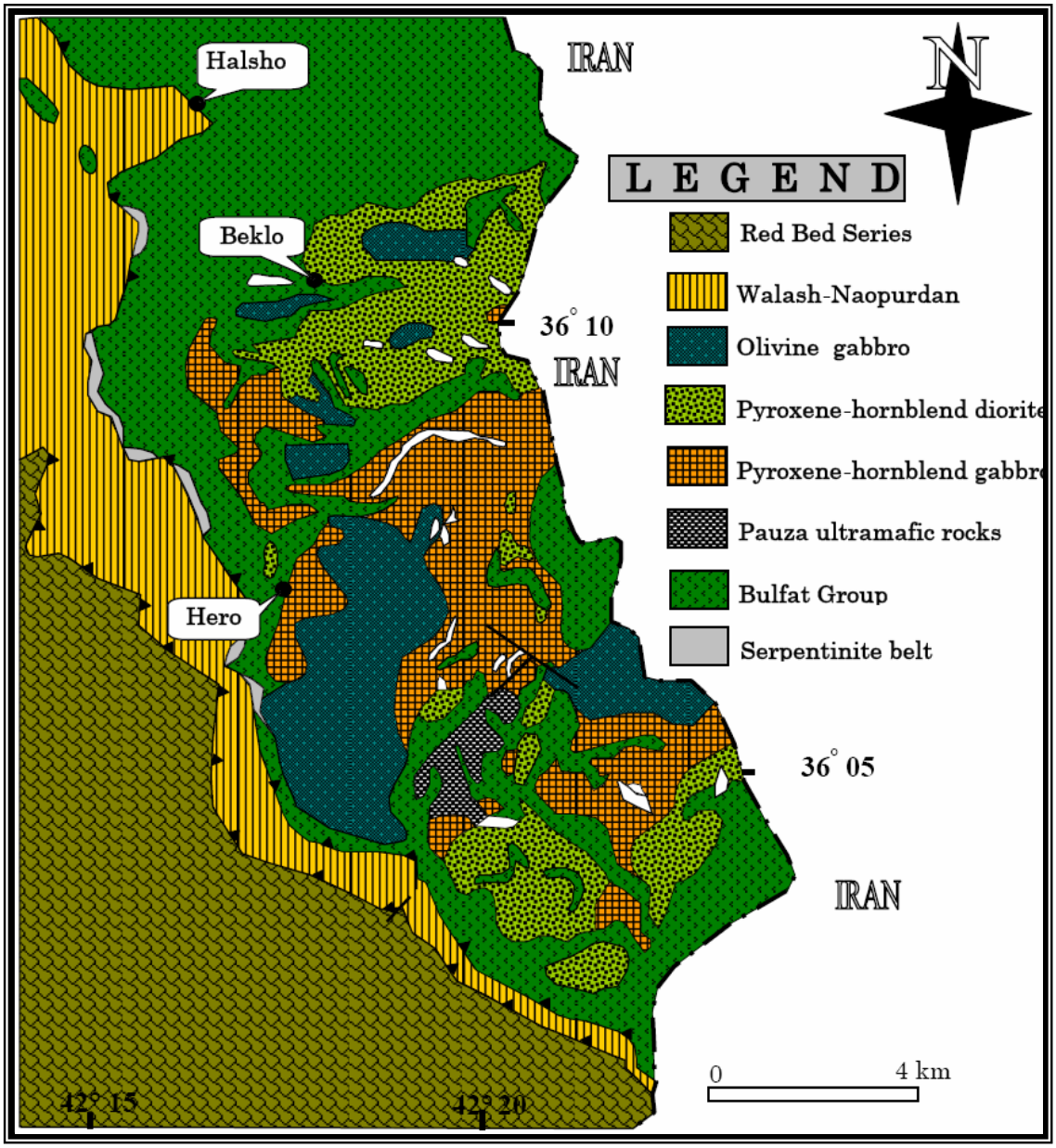

Fig. 2-5: Geological map of the Qaladez area.

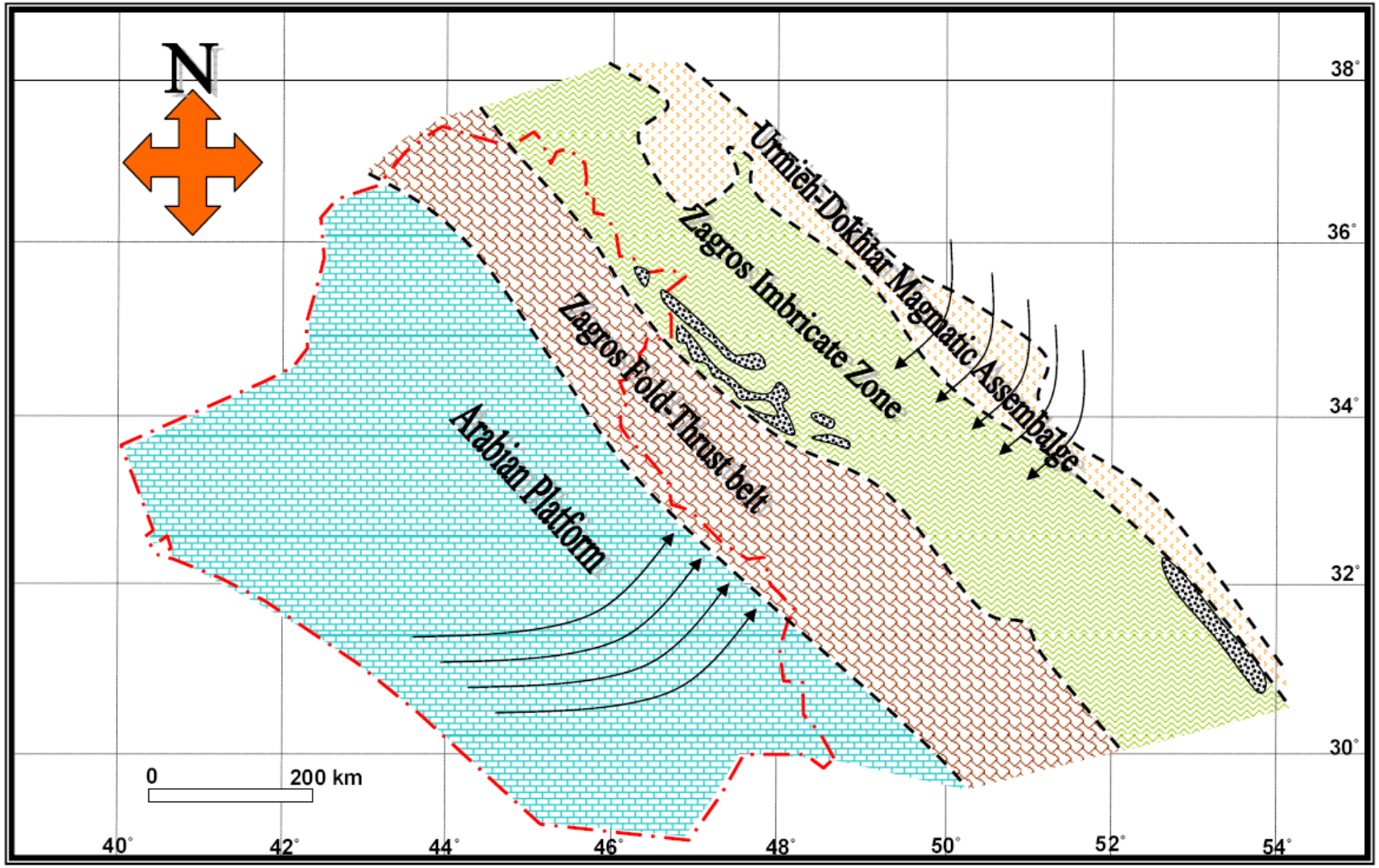

Fig. 2-6: Main tectonic units of Iraq and adjacent territories

Chapter 3

Petrology of ultramafic rocks

1-Field observation and Petrography

From Jun to August 2007, 200 rock samples were collected from three different localities within the Iraqi Zagros Thrust Zone, including Penjwin ophiolite, Mawat ophiolite and Pauza ultramafic body. Samples were extracted using Estwing hammers. All 200 samples were prepared for thin section using a standard rock saw, and 50 representative samples were chosen to be made into polished thin sections. Samples to be made into polished thin sections were chosen on the basis of least weathering and least apparent degree of serpentinization to represent the freshest and most undeformed rocks across the entire rock outcrops.

3-1 Penjwin ultramafic body

3-1-1 Dunite

Dunite occurs as lenses (30 cm × 30cm in dimension) (Fig.3-1) or as envelopes surrounding chromitite ore bodies. The contact between the dunite lenses and their host peridotite are relatively sharp but the dunite envelopes around the chromitites grade outward into harzburgite. In dunite, olivine forms anhedral grians, 0.1- 0.5 mm across, many of which have typical kink band texture, similar to deformational fabric seen in the mantle tectonites (Raymond, 2002; Coshi and Gardner, 2004). Chromian spinel forms euhedral grians, 0.5 mm across, and is nearly opaque to dark reddish brown in thin section. It is commonly inhomogeneous, displaying a zoning pattern of Cr-rich core compositions to Cr-poor rim compositions. The chromite crystals often associate thin rims of magnetite and ferrian chromite or chromian magnetite (nomenclature after Evans and Frost, 1975; Barnes, 2000), which developed during hydrothermal alteration or serpentinization.

3-1-2 Harzburgite

Harzburgite is the most abundant rock type in the Penjwin ultramafic body. Although the harzburgites have a similar megascopic appearance (Fig.3-2), they can be subdivided readily into two principal petrographic groups on the basis of mineral association and distance to the main thrust fault. The first group, designated the "Mlakawa-type" because a large body exposed at Mlakawa is typical of the group, consists of olivine, talc, tremolite, and serpentine, that has a direct contact with the main thrust fault. The second group is called "KaniManga-type", after the village of KaniMana which is located in the front of harzburgite, which consists of olivine, and hornblende. This type is just located behinds the first group and it is far from the main thrust faults by 2-3 km northeast. In both types disseminated chromian spinel occurs as polygonal to amoeboied crystal, and sometimes has inclusion of silicate minerals, including olivine and serpentine.

3-1-3 Pyroxenite

Pyroxeneite assemblages are locally found as veins of several centimetres thick in the main harzburgite body (Fig. 3-3). Thicker vein is the source of discrete megacrysts of the clinopyroxene assemblage. The veins are remarkably planer, indicating that the mantle host rock (harzburgite) fractured in a brittle manner by hydraulic fracturing (e.g., Best, 2003). Then the pyroxeneite magma agent was emplaced into the fracture, forming pyroxene veins. Pyroxeneite consists of megacrysts of clinopyroxene with ilmenite exsolution lamellae suggesting the rock of either of ultrahigh-pressure origin or ultra-deep mantle origin (about 170 km)? (e.g., Zhang and Liou, 1998; Best, 2003; Zhang and Liou, 2003).

3-1-4 Chromitite

The chromitites are hosted in harzburgite, although they are typically enveloped by dunite. The chromitites bodies are mainly lensoidal in form (Fig. 3-4), but some occur as veins, stringers and linear or planer seggregation (Fig. 3-5). The dimensions are highly variable, generally ranging from 2 to 3 m long and 0.5-2 m thick. Most chromitite bodies are concordant with the foliation in the host peridotite. The contacts between the chromitites and host dunites or harzburgites are usually sharp, but some chromitite bodies grade into the duite envelope by increasing in modal olivine. Most of the chromitites have massive (> 80 % chromite) or disseminated texture. Chromite in the massive chromitites is typically medium grained (1-4 mm across). Disseminated chromitites occur as aggregates of 0.5-1mm crystal. Common banded texture is also present. Olivine and tremolite, the most abundant silicate minerals in the chromitites, occur as matrix minerals and as inclusions in chromite.

3-1-5 Hornblendite

Hornblendite is hosted in harzburgite. Hornblendite bodies are always lensoidal in form (Fig. 3-6). The dimensions are highly variable, generally ranging from 2 to 3 m long and 0.5-2 m thick. Most hornblendite bodies are concordant with the foliation in the host peridotite. The contacts between the hornblendite and host harzburgite are typically sharp. All hornblendite lenses have granular texture, in which hornblende is the major minerals (90 vol. %), with some plagioclase (7 vol. %), and accessory ilmenite. Hornblende is typically medium grained (0.5-2 mm across) and plagioclase mostly occurs as rounded grain with 0.2-1 mm across. Oriented inclusions of ilmenite are abundant in the core of hornblende crystals. A hornblendite lens at the main thrust fault contains lensoidal rock of centimetric scale (Fig.3-7). It has mineral assemblages rutile + Cl-apatite + ilmenite + chlorite + amphibole ± pyroxene.

3-1-6 Serpentinite

Two types of serpentinite are recognized; they are massive and sheared ones. The former is characterized by pseudomorphic texture, whereas the latter by tiger skin texture (Mohammad et al., 2007). Olivine and pyroxene have mesh and bastite textures, respectively. In mesh texture, olivine is survived at the core of mesh consisting of serpentines. The mesh texture is more common in dunite. Bastite texture resembles mesh texture except that the mesh centre consists of pyroxene and it is more common in pyroxene-rich peridotite. Serpentine pseudomorphs consist of lizardite and chrysotile, which are early low-temperature serpentinization products. Antigorite is also found as a later-stage recrystallization product in the sheared parts of host serpentinites (Mohammad and Maekawa, 2007). In addition to primary olivine and pyroxene, serpentine, chromian chlorite, talc, tremolite, and disseminated chromian spinel are also present. Fine-grained elongated opaque minerals (mainly magnetite) are commonly observed along the margins of individual mesh cells of olivine pseudomorphs and cleavages in pyroxene bustites.

3-2 Mawat ultramafic body

3-2-1 Dunite

Dunite is massive, and occupies the highest peak of Mawat ultramafic bodies (Fig. 3-8). Dunite has typical olive-green colour, and is characterized by equigraular-mosaic, and equigraular-tabular textures (texture nomenclature after Raymond, 2002). In dunite, olivine forms anhedral grians of 0.5-10 mm across. It is either of olive-green or black in color (Fig. 3-9). The black color olivine contains magnetite exsolution lamellae parallel to c-crystallographic axis, many of which have typical kink band texture and fracture, similar to deformational fabrics seen in mantle tectonites from ophiolites (Raymond, 2002; Coshi and Gardner, 2004).

Chromian spinel forms euhedral grians of 0.5 - 5mm across, and is nearly opaque to dark reddish brown under polarizing microscope.

3-2-2 Harzburgite

Harzburgite is massive, and occupies 70 % by the area of Mawat ultramafic bodies (Fig. 3-10). It is characterized by typical equigraular-mosaic texture. Harzburgite consists of olivine, orthopyroxene, and clinopyroxene. They are partly to completely replaced by talc. Chromian spinel forms amoeboid grians, of 0.3 – 0.5 mm across, and are nearly opaque to dark reddish brown in thin section, the minerals contains inclusions of silicate phases like serpentine and olivine.

3-2-3 Websterite

Webesterite occurs as a pod (10 × 10 cm) within the main harzburgite body (Fig. 3-11). The rock is characterized by typical equigraular texture. Webesterite consists of clinopyroxene (2-3 mm across), orthopyroxene (0.5-1 mm across), olivine (0.1 mm across) and accessory plagioclase which occur as a fine grain between pyroxenes (pigeonite + diopside) crystals. These constituent minerals partly underwent chloritization and sericitization.

3-2-4 Hornblendite

The hornblendite is hosted in harzburgite. Hornblendite bodies are always lensoidal in form (Fig. 3-12). The dimensions are highly variable, generally ranging from 2 to 3 m long and 0.5-2 m thick. Most hornblendite bodies are concordant with the foliation in the host peridotite. The contacts between the hornblendite and host harzburgites are typically sharp. All hornblendite lenses have granular texture, and consists mainly of hornblende (90 vol. %) with some plagioclase (7 vol. %), and contain

small amount of ilmenite. Hornblende occurs as medium grained crystal (0.5-2 mm across). Plagioclase shows mostly rounded shape with 0.2-1 mm across. Inclusions with preferred orientation are abundant in core of hornblende.

3-2-5 Pyroxenite

Pyroxenite ranging in size from massive block to 10-cm vein (Fig. 3-13). Massive block is found in the south of the Mawat ultramafic bodies, whereas the vein is observed at the highest peak in the main body of massive duinte. Massive pyroxenite, consisting of coarse-grained euhedral to subherdal orthopyroxene and clinoppyroxene, in which clinopyroxene undergo extensive talcitization. Vein types consisting of monomineralic diopside which is host mineral of native copper ore.

3-2-6 Serpentinite

Serpentinite is of massive type, either associated with Mawat ophiolite or as isolated serpentinite bodies within Walash-Noupradan volcano-sedimentary unit of plaeoarc tectonic setting (Mohammad and Maekawa, 2007). Serpentine pseudomorph consists of lizardite and chrysotile. In addition to serpentine minerals, chromian chlorite, talc, tremolite, disseminated chromian spinel, and relict olivine and pyroxene are also found. Fine-grained elongated opaque minerals are mainly magnetite, which is commonly observed along the margins of individual mesh cells of olivine pseudomorphs and cleavages in pyroxene bustites.

3-3 Pauza ultramafic body

3-3-1 Spinel lherzolite

The lherzolite samples have protogranular to porphyroclastic textures (e.g., Mercier and Nicolas, 1975; Harte, 1977). Their primary modal mineralogy includes olivine (50–70 vol. %), orthopyroxene (15–20 vol. %),

clinopyroxene (10–20 vol. %) and spinel (up to 5%). They display plastic deformations such as undulose extinction, strain lamellae, kink bands, rotation, shearing, which are associated with recrystallization, all typical features of Alpine-type peridotites. Olivine occurs as porphyroclastic grains (>2 mm) as well as smaller polygonal neoblasts (<0.2 mm) with abundant 120° triple junctions.

3-3-2 Harzburgite

Harzburgite, the most abundant rock in the Pauza peridotite, consists of olivine, orthopyroxene and a lesser amount of clinopyroxene and spinel. The modal abundance of olivine is 70-80 vol. %, orthopyroxene 25-20 vol. % and spinel as much as 5 vol.%. Clinopyroxene is rare and always occurs as exsolution lamellae in orthopyroxene. Small amounts of serpentinite, chlorite and opaque are also observed. Accessory pentlandite and native copper are dispersed throughout the rocks. Most of minerals display structures due to plastic deformation such as undulose extinction, strain lamellae, kink bands, rotation, and shearing, all typical features of alpine-type peridotites. Olivine forms porphyroclastic grains (<2 mm) as well as smaller polygonal neoblasts (≈ 0.2 mm) with abundant 120° triple junctions around orthopyroxene. Patches of fine- to coarse-grained olivine locally to completely replace orthopyroxene porphyroclasts forming millimetric scale podiform dunite.

3-3-3 Dunite

Dunite, collected from Pauza, is the least serpentinized lithology among the studied ultramafic rocks. It displays porphyroclastic to mylonitic textures, and consists of olivine (85–90 vol. %), clinopyroxene (1–3 vol. %) and disseminated spinel (up to 10 vol. %). Scarce serpentine, chlorite, tremolite (frequently in capillary veins) and magnetite are products of hydrothermal alteration. Coarse olivine (2.5–3.5 mm) is usually elongated and exhibits undulatory extinction and strain lamellae.

In places, it is surrounded by fine-grained olivine crystals showing a mylonitic fabric. Spinel is chromite and forms subhedral to euhedral crystals, typically 1 mm in diameter. The chromite crystals are commonly inhomogeneous, displaying a zoning pattern of Cr-rich core to Cr-poor rim. Chromite crystals are often associated with thin rims of magnetite and ferrian chromite or chromian magnetite, which formed during hydrothermal alteration.

3-3-4 Hornblendite vein

Hornblendite veins are rarely found in the Pauza ultramafics; only five has been recorded. The hornblendite veins range in thickness from 1 cm to 5 cm. It usually consists of mono-mineralic hornblende with flow texture, which may have interpreted to be originally pyroxene vein and thereafter hydrated to have been hornblendite during the kinematic history of the Pauza massif. Hornblendite veins sometime mainly consist of hornblende and plagioclase, with accessory spinel, and ilmenite. The veins are medium to coarse-grained 5–25 mm in thickness, and are undeformed granular texture. The coarse grain size as well as the lack of deformation suggest that the hornblendite veins were intruded relatively late in the kinematic history of the massif, although age is not known.

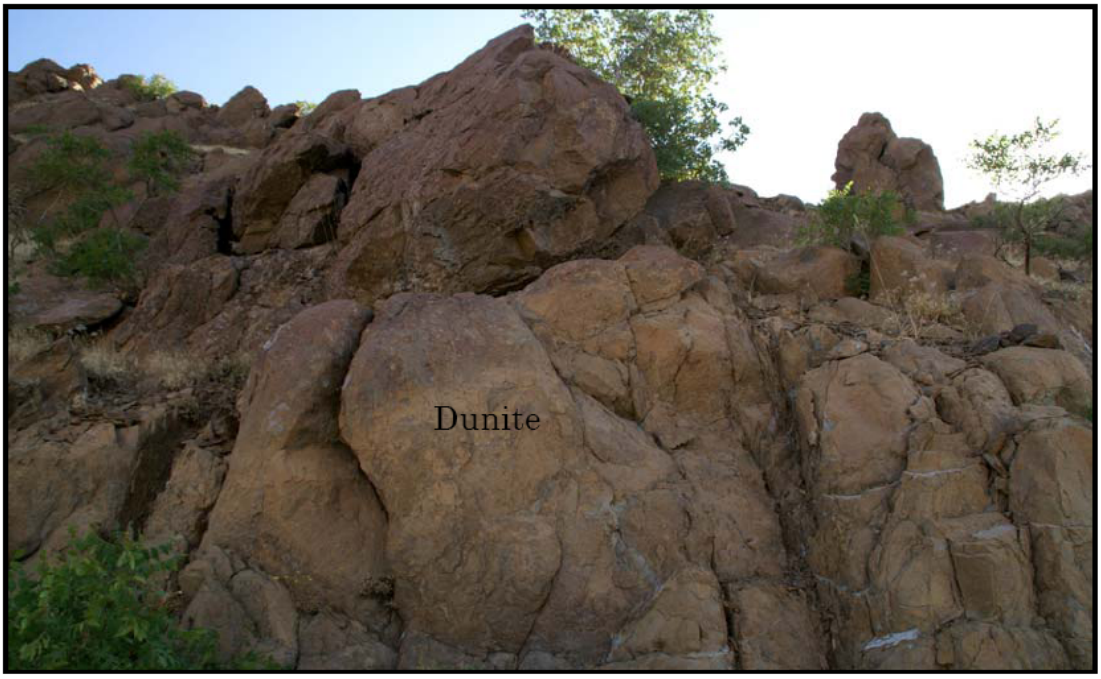

Fig. 3-1: Field photograph of dunite in Penjwin ultramafic body.

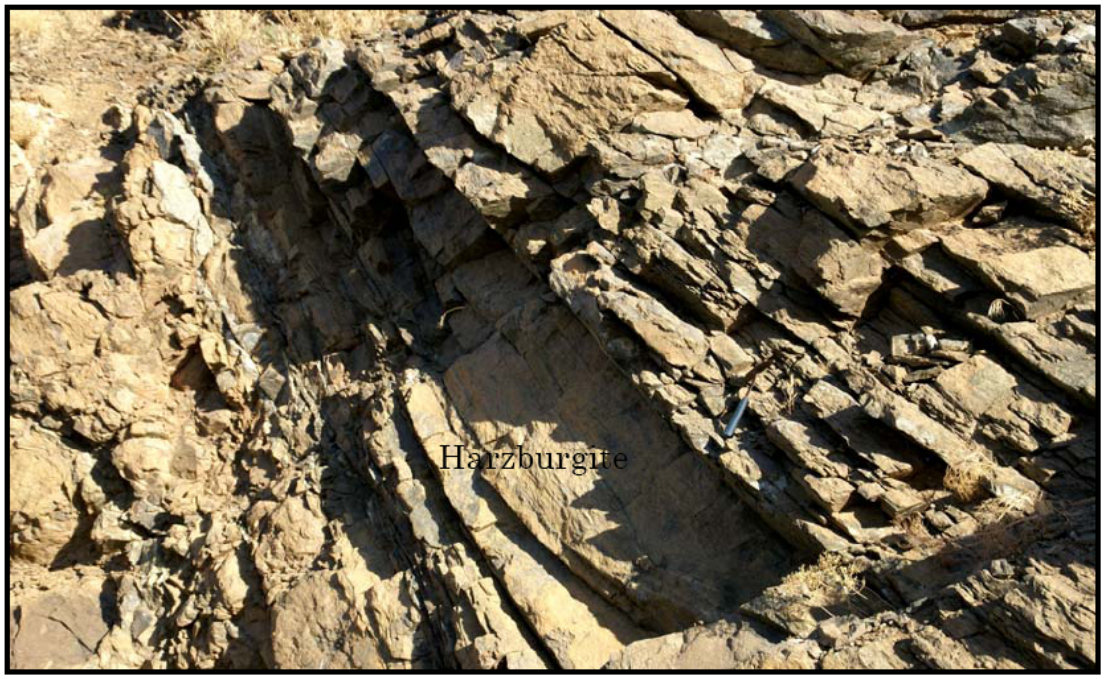

Fig. 3-2: Field photograph of layerd-like harzburgite in Penjwin ultramafic body.

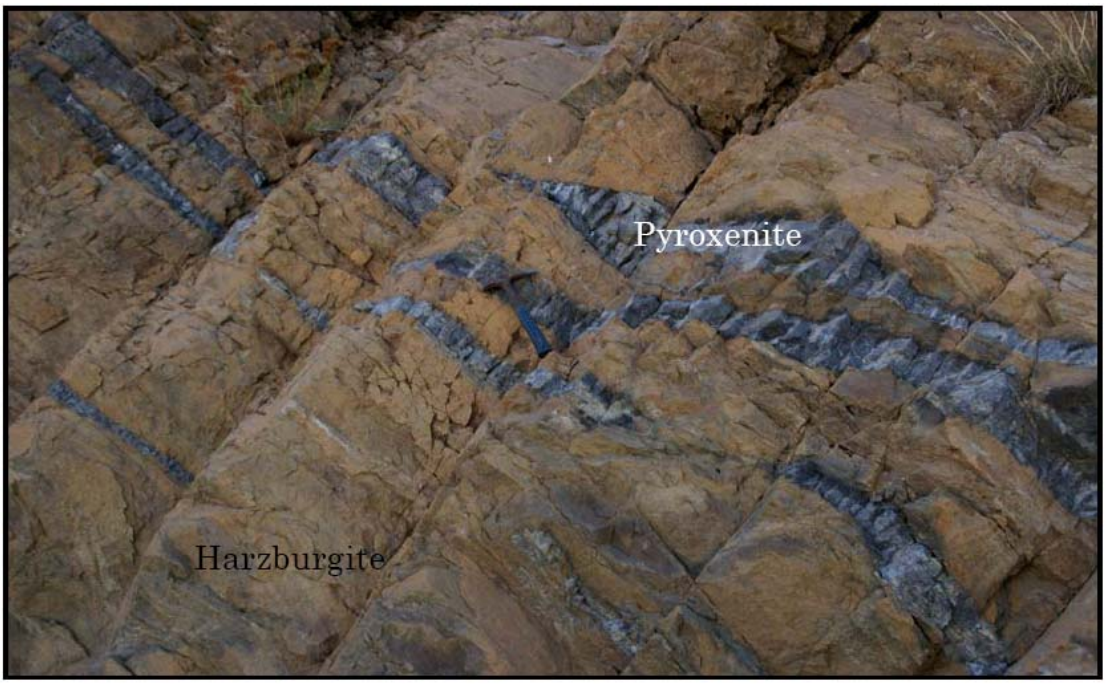

Fig. 3-3: Field photograph of pyroxenite veins within harzburgite in Penjwin ulramafic body.

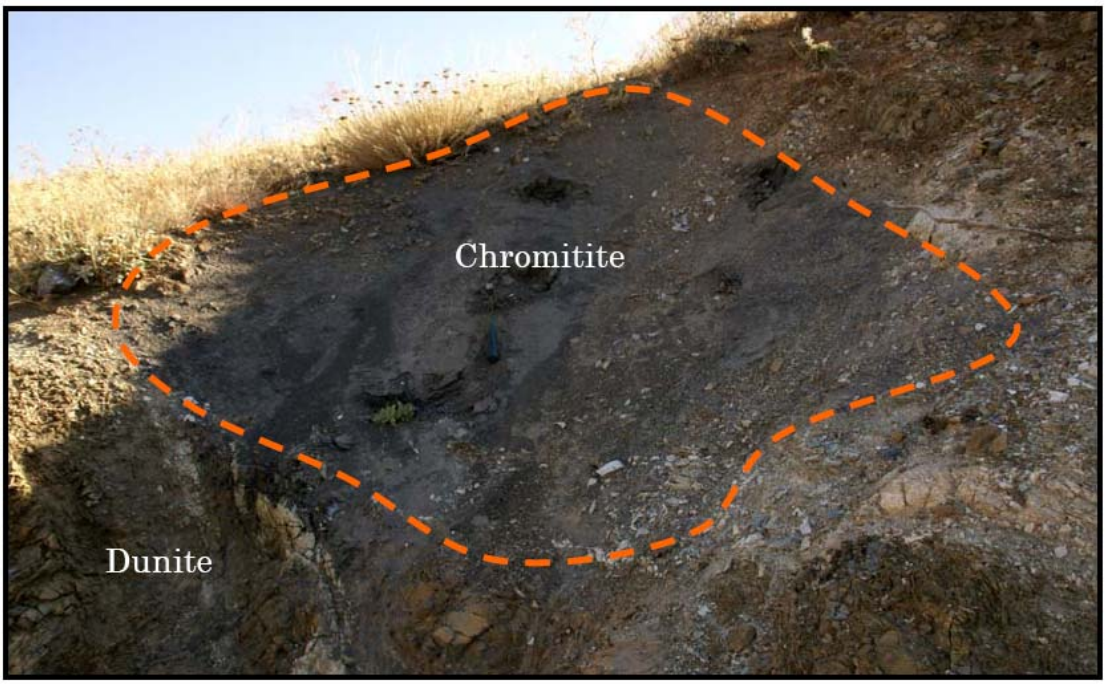

Fig. 3-4: Field photograph of podiform chromitite envloped dunite in Penjwin ultramafic body.

Fig. 3-5: Field photograph of banded chromite in Penjwin ultramafic body

Fig. 3-6: Field photograph of hornblendite lens within harzburgite of Penjwin ultramafic body.

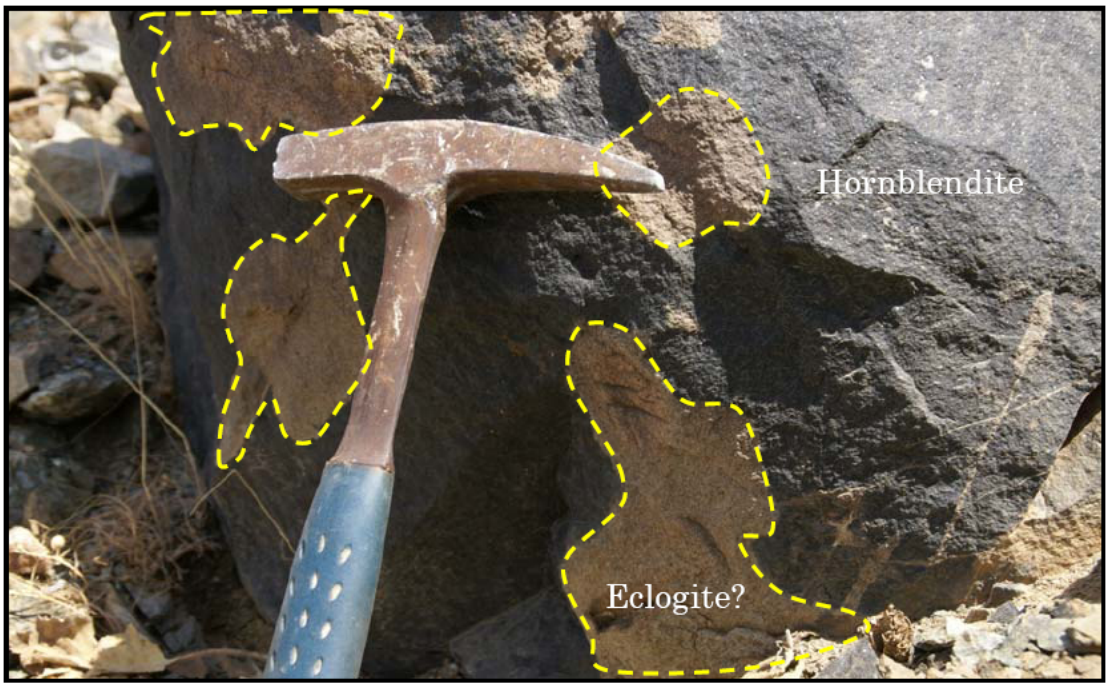

Fig. 3-7: Field photograph of possible eclogite lenses in hornblendite of Penjwin ultramafic body.

Fig. 3-8: Field photograph of massive dunite of Mawat ultramafic body.

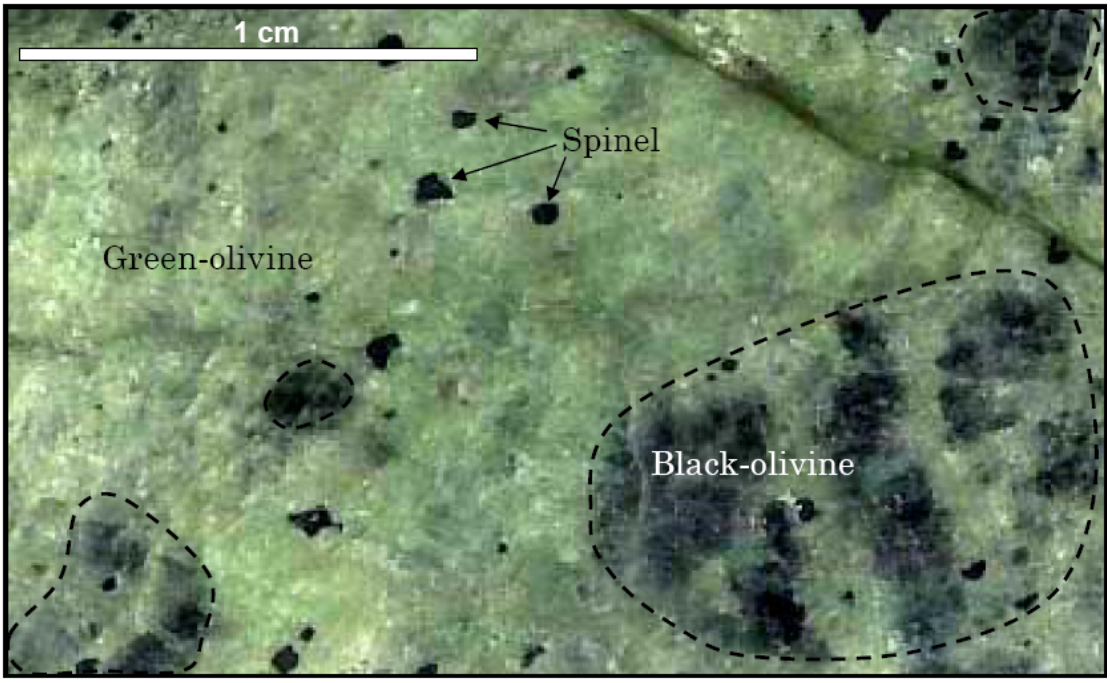

Fig. 3-9:Slab photograph of massive dunite of Mawat ultramafic body, showing different kinds of olivine.

Fig. 3-10: Field photograph of massive harzburgite of Mawat ultramafic body.

Fig. 3-11: Field photograph of webesterite pod within harzburgite of Mawat ultramafic body

Fig. 3-12: Field photograph of hornblendite lens in harzburgite of Mawat ultramafic body

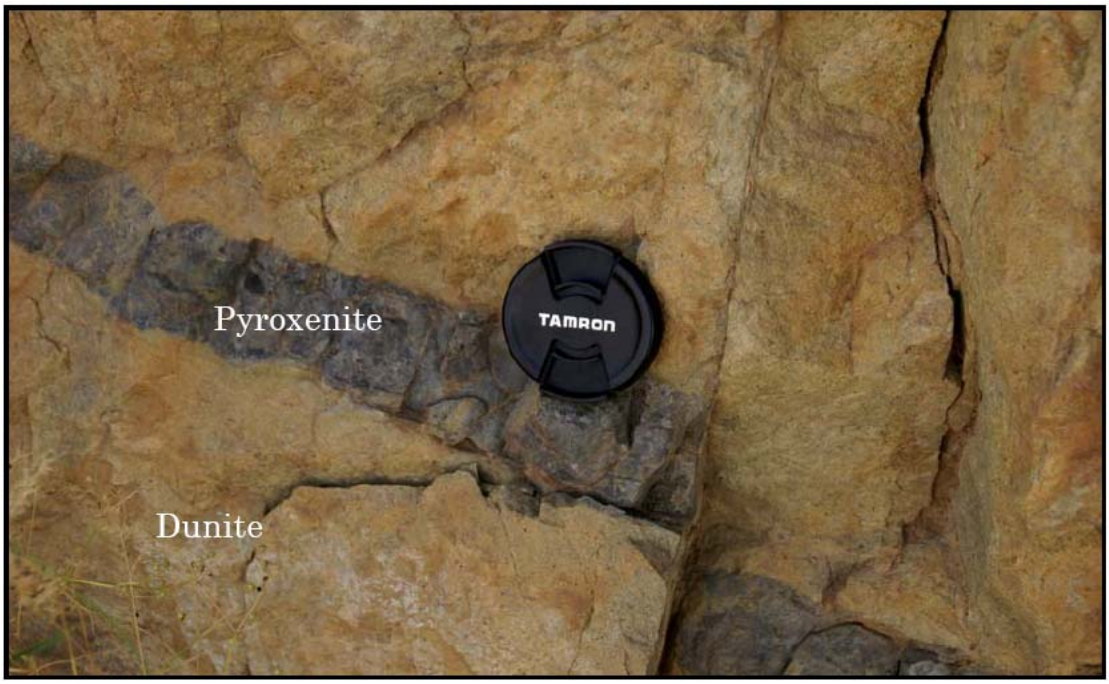

Fig. 3-13: Field photograph of pyroxenite vein in dunite of Mawat ultramafic body.

Chapter 4
Mineralogy and mineral chemistry

4 Mineralogy and mineral chemistry

Because of the occurrences of many types of ultramafic rocks with the Iraqi Zagros Thrust Zone (see chapter three). In this chapter I give the mineralogy and mineral chemistry of serpentineized peridotites in Mawat and Penjwin ophiolites, and peridotites from Pauza ultramafic body.

4-1 Penjwin peridotites

4-1-1 Olivine

I analyzed relict highly-strained olivine grains because they best represent primary magmatic compositions (Coish and Gardner, 2004). Olivines (Table 4 - 1) in both dunite and harzburgite have a narrow compositional range of $Fo_{90–92}$.

4-1-2 Spinel

Representative analyses of spinel from dunite and harzburgite are given in Table 4 - 2. Spinels in dunite are inhomogeneous in compositions and characterized by normal zoning, with Cr- number [=Cr×100/ (Cr + Al)] ranging from 63 to 71 (Fig. 4 - 1), and Mg-number [Mg×100/ (Mg + Fe)] ranging from 36 to 44. Spinels in harzburgite are also inhomogeneous in composition and characterized by both reverse and normal zonings, i.e., Al-rich core to Cr-rich rim or vice versa. Cr- number is ranging from 53 to 57, and Mg-number ranging from 32 to 36.

EDS analyses of disseminated chromian spinel show different zoning from Al-rich core through transitional ferrichromite zone to outer Cr-magnetite zone in both dunite and Mlakawa type harzburgite (Fig 4 - 2). The zoning is interpreted to have been affected by alteration due to serpentinization. Whereas disseminated chromian spinel in KaniManga type harzburgite shows typical reverse zoning i.e. Cr-rich core to Al-rich rim (Fig. 4 - 3), that possibly is interpreted to be a growth zoning. Here, in Table 4 - 2, I only give the composition of the cores of chromian spinel

which have not undergone total alteration to ferrichromite and represent primary magmatic chromian spinel.

4-1-3 Pyroxene

Representative analyses of pyroxene from harzburgite are given in Table 4 - 3. Orthopyroxene is enstatite ($En_{89}Wo_1Fs_9$) (Fig.4 - 4). Enstatite has low Al_2O_3 contents (0.2 wt. %), with relatively high CaO and TiO_2 contents (1.1 and 0.1 wt. % respectively). Clinopyroxene is diopside ($En_{47}Wo_{49}Fs_2$). Diopside has low Al_2O_3 (0.2 wt. %) and extremely low TiO_2 (< 0.03 wt. %). Cr_2O_3 contents are ranging from 1 to 1.5 wt %.

4-1-4 Hydrous phases

Hydrous phases are represented mainly by serpentine polymorphs, chromian chlorite, and anthophylite. Lizardite and chrysotile are dominated serpentine polymorphs in massive type serpentinite. Antigorite is restricted to the sheared type of serpentinite at the main thrust fault. The analyses (Table 4 - 4) show that antigorite is richer in FeO and poorer in MgO and SiO_2 than chrysotile (Mohammad and Maekawa, 2007). Chlorite always occurs around the chromian spinel or within the chromian spinel. According to the classification of Hey (1954) all analyzed chlorite are clinochlorite. However it contain considerable amount of Cr_2O_3 1.4 to 2.6 % (Table 4 - 5) so I can name it “chromian clinochlorite”. Anthophylite are more common in the KaniManga type harzburgite. Values of X_{Mg} show a fairly limited range (0.89 to 0.90) (Table 4 - 6).

4-2 Mawat peridotites

4-2-1 Olivine

Representative analyses of olivine from Mawat ultramafic body are given in Table 4 - 7. Olivine in harzburgite has contents ranging from 90.6 to 91.6. Both black and green olivines in dunite are homogeneous in

compositions with Mg-number ranging from 91.3 to 92.5. They have low CaO (< 0.04 wt. %), and MnO (< 0.3 wt. %).

4-2-2 Pyroxenes

Representative analyses of pyroxenes from harzburgite are given in Table 4 - 8. Orthopyroxenes are enstatite ($En_{89}Wo_2Fs_8$) and augite (En_{68} Wo_3 Fs_{28}) (Fig.4 - 5) with Mg-number of 89 to 91 and 95 to 96 respectively. Enstatite has low Al_2O_3 contents (nearly zero), with relatively high CaO and TiO_2 contents (1.2 and 0.15 wt. %, respectively). Augite has very low FeO contents (less than 2 wt. %), with high CaO (13 - 14 wt. %) and extremely low TiO_2 (nearly zero).

4-2-3 Spinel

Representative analyses of spinel from dunite and harzburgite are given in Table 4 - 9. Spinels in dunite are homogeneous in composition and lack zoning, with Cr-number ranging from 79 to 80 (Fig. 4 - 6), and Mg-number ranging from 29 to 31. Spinels in harzburgite are inhomogeneous in composition and characterized by normal zoning i.e. Al-rich core to Cr-rich rim. Cr- number ranges from 63 to 71, and Mg-number from 36 to 44.

3-2-4 Hydrous phases

Hydrous phases are represented mainly by serpentine and talc. Lizardite and chrysotile are dominated serpentine polymorphs in serpentinite; antigorite is nearly absent. EDS analyses of serpentine are given in Table 4 - 10. Because serpentine minerals comprise several generations of growth, the analyses show a high degree of variability (Mohammad and Meakawa, 2007).

4-3 Pauza peridotite

4-3-1 Olivine

Representative analyses of olivine from Pauza ultramafic body are given in Table 4-11. Olivines in harzburgite and lherzolite have foresteritic content ranging from 90.6 to 91.6. Olivines in dunite are homogeneous in compositions with Mg-number ranging from 91.3 to 92.5. They have low CaO (< 0.04 wt. %), and MnO (< 0.3 wt. %). NiO in olivine increases from lherzolite through harzburite to dunite ($NiO_{lherzolite}$ < $NiO_{hazrburgite}$ < NiO_{dunite}).

4-3-2 Pyroxene

Representative analyses of pyroxene from harzburgite are given in Table 4 -12. Orthopyroxene are enstatite ($En_{90}Fs_{9.80}Wo_{0.20}$) and augite ($En_{66}$ Fs_6 Wo_{28}) (Fig 4 - 7) with Mg-number varying from 89 to 91 and 95 to 96 respectively. Enstatite has low Al_2O_3 contents (nearly zero), with relatively high CaO and TiO_2 contents (1.2 and 0.15 wt. % respectively). Augite has very low FeO contents (less than 2 wt. %), with high CaO (13 - 14 wt. %) and extremely low TiO_2 (nearly zero). Clinopyroxenes in lherzolite are diopside (En_{35} Fs_{17} Wo_{48}), and has high Al_2O_3 (1 - 1.5 wt. %).

4-3-3 Spinel

Representative analyses of spinel from dunite and harzburgite are given in Table 4 - 13. Spinel in dunite are homogenous in composition and lacks zoning. Cr-number of spinel ranges from 80 to 83 (Fig. 4 - 8), and Mg-number ranging from 24 to 25. Spinels in harzburgite are homogeneous in composition with Cr-number ranging from 58 to 61 and Mg-number ranging from 36 - 38. Spinel in lherzolite (Table 4 – 14) are homogenous in composition, lack zoning, and has Cr-number ranging from 29 to 34, and Mg-number ranging from 48 to 51. (Cr-number $_{lherzolite}$ < Cr-number $_{hazrburgite}$ < Cr-number $_{dunite}$).

4-3-4 Hydrous phases

Hydrous phases are represented mainly by serpentine and talc. Lizardite and chrysotile are dominated serpentine polymorphs in serpentinite; antigorite is nearly absent.

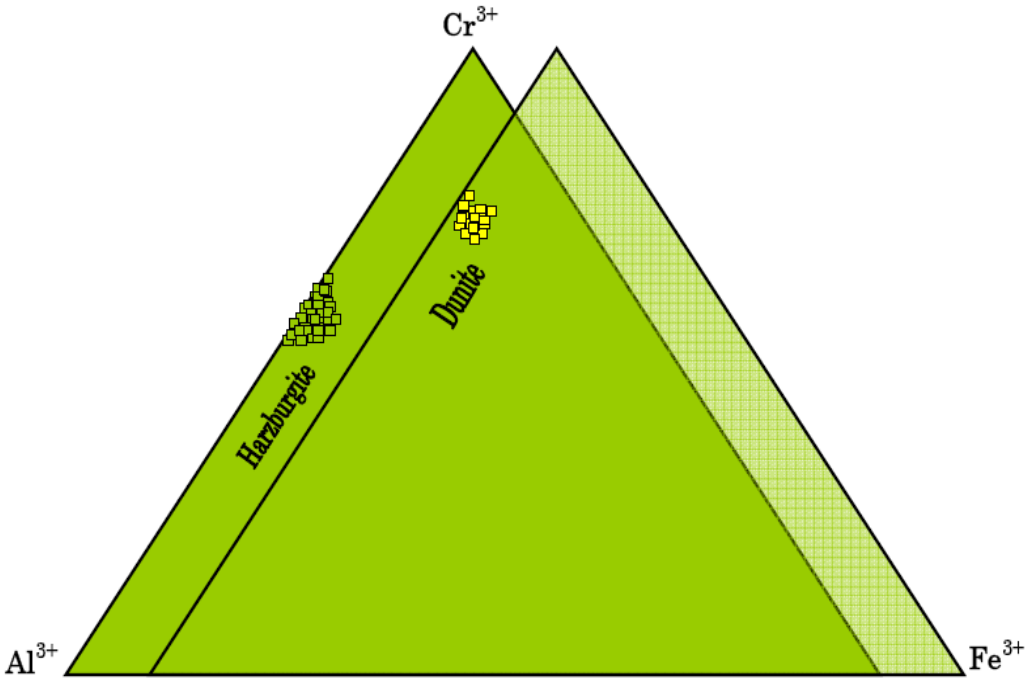

Fig 4 -1: Compositions of chromian spinel cores in dunite and harzburgite of Penjwin peridotite plotted on Cr^{3+}- Al^{3+}- Fe^{3+} diagrams.

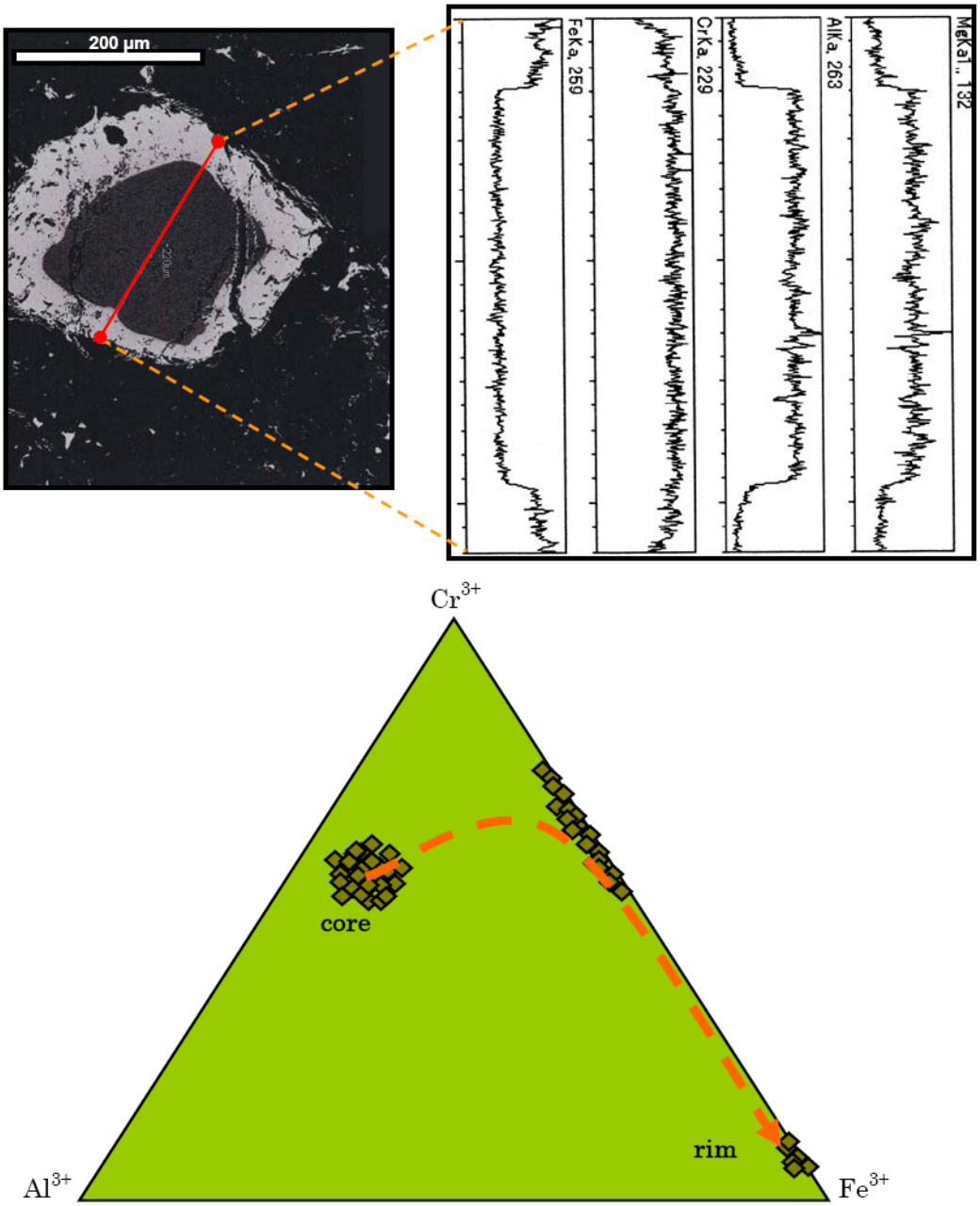

Fig 4 -2: Compositions of chromian spinel in Mlakawa-type harzburgite of Penjwin peridotite plotted on Cr^{3+}- Al^{3+}- Fe^{3+} diagram, with both back-scattered image and line scan of normal zoning in chromian spinel.

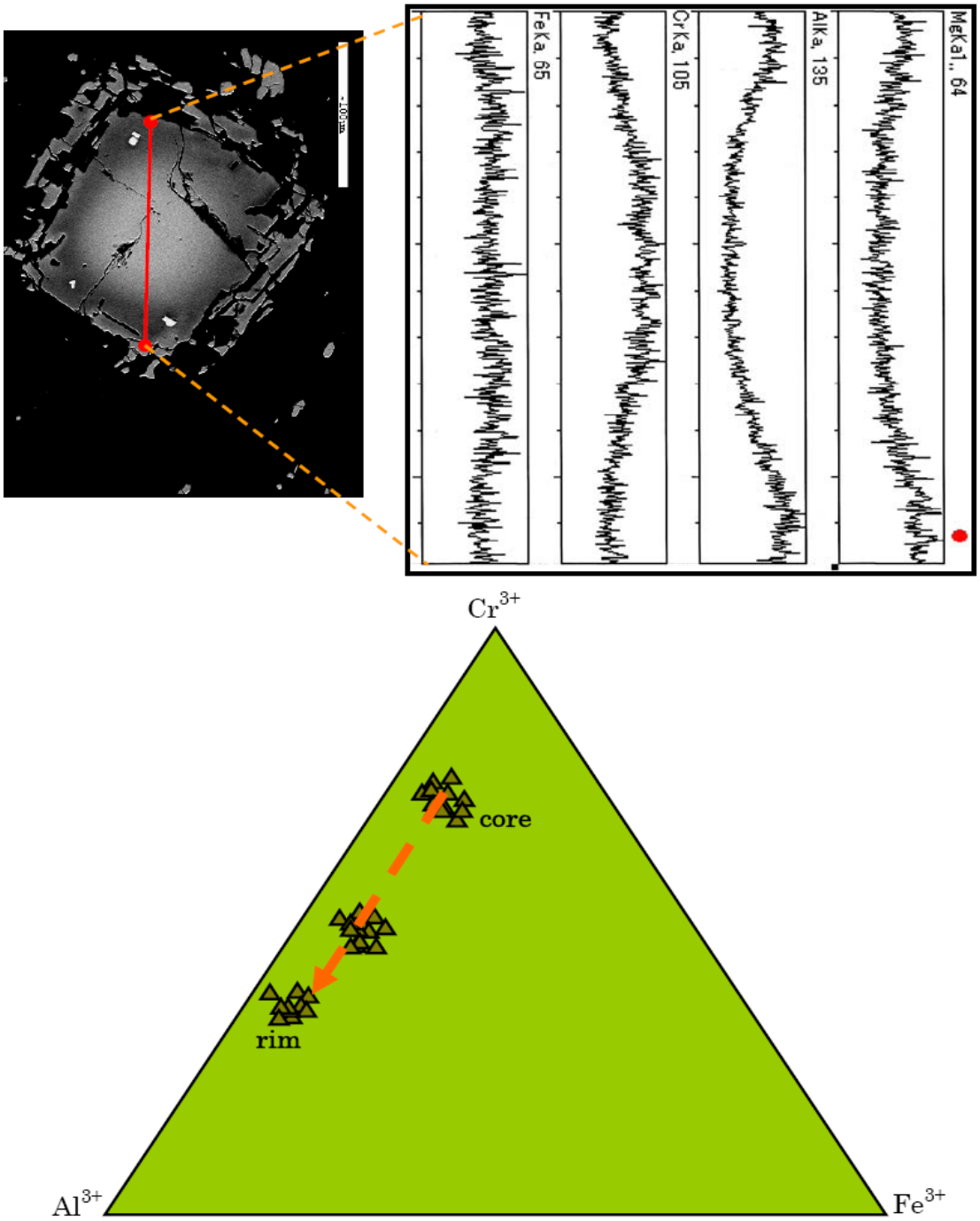

Fig 4 -3: Compositions of chromian spinel in KaniManga-type harzburgite of Penjwin peridotite plotted on Cr^{3+}- Al^{3+}- Fe^{3+} diagram, with both back-scattered image and line scan showing reverse zoning in chromian spinel.

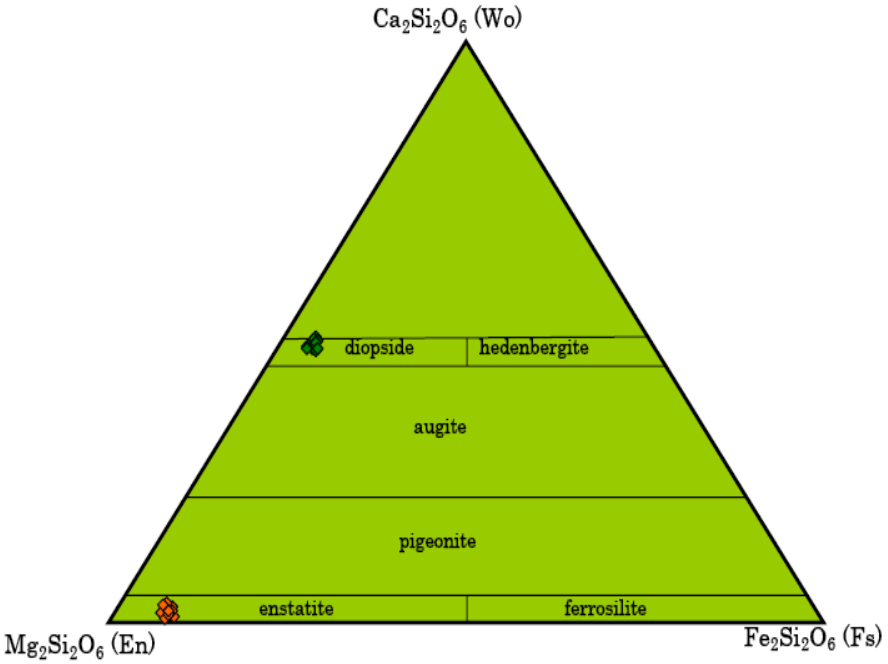

Fig 4 -4: Compositions of pyroxene in harzburgite of Penjwin peridotite plotted on En-Wo-Fs diagram (after Morimoto et al., 1988)

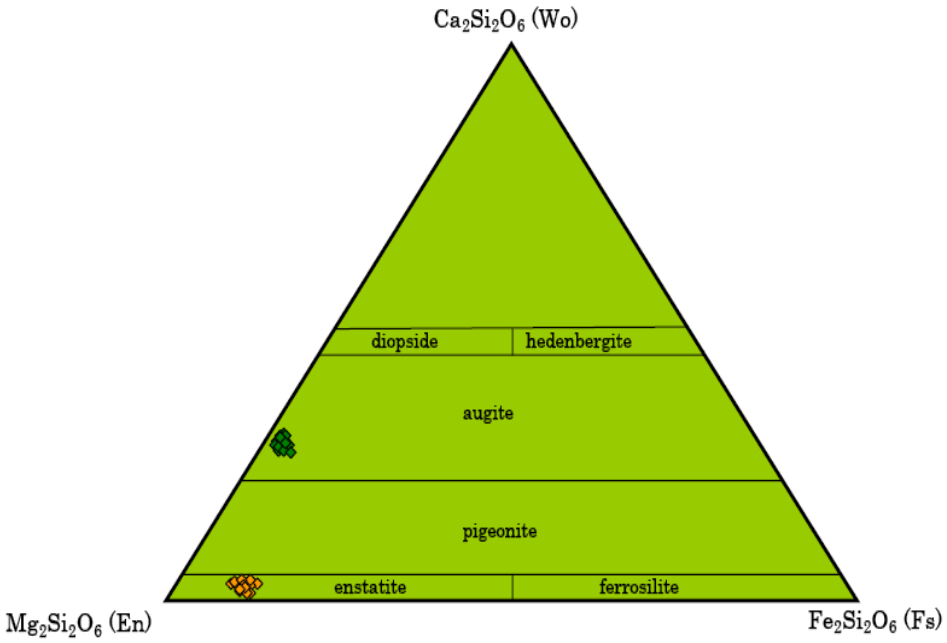

Fig 4 -5: Compositions of pyroxene in harzburgite of Mawat peridotite plotted on En-Wo-Fs diagram (after Morimoto et al., 1988).

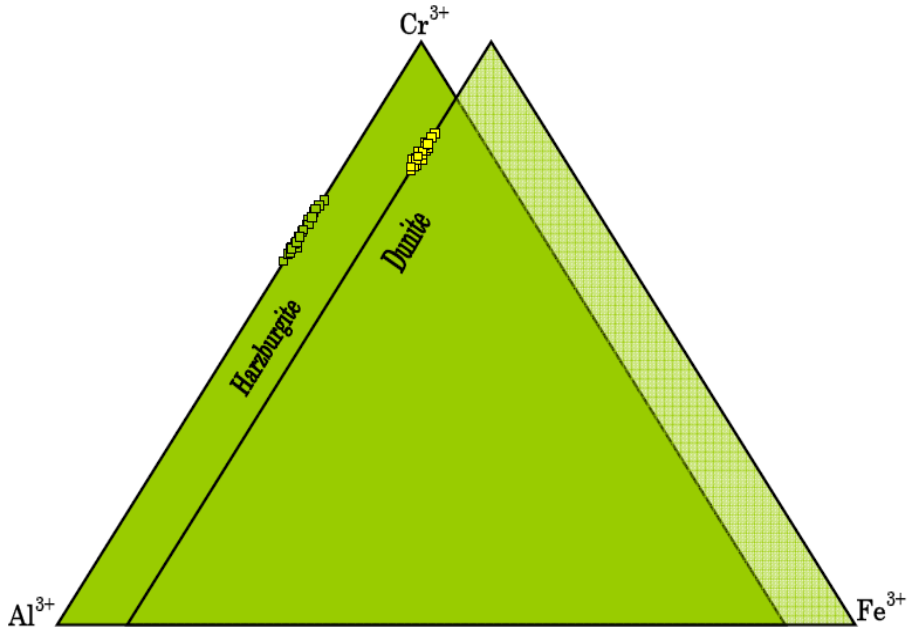

Fig 4 -6: Compositions of chromian spinel cores in dunite and harzburgite of Mawat peridotite plotted on Cr^{3+}- Al^{3+}- Fe^{3+} diagrams.

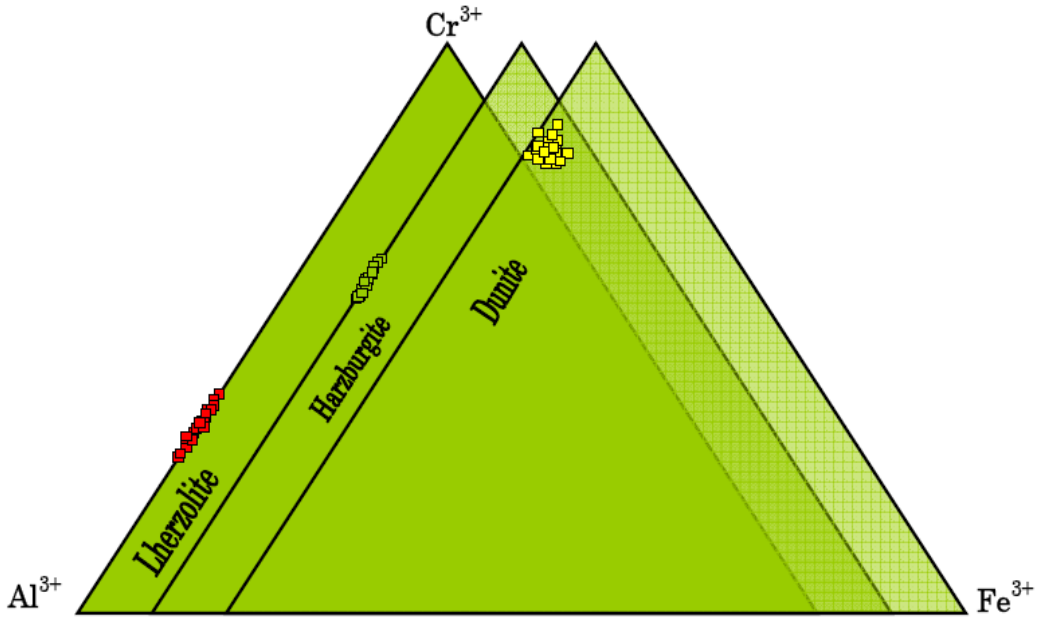

Fig 4 -7: Compositions of chromian spinel cores in dunite, harzburgite and lherzolite of Pauza peridotite plotted on Cr^{3+}- Al^{3+}- Fe^{3+} diagrams.

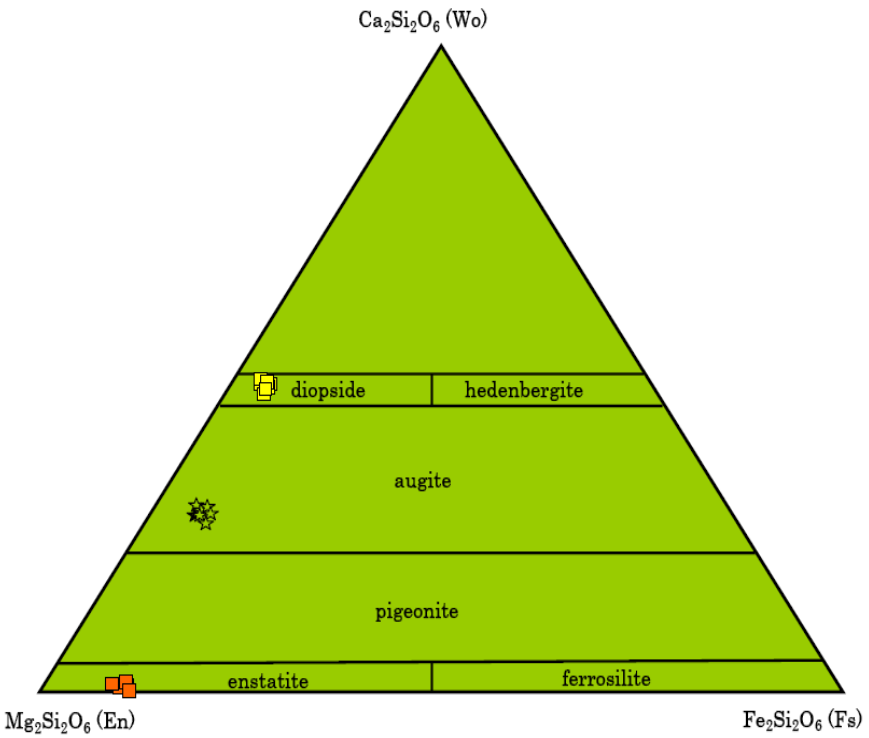

Fig 4 -8: Compositions of pyroxene in Pauza peridotite plotted on En-Wo-Fs diagram (after Morimoto et al., 1988).

Chapter 5

Discussions

5-1 Classifications and Petrogenesis

It is well known that the chromian spinel chemistry plays an important role in classifying mantle-derived peridotite in terms of origin and tectonic setting (Dick and Bullen, 1984). However the ultramafics along the Iraqi Zagros Thrust Zone reflect vitiations from lherzolite through harzburgite to dunite, but their chromian spinels chemistry are plotted in the field of alpine type peridotite on Cr-number vs. Mg-number classification diagram (Fig. 5 – 3) indicating that all ultramafics along the Iraqi Zagros Thrust Zone are of alpine type. Dick and Bullen (1984) subdivided alpine peridotite based on Cr-number of spinels into three types: (I) peridotites that contain spinels with Cr-number < 0.6, which are thought to be derived from oceanic lithosphere formed at mid-oceanic ridge, although the possibility of other environments are not precluded; (III) peridotites that contain spinels with Cr-number > 0.6, which are mostly considered to have formed in island arcs; and (II) peridotites that containing spinel spanning the full range composition between type I and type III, which reflects a composite origin, such as formation in subduction-related environments on oceanic crust. The core compositions of chromian spinels in both Mawat and Penjwin in peridotites correlate with those of type III (Fig. 5 – 1). The chromian spinel core composition in Pauza comprises both type I for lherzolite and type III for dunite and harzburite. The occurrences of different type of alpine peridotite within the same ultramafic body suggest that the above classification of alpine peridotite is not necessary to be correct for all alpine peridotites. This classification dose not considers the degrees of partial melting within the same ultramafic bodies that control the compositions of chromian spinel. Arai (1994) used the diagram of Fo content of olivine vs. Cr-number of chromian spinel to distinguish between cumulate and tectonite peridotites. The pattern of typical tectonite has variable Cr-number in a narrow range of Fo content. In contrast, the cumulate peridotite covers a wide range of Fo content for the limited Cr-number. All the samples of peridotite from the Iraqi Zagros Thrust Zone are consistently plotted with

the tectonite region of the graph (Fig. 5 – 3), are suggesting the tectonite origin for the Iraqi Zagros Thrust Zone peridotites.

5-2 Chemical modification of chromite during alteration

Spinel-group minerals, particularly chromite, are highly susceptible to chemical modification during hydrous alteration and metamorphism at low temperatures (Barnes, 2000). The variability of chromite composition reported in the literature may be the result of differences in alteration history, not differences in igneous origin. Tow types of zoning were observed in peridotite from IZTZ which are as follow:

5-2-1 Normal zoning

Normal zoning is the most common type of alteration of chromian spinel in peridotites along the Iraqi Zagros Thrust Zone. Back scattered image and line scan show that altered chromian spinel is concentrically zoned from Al-rich core to Fe-rich rim (ferrichromite) with magnetite outermost rim, which is in contact with chlorite aureoles (Fig. 4 – 2). Al^{3+}-Cr^{3+}-Fe^{3+} triangular plots distinctively characterize the three zones with apparent compositional gap in between (Fig. 4 – 2). The core is Al-rich and lies along the Cr-Al join. Due to extensive Al loss relative to Cr, spinel transitional zone lies midway along Fe-Cr join. The low alumina chromian spinel resulting from metamorphism is often called ferrichromite. However, the outer rim is Cr-magnetite, which is nearly devoid of Al and lies along the Fe-Cr joint. Magnetite formed by serpentinitzaion process is always called syn-serpentinization magnetites; it is identified from magmatic magnetite by that the magmatic magnetite is plots along the Al-Fe join (Barnes and Roeder, 2001).

The $Mg/(Mg+Fe^{2+})$ of the spinel-group minerals are dominantly controlled by the degree of the hydrothermal alteration (Barnes, 2000). Spinels altered under greenschist facies display Mg-number ranging from 0.4 to 0.7, while those altered in amphibolite facies have Mg-number <0.35 (Barnes, 2000). Hence, the $Mg/(Mg+Fe^{2+})$ ratios of the altered peridotite in

the Iraqi Zagros Thrust Zone are up to 0.4, suggesting that the approximate conditions of metamorphism are situated from the boundary of the greenschist–amphibolite facies to the lower amphibolite facies. This is in agreement with the low amphibolite facies assemblage of tremolite+antigorite+talc observed in the serpentinized peridotites.

5-2-2 Reverse zoning

Reveres zoning is very unusual and rare type of zoning, which is only recorded in KaniManga type harzburgite. It is characterized by Al-rich rim with gradual decrease of Al toward the center of the grain (Fig. 4 – 3). Al^{3+}-Cr^{3+}-Fe^{3+} triangular plots distinctively characterize the progressive enrichments of Al and decreasing of Cr contents toward the rims, while Fe^{3+} remains unchanged during this kind of alteration (Fig. 4 – 3). The assemblage of chlorite + pure foresterite + spinel with Al-rich rim suggests a mechanism for the formation of the zoning as follows (Fig. 5 – 2): The primitive chromian spinel (Cr-number = 58 – 61) in harzburgite underwent retrograde metamorphism along the rim by reaction with surrounding olivine (Fo_{90-91}) in the presences of hydrous silicate conditions to form both Cr-magnetite and chlorite aureole (chlorite contains Al_2O_3 about 18 wt. %). During later progressive metamorphism due to the collision of the Arabian plate with the Iranian plate, the Al_2O_3 expelled from the chlorite structure, forming a new neoblast of pure forsterite aureole (Fo_{95-96}) and rim of high aluminous spinel with Cr -number ranging from 28 to 32 on around primitive spinel. The only mineral which can accommodate Al_2O_3 during this transformation is spinel in ultramafic system. Most of the Fe in the primitive olivine and chromian spinel are consumed to form in the syn-serpentinization magnetites.

5-3 Serpentinization

The serpentinization process of peridotite along the IZTZ having both criteria of isochemical and allochemical processes. The formation of metasomatic rocks, rodingite and albitite, within serpentinite bodies

involves loss and gain of CaO, SiO_2, and Na_2O between serpentinized peridotite and country rock (Mohammad, 2004; Mohammad et al., 2007). This observation is not only consistent with the hypothesis that some serpentinization is ***constant-volume*** process; it suggests that serpentinization is an ongoing process, even at ambient temperatures at the earth's surface. However, the intensive fracturing in the massive serpentinite as well as the occurrence of kernel pattern (Mohammad and Maekawa, 2007) requires an increase of the volume of ultramafic body, suggesting that some serpentinization of ultramafic along IZTZ are ***constant-chemical*** process. Based on the above observation I can conclude that the early stage of serpentinization is isochmical, which require only adding water, with increasing the degree (late stage) of serpentinization it became allochemical process.

5-4 Partial melting

The peridotites of the IZTZ show many petrologic and geochemical signatures of partial melting. On the scale of the entire complex, the mantle rocks range from lherzolite throughout harzburgite to dunite. These petrological variations are associated with systematic changes in mineral compositions especially spinel and olivine. The chemistry of spinel-group minerals from the IZTZ ultramafic rocks reveal a multi-stage genesis in the different types of their host peridotites. Textural and chemical features of the minerals indicate that an early partial melting process played a distinctive role on their genesis. Lobate boundaries of the aluminous spinel grains of lherzolitic rock of peridotites along with their linear evolution of Cr-number with Mg-number and their resemblance to spinels of abyssal-type peridotite suggest the involvement of a partial melting episode in their genesis. Plots of the spinel-olivine pairs of lherzolitic peridotite on the OSMA diagram imply small degrees (10–15%) of partial melting. The common low Ti contents in the spinels of lherzolite rocks and gradual increase of Ti in spinel toward harzburgite and dunite also support relatively residual character. Arai (1987) and Cabanes and

Mercier (1988) suggested that primitive mantle peridotites contain olivine with Fo of 87.5–88.0 and spinel with Cr-number of 8–10; these values increase with the evolution of partial melting (Irvine, 1965, 1967; Dick and Bullen, 1984; Bonatti and Michael, 1989; Hellebrand et al., 2001). The Cr-number of spinel v.s Fo (Fig. 5 – 3) diagram in Pauza harzburgite shows that a fertile lherzolite 10-15 % of partial melting, becomes harzburgite at about 30 % melting and dunite at about 40 % melting (Fig. 5 – 3). Harzburgite in both Mawat and Penjwin peridotites with 30 % of partial melting becomes dunite at about 40 % melting. These result are consistent with the results of experiments on partial melting of upper mantle peridotite ((Jaques and Green, 1980; Duncan and Green, 1980, 1987; Bonatti and Michael, 1989; Kostopoulos, 1991).

5-5 Tectonic setting

Bonatti and Michael (1989) stated that the bulk composition of the mantle peridotites and the modal and elemental compositions of constituents minerals are dependent on the geotectonic environment of their formations. Cr-number in spinel is also a good indicator of the tectonomagmatic history of the host rock. The spinel in the lherzolite has low Cr-number < 60, typical of oceanic ophiolites (including back-arc basins; Dick and Bullen, 1984), while the magnesiochromite–olivine and the chromite–olivine compositions in both harzburgite and dunite respectively, lie near or within the olivine–spinel mantle array and are consistent with a SSZ origin (Figs. 5 – 3 and 5 – 4). The chromites in dunite are higher in Cr-number, that is analogous to those from both Alpine type and arc-related peridotites (Dick and Bullen, 1984).

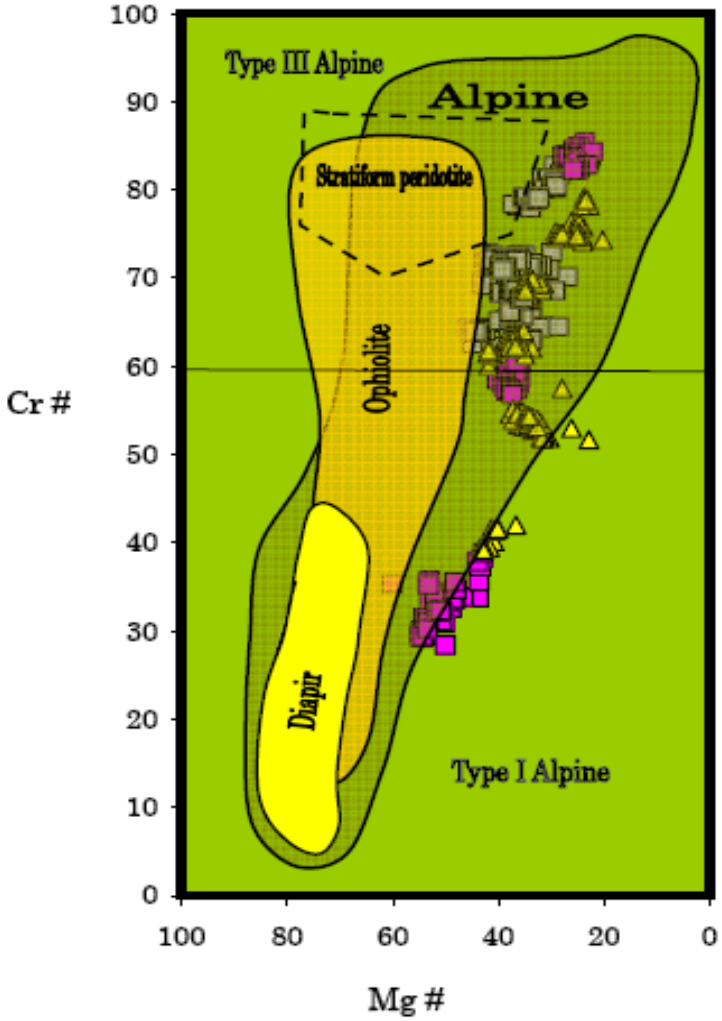

Fig. 5 – 1: Chromian spinel compositions plotted on Cr# vs. Mg#. Fields aftrer (Raymond, 2002). Pink boxes are Pauza, yellow triangles are Penjwin and gray boxes are Mawat peridotites

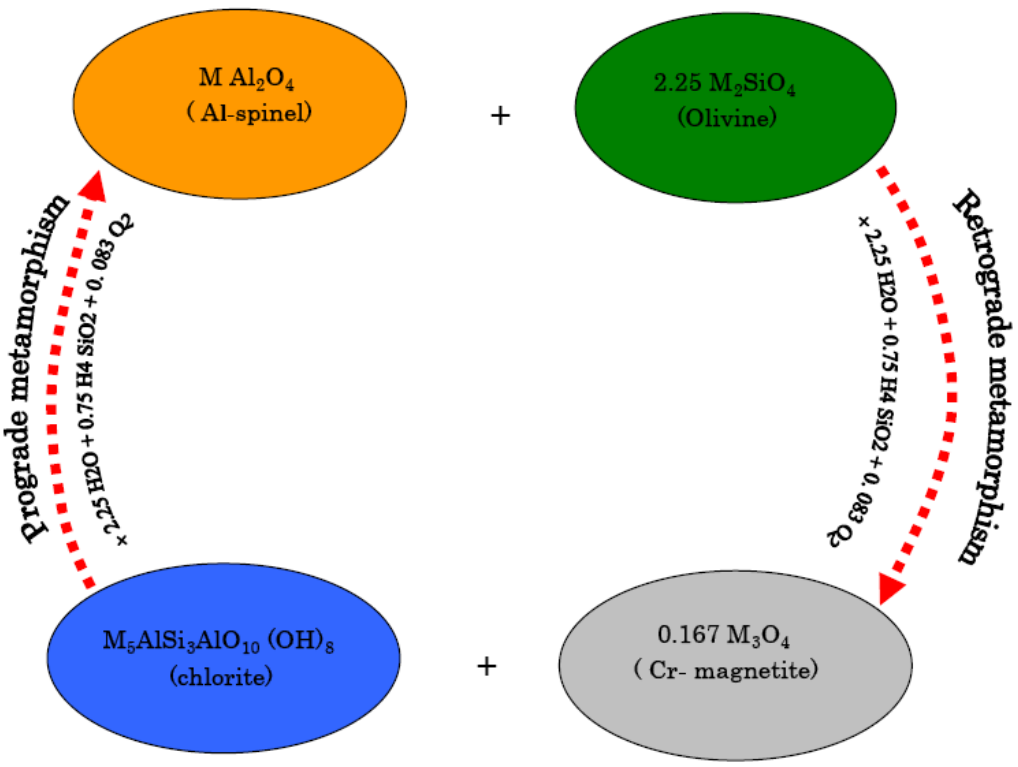

Fig. 5 – 2: Cyclic metamorphism of chromian spinel in harzburgite.
M = (Mg,Fe)

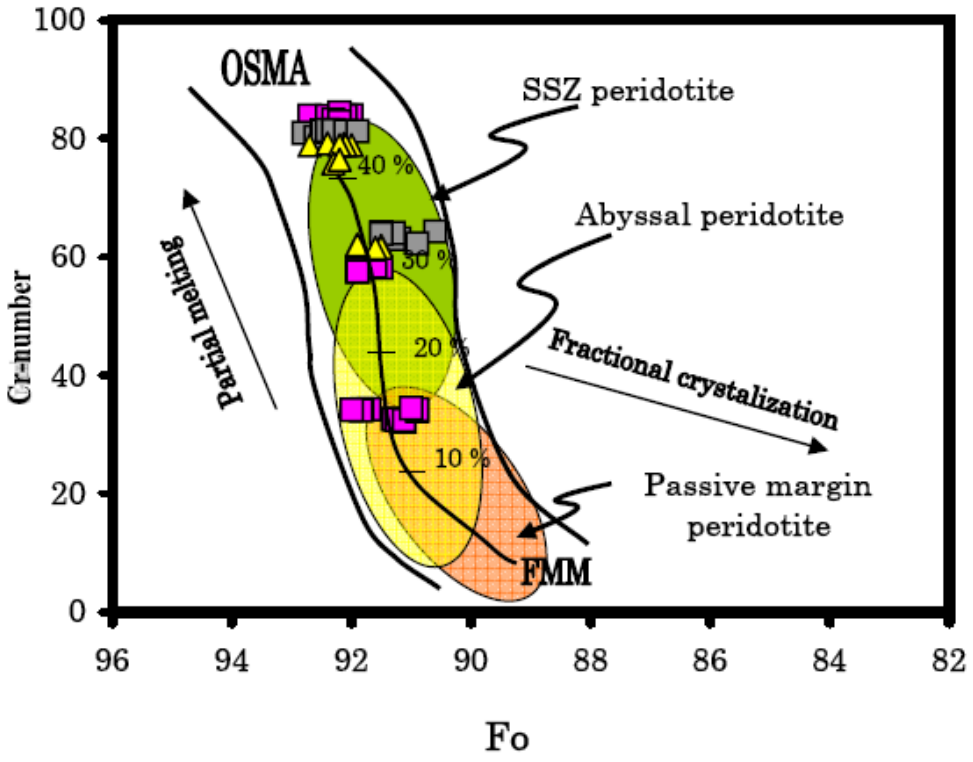

Fig. 5-3: Cr-number in spinel vs. Fo content of olivine in ultramafic rocks from IZTZ. Fields for spinels occurring in abyssal (and oceanridge),oceanic SSZ and passive margin peridotites are after Dick and Bullen (1984) and Pearce et al. (2000). OSMA field after Arai (1994). Pink boxes are Pauza, gray boxes are Mawat, and yallow triangles are Penjwin peridotites. OSMA: olivine–spinel-mantle array; FMM: fertile mantle composition.

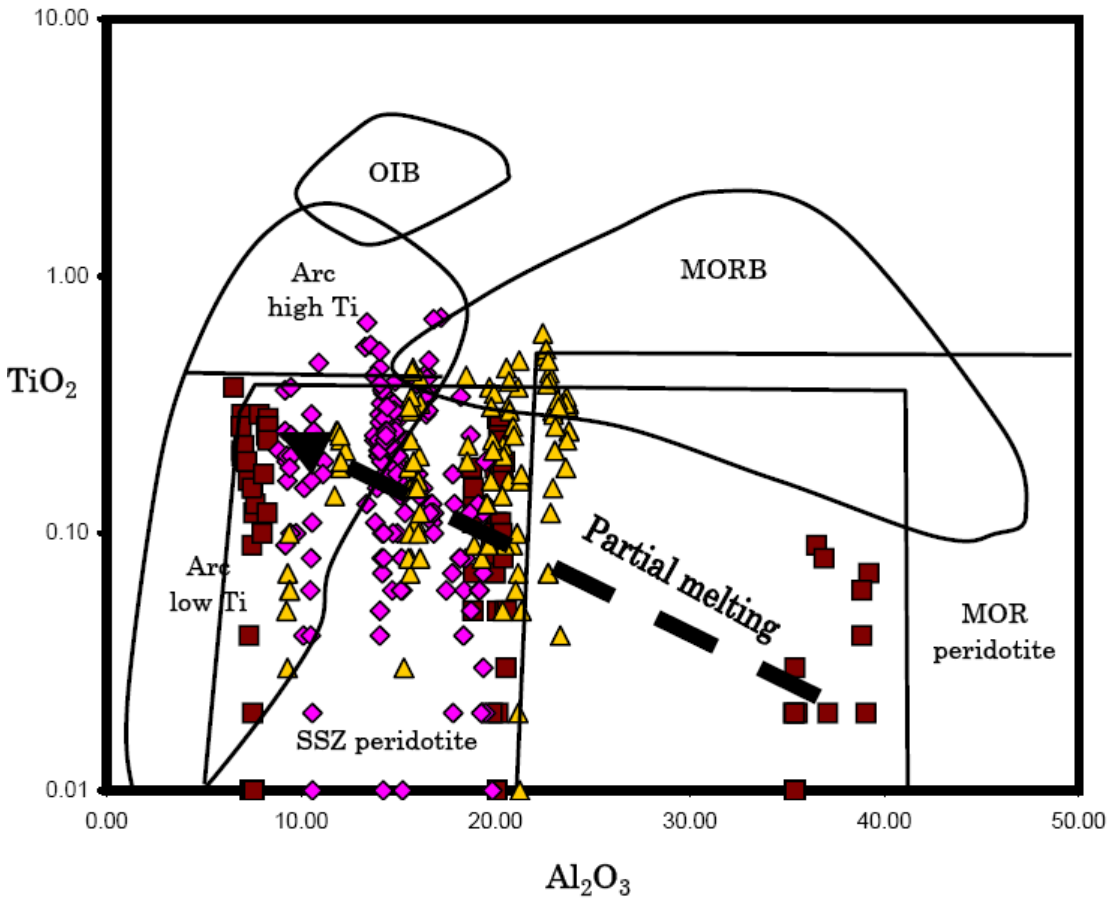

Fig. 5 – 4: Chromian spinel compositions plotted on TiO_2 vs. Al_2O_3 tectonic discrimination diagram. Fields for arc volcanic rocks, supra-subduction zone (SSZ), ocean island basalts (OIB), and MORB basalts and peridotites after Kamenetsky et al. (2001). Brown boxes are Pauza, yellow triangles are Penjwin and pink diamonds are Mawat peridotites

Chapter 6

Related rock

6-1 Field and petrographic observations

The albitite occurs as an isolated pod (4 m^2 in dimension) within the tectonized and serpentinized peridotite of the Penjwin ophiolite sequence (Fig. 6 – 1 A). The albitite is concentrically zoned from the host rock to the center of the pod (Fig. 6 – 1 B). In Figure 1B, A represents the sheared serpentinite, which consists mainly of the serpentine minerals lizardite and chrysotile as early phases and antigorite as a later recrystallized phase with a subordinate amount of carbonate minerals. B shows the chlorite-rich blackwall zone, which consists of alternating bands of chlorite and carbonate minerals (Fig. 6 – 2 A). The chlorite bands include some euhedral grains of magmatic zircon, highly fractured apatite, and subhedral fine-grained titanite grains (Type I). C shows the grossular–prehnite zone, which consists mainly of grossular garnet with prehnite (Fig. 6 – 2 B), ilmenite, zoisite, and magnetite. Grossular replaces Ca-plagioclase as a result of rodingitization (early rodingitization stage) of plagiogranite during serpentinization of host rock (Mohammad 2004). Prehnite is a replacement after grossular. Ilmenite occurs as large (0.5 mm) highly fractured subhedral grains rimmed by thin metamorphic titanite (Type II). D shows the albite-tremolite zone, consisting of highly fractured and mylonitized albite with inclusions of analcime. Amphibole in this zone is represented by zoned acicular tremolite–actinolite of late rodingitization stage at the expense of grossular of early rodingitization stage. Tremolite–actinolite is rimmed by edenite during high pressure-temperature albitization stage. Ilmenite occurs as highly-fractured coarse grains with titanite rim (Fig. 6 – 2 C), or is completely replaced by titanite (Type III) (Fig. 6 – 2 D), or is rimmed by a thin rim of rutile (Fig. 2E). E is the albite zone, which consists of large euhedral plagioclase (0.5 mm) (Figs. 6 – 2 F,G) and chessboard albite with some large euhedral patchy-zoned allanite, apatite, strontium apatite, sheaf-like barium muscovite, and large euhedral zoned zircon (Fig. 6 – 2 H). Pseudomorphs after biotite are also present in albite zone. The oscillatory zoned character of both

plagioclase (Figs. 6 – 2 G,H) and zircon suggest an origin via magmatic crystallization.

6 - 2 Mineralogy

6-2-1 Plagioclase

Based on optical petrography and BSE analysis, four types of albite were distinguished. They were thought to reflect multiple sources and origins. Representative chemical analyses of various types of albite are given in Table 6 - 1.

(1) Magmatic albite ($Ab_{97}An_2Or_1$) occurs as large euhedral to subhedral crystals, typically with oscillatory zoning. It shows plastic deformation fabrics such as kink bands and undulatory extinction, and also underwent later brittle fragmentation. Chemical analysis of euhedral plagioclase with concentric zoning does not show a large compositional range; that is, Ca contents are 2–3 wt. % richer in the core than in the rim. This zoning can be interpreted in three ways. First, direct crystallization from Na-rich magma could have occurred (e.g., Schwartz, 1992). Second, a primary zoned plagioclase could have changed to albite by metasomatism (e.g., Smith, 1974). Third, the occurrence of fine inclusions of grossular in albite may suggest the breakdown of calcic plagioclase to form garnet and albite.

(2) Chessboard albite ($Ab_{99}An_1$) occurs as large euhedral to subhedral grains surrounded by magmatic albite. It has been reported from keratophyres (Battey, 1995; Carstens, 1966), granite (Gilluly, 1933; Anderson, 1982), and plagiogranite (Dubińska et al., 2004; Kaur and Mehta, 2005). In these occurrences, the chessboard albite is considered to have replaced potassium feldspar during metamorphism or metasomatism. The lack of either K-feldspar components or inclusions of K-feldspar in the chessboad albite suggests igneous origin.

(3) Albite after Ca-bearing plagioclase ($Ab_{97}An_3$) occurs around ilmenite. It is interpreted that have undergone titanitization during the albitization process, because Ca-bearing plagioclase is the only source of

Ca in titanite, and the titanite is the reaction product of Ca-bearing plagioclase with ilmenite (Harlov et al., 2006):

(4) Albite ($Ab_{99}An_1$) with inclusions of analcime. The albitites always lack quartz. Inclusions of analcime without quartz in albite may represent the retrograde products of original jadeite inclusions. We think that this type is formed after jadeite during retrograde metamorphism according to the following reactions:

$NaAlSi_2O_6$ (jadeite) + SiO_2 (quartz) = $NaAlSi_3O_8$ (albite with jadeite inclusion).(1)

$NaAlSi_3O_8$ (albite contain jadeite inclusion) + H_2O = $NaAlSi_3O_8$ (albite with analcime inclusion). (2)

6-2-2 Titanite

Representative analyses of titanite are given in Table 6 - 2. According to the Fe–Al titanite discrimination diagram of Kowallis et al. (1997), all titanite types (I, II, and III) plot in the field of metamorphic titanite (Fig. 6 - 3). As titanite contains high amounts of Ca, it is most commonly found in Ca-rich rocks. Several authors have observed that the Ca/Al ratio of a melt precludes the presence or absence of titanite in igneous rocks. High Ca activity in the melt favors crystallization of titanite over other phases, according to the following reactions:

2 $FeTiO_3$ (ilmenite) + SiO_2 (quartz) + CaO = $CaTiSiO_5$ (titanite) + $TiFe_2O_4$ (ulvospinel). (3)

$KAlSi_3O_8$ (K-feldspar) + 3 $FeTiO_3$ (ilmenite) + 3 SiO_2 (quartz) + 3 CaO + H_2O = 3 $CaTiSiO_5$ (titanite) + $KFe_3AlSi_3O_{10}$ $(OH)_2$ annite. (4)

whereas high Al activity in a melt favors the crystallization of phases other than titanite according to the following reaction:

3 $TiFe_2O_4$ (ulvospinel) + 3 SiO_2 (quartz) + 3 $CaTiSiO_5$ titanite + 3 Al_2O_3 = 3 $CaAl2Si_2O_8$ (anorthite) + 6 $FeTiO_3$ (ilmenite). (5)

Plagioclase and ilmenite are the original magmatic phases in the rock, so the original magma that crystallized into plagiogranite was rich in Al and poor in Ca, and preferentially crystallized the phases on the right side of the reaction (5). Accordingly, all titanites in the samples studied are metamorphic in origin. On the basis of their chemical compositions and textural relationships with other phases, metamorphic titanite has been subdivided into three types (I, II and III) as follows:

6-2-2-1Type I titanite

Type I of titanite occurs as fine-grained crystals (0.01 mm in diameter) within chlorite after biotite in the albite zone (Fig. 6 – 4 A). The chlorite formed during the chloritization of biotite during ocean-floor metamorphism or rodingitization of plagiogranite (Mohammad, 2004). Although K_2O contents in chlorite are nearly zero and no trace of biotite has been recorded, pseudomorph shape and relict cleavage traces suggest that biotite was the primary phase. Textural evidence of titanite with coexisting phases (K-feldspar, muscovite, prehnite, and epidote in a chlorite matrix) suggests three possible reactions for the chloritization process of biotite during low-temperature metamorphism (Moore and Liou, 1979; Eggleton and Banfield, 1985; Enami et al., 1993). These reactions are as follows:

$$K_2Mg_{2.2}Fe^{2+}_{2.1}Fe^{3+}_{0.5}Ti_{0.5}Al_3Si_{5.6}O_{21.5}(OH)_{2.5} \text{ (biotite)} +$$

$$8.69\ CaAl_2Si_2O_8 \text{ (anorthite)} + 5.84\ K^+ + 4.37\ SiO_2 \text{ (quartz)} +$$

$$11.46\ H_2O + 8.19\ CO_2 =$$

$$3.95\ K_2Mg_{0.3}Mg_{0.3}Fe^{2+}_{0.2}Fe^{3+}_{0.1}Al_{4.9}Si_{6.5}O_{20}\ (OH)_4 \text{ (phengite)} +$$

$0.5\ CaTiSiO_5$ (titanite) + $0.05\ Fe_2O_3$ (hematite) +

$8.19\ CaCO_3$ (aragonite) + $5.84\ H^+$. (6)

biotite + 0.21 anorthite + $1.64\ H_2O$ + $1.46\ H^+$ + $0.082\ O_2$ =

0.46 chlorite + 0.11 titanite + 0.10 epidote + 0.56 muscovite +

0.63 quartz + 0.02 magnetite + $1.46\ K^+$. (7)

$K_{1.88}\ (Mg,Fe)_{5.02}Ti_{0.44}Al_{2.74}Si_{5.51}\ O_{20}(OH_{4-x},F_x)$ (biotite)+

$1.64\ CaAl_2Si_2O_8$ (anorthite) + $1.88\ SiO_2$ (quartz) + $2.97\ H_2O$ =

$0.80\ CaTi_{0.55}Al_{0.44}\ (OH_{0.45-1.25x},\ F_{1.25x})O_{0.55}SiO_4$ (titanite) +

$0.55\ (Mg,Fe)_{9.19}Al_{5.38}Si_{5.43}(OH)_{16}$ (chlorite)+

$0.42\ Ca_2Al_2Si_3O_{10}(OH)_2$ (prehnite) + $1.88\ KAlSi_3O_8$ (K-feldspar). (8)

Because of the absence of magnetite within chloritized biotites, reaction (8) is more realistic than the other two reactions.

6-2-2-2 Type II titanite

This type of titanite, found in the grossular–prehnite zone, occurs as a thin rim around ilmenite (Figs. 6 – 4 B and 6 – 4 C) that is entirely surrounded by grossular garnet. Titanite is interpreted to be a by-product of several reactions. It is suggested that the original Ca-plagioclase in plagiogranite underwent albitization during the dissolution of quartz by alkaline (Na-rich) solutions. The Na-rich fluids were introduced during serpentinization. The soluble sodium silicate reacted with calcic-plagioclase to form albite. This was accompanied by a reaction involving calcic-plagioclase to produce grossular. The reactions are as follows:

$2\ CaAl_2Si_2O_8$ (anorthite) + Na_4SiO_4 (Na-soluble silicate) + $7\ SiO_2$ =

$4\ NaAlSi_3O_8$ (albite) + 2 CaO. (9)

$CaAl_2Si_2O_8$ (anorthite) + 2 CaO + SiO_2 = $Ca_3Al_2Si_3O_{12}$ (grossular). (10)

Rearrangement of the reactions suggests that Ca-plagioclase changes to grossular and albite by the addition of Na-soluble silicate, which is formed by the dissolution of quartz. The reaction is:

$3\ CaAl_2Si_2O_8$ (anorthite) + Na_4SiO_4 (Na-soluble silicate) + $8\ SiO_2$ =

$4\ NaAlSi_3O_8$ (albite) + $Ca3Al_2Si_3O_{12}$ (grossular). (11)

Alternatively, the occurrence of fine grossular grains within the center of zoned plagioclase suggests that the original Ca-plagioclase may have broken down under high-pressure conditions to form albite and grossular (OBrien and Rötzeler 2003; Krenn and Finger 2004).

During subsequent high-pressure metamorphic events, the grossular became unstable and reacted with the rutile rim around ilmenite or with ilmenite to form titanite and clinozoisite, as shown in the electron microprobe traverse (Fig. 6 – 5). The formation of this type of titanite can be expressed according to the following reactions:

$3\ Ca_3Al_2Si_3O_{12}$ (grossular) + $5\ TiO_2$ (rutile) + $2\ SiO_2$ (quartz) + H_2O =

$5\ CaTiSiO_5$ (titanite) + $2\ Ca_2Al_3Si_3O_{12}$ (OH) (clinozoisite). (12)

$3\ Ca_3Al_2Si_3O_{12}$ (grossular) + $5\ FeTiO_3$ (ilmenite) + $2\ SiO_2$ (quartz) +

$H_2O + 1.25\ O_2 = 5\ CaTiSiO_5$ (titanite) + $2\ Ca_2Al_3Si_3O_{12}$ (OH)

(clinozoisite) + $2.5\ Fe_2O_3$. (13)

6-2-2-3 Type III titanite

Type III titanite, found in the albite–tremolite zone, occurs as highly fractured coarse grains (0.1 – 0.2 mm) containing fine inclusions (0.01 mm) of ilmenite (Fig. 6 – 4 D). It is completely surrounded by albite, analcime, and fine-grained chlorite. The electron microprobe traverse in Figure 6 – 6 suggests that titanite is located along the reaction boundary between ilmenite and Na-plagioclase. This type of titanite is interpreted to have been contemporaneous with the albitization process of Ca-plagioclase and titanitization of ilmenite (Harlov et al., 2006). This process results in increased albite component of plagioclase and/or the formation of analcime and titanite with fine-grained chlorite. The sources of Ca in titanite can only come from the breakdown of Ca-plagioclase (Fig. 6-7).

6-2-3 Amphibole

The representative analyses of amphibole are given in Table 6 – 3. Amphiboles display compositional zoning, with Al_2O_3 increasing gradually from the core to the rim (Fig. 6 – 8), and FeO and MgO decreasing toward the rim. According to the classification of amphiboles by Leake et al. (1997), the cores of amphibole are tremolite-actinolite, whereas the rims are edenite.

6-2-4 Apatite

The albitites contain as much as 3 vol. % apatite. Apatite occurs as large subhedral grains, and is commonly highly fractured. It contains inclusions of patchy zoned allanite and fine inclusions of Sr-apatite. Large

apatite grains, characterized by blue, contain low SrO contents (< 0.1 wt. %), and lack SiO_2 (Table 6 – 4). EDS analysis suggests that a small amount of chlorine is present, possibly representing Cl-apatite of Deer et al. (1992). The Sr-apatite inclusions contain > 50 wt.% SrO and as much as 4 wt.% SiO_2. Because the presence of SiO_2 in the apatite structure requires a coupled substitution of Si^{4+} for P^{4+} and Na^{+} or REE to Ca^{2+}, the Sr-apatite contains a large amount of Na_2O. Similar Sr-bearing apatite has been recorded in high-pressure metamorphic rock (e.g., Krenn and Finger, 2004) and kimberlite (e.g., Chakhmouradian et al., 2002).

6-2-5 Allanite and analcime

Allanite occurs as a large anhedral grain or as an inclusion in both ilmenite and apatite, and always shows patchy zoning. Allanite is of the Ce-allanite type; it contains >12 wt. % of CeO, 8 wt. % of LaO_2, and 3 wt. % of NdO_2 (Table 6 – 5). Analysis of X-ray maps and BSE images indicate significant REE substitutions for Ca and Fe substitution for Al in allanite, as suggested by Gieré and Sorenson (2004) (Fig. 6 – 9, 6 – 10).
Analcime is found as a vein-filling or as inclusions in albite. Compositions of analcime are given in Table 6 – 6. It is a hydrous equivalent to jadeite.

6-2-6 Barian Mineral

Barium muscovite, celsian, and cymrite are representative barian minerals found in albitite pods in the study area. The compositions of these minerals are given in Tables 6 – 7 and 6 – 8. Barium muscovite

contains as much as 10 wt. % BaO. It is typically zoned with BaO increasing and K_2O decreasing from core to rim (Mohammad et al., 2007). Celsian and cymrite are characterized by high BaO content (37–41 wt. %) (Table 6 – 8). Cymrite is a hydrous high-pressure equivalent to celsian. It can be distinguished from the celsian based on composition; cymrite gives totals of < 97, whereas celsian gives totals ~ 100.

6-2-7 Pyroxene

Compositions of pyroxene are given in Table 6 – 9. According to Morimoto et al. (1988), pyroxenes are classified into diopside. They are concentrically zoned (Fig. 6 – 11), and have colorless core and pale yellowish-green rim.

6-3 Geothermobarometry

Euhedral zircon in the albitite pod is inferred to have been crystallized at a temperature of 1000 ± 100 °C based on Ti content (Avg. of Ti = 1500 ppm)(Watson et al., 2005) obtained by Laser albation-ICPMS. Based on calcic-amphibole thermobarometry of Ernst and Liu (1998), amphibole cores (actinolite-tremolite) represent low-temperature and low-pressure metamorphic conditions at the early prograde rodingitization stage of the plagiogranite, as shown in Figure 6 – 12. Toward the rim, the amounts of TiO_2 and Al_2O_3 increase with progressive albitization or with increasing Na_2O in the rock. Edenite was formed at the amphibole rim, representing the peak of albitization under high-pressure and high-temperature conditions (P = 1.5 GPa and T = 650 °C) (Fig. 6 – 12). This temperature is consistent with the results of the plagioclase-amphibole thermometry of Holland and Blundy (1994). Accordingly, the core is believed to have formed at T = 450 °C with a gradual increase to 750 °C at

the rim. Estimated pressure – temperature of metamorphic titanite formation conditions (Fig. 6 – 13) are best fit with the result of amphibole thremobarometry.

6-4 Whol rock geochemistry

Whole-rock analyses of five samples from the core of the albitite pod show that these rocks contain large amounts of SiO_2 (average 63.8 wt.%), Al_2O_3 (average 19.5 wt.%), and Na_2O (average 11.4 wt.%) (Table 6 – 10). They show enrichment in all REEs (Fig. 6 – 14 A, 6 – 14 B). Spatially, light REE concentration is ~100× chondrite, middle REE is 10× chondrite, and heavy REE is 7× chondrite. The Eu anomalies may relate to original Eu anomalies in the albitite protolith or mobility of this element during chessboard albite formation from feldspar or Ca-plagioclase. Similar REE patterns with Eu anomalies were recorded in Slavezines massif albitite in France and the albitite deposits from Central Sardinia, Italy (e.g., Boulvais et al., 2007; Castorina et al., 2006). For chemical classification, oxide weight percents were plotted in the CNK (CaO Na_2O K_2O) diagram (Fig. 6 – 15) of Glikson (1979) and normative albite (Ab), anorthite (An), and orthoclase (Or) were plotted on an An-Ab-Or ternary diagram (Fig. 6 – 16) (Barker, 1979). In both diagrams, the samples are plotted in the trondhjemite field. Typical plagiogranites worldwide plot in the fields of trondhjemite and tonalite (e.g., Coleman and Peterman, 1975; Rao et al., 2004; Kaur and Mehta, 2005). On the A/CNK-A/NK [A/CNK – Al_2O_3/(CaO Na_2O K_2O)]diagram (Fig. 6 – 17 A) of Shand (1943), albitized plagiogranite is located in the peraluminous field and tends to be Al saturated with an A/CNK close to 1, which is the value of albite. In SiO_2/Al_2O_3-A/CNK (Fig. 6 – 17 B) of Kaur and Mehta (2005) and K_2O-SiO_2 diagram (Fig. 6 – 18) of Coleman and Peterman (1975), Mlakawa albitized plagiogranite is located in the field of high aluminous oceanic plagiogranite. Although the rock underwent loss and gain of Na_2O, CaO and Al_2O_3 compared with typical plagiogranite, differences are not large enough to shift the position of the Mlakawa albitite protolith from the plagiogranite field to other fields.

6-5 Discussion

The geochemical data from the albitite pod, the estimated temperature of zircon formation, and the textures preserved in the rock indicate that the protolith of Mlakawa albitite was igneous in origin. Furthermore, the intimate association with ultramafic rocks of the ophiolite suite suggests a plagiogranite origin for the albitites. Previous workers have considered that a high degree of fractional crystallization of a subalkaline low-potassium tholeiitic magma was primarily responsible for petrogenesis of plagiogranite (e.g., Coleman and Peterman, 1975; Engel and Fisher, 1975; Coleman and Donato, 1979; Saunders et al., 1979; Aldiss, 1981; Kontinen, 1987; Borsi et al., 1996; Kaur and Mehta, 2005). The possibility that the Mlakawa albitite originated from an Na-rich magma, however, is rejected because of the lack of Na-rich igneous rocks in the ultramafic suite, except for plagiogranite. The formation of both blackwall and rodingite around albitite requires an influx of Ca and Mg during the serpentinization of the host rock. Because serpentine structure does not accommodate Ca, Ca is expelled into the fluid during the formation of lizardite and chrysotile from pyroxene in the early stage of serpetinization, and affects adjacent primary plagioclase of plagiogranite to produce a grossular rim according to the following reaction:

$CaAl_2Si_2O_8$ (plagioclase) + 2 CaO + SiO_2 = $Ca_3Al_2Si_3O_{12}$ (grossular). (14)

In a later stage of serpentinization (i.e., the albitization stage), antigorite was formed from lizardite and/or chrysotile. As the ratio of Mg/Fe tends to be higher in antigorite than in lizardite and/or chrysotile (Mohammad and Maekawa, 2007), the fluids come to be rich in Mg and react with the preexisting grossular rim of plagiogranite to form chlorite in blackwall, and to form prehnite and tremolite-actinolite in rodingite according to the following reactions (OHanley et al., 1992; OHanley, 1996; Hatzipanagiotou and Tiskouras, 2001):

3 grossular + H_2O + Mg = 2 prehnite + chlorite + 5 Ca. (15)

21 grossular + 3 chlorite + 25 CO_2 = 25calcite + 3 tremolite +

16 clinozoisite + H_2O. (16)

From the above reactions, it is clear that the serpentinization processes in the host rock, blackwall formation, and rodingitization of plagiogranite were contemporaneous. The lack of any vein or channel of albitite radiating from the albitite pod to the host serpentinite negates the possibility of precipitation from metasomatic fluids for the formation of Mlakawa albitite.

After the formation of plagiogranite within the ultramafic part of the Penjwin ophiolite sequence, the primary plagiogranite underwent rodingitization and blackwall formation during the early stage of serpentinization under the low-pressure and low-temperature metamorphic conditions in the oceanic stage. In that stage, the serpentinization proceeded to produce a lizardite-chrysotile assemblage at the expense of primary olivine and pyroxene in the host peridotite, and thereafter the rodingitization led to the formation of grossular at the expense of Ca-plagioclase in the plagiogranite. When the subduction of the Arabian plate beneath the Iranian plate was initiated in the middle Cretaceous, the rocks progressively underwent (early) high-pressure and low-temperature metamorphism. Antigorite was formed at the expense of lizardite and chrysotile in the serpentinized peridotites. This metamorphic stage is recognized in plagiogranite by the progressive formation of tremolite-actinolite from grossular and the formation of celsian. Celsian is interpreted to be related to tremolite-actinolite formation during rodingitization because it is stable in a hydrous environment. This is consistent with rodingitization of plagiogranite and serpentinization of host rocks because the host rocks are interpreted to have been serpentinized by Ba-rich fluids. Thus, we conclude that the fluid responsible for serpentinization was Ba-rich, and the celsian was formed by the alteration of a plagiogranite pod by Ba-rich metasomatic fluid according to the following reaction:

$CaAl_2Si_2O_8$ (plagioclase) + Ba^{2+} = $BaAl_2Si_2O_8$ (celsian) + Ca^{2+}. (17)

Due to lack of K-feldspar in the rock, it is reasonable to consider that celsian was drived from Ca-plagioclase by the substitution of Ba for Ca. During the collision of the Arabian plate with the Iranian plate (later prograde metamorphism and progressive albitization), the pressure and temperature conditions increased, and the actionlite-tremolite changed to edenite and celsian to cymrite by the reaction:

$BaAl_2Si_2O_8$ (celsian) + H_2O = $BaAl_2Si_2O_8 \cdot H_2O$ (cymrite). (18)

The occurrence of barium muscovite suggests that the rock recrystallized under high-pressure conditions (e.g., Harlow and Olds, 1987; Kobayashi et al., 1987; Harlow, 1995). The occurrence of Ba-rich minerals as well as edenite suggests that the albitization of plagiogranite occurred within a subduction zone by the fluids derived from the subducting plate and from sediments just above the subducting plate. The fluids were squeezed out by dehydration, and were mixed with Na-rich seawater trapped in the sediment above the subducted slab. As Ba enrichment is common in marine sediments (Frondel and Ito, 1968; Morand, 1990), the source of Ba is probably related to the subducted sediments on top of the plate. Sr-apatite contains > 50 wt.% SrO and occurs as fine-grained euhedral crystal, as inclusions within apatite, and as thin rims around apatite. It is related to the high-pressure breakdown of plagioclase to form grossular and albite during the albitization. Krenn and Finger (2004) concluded that Sr-apatite in metamorphosed granite was formed under high-pressure metamorphic condition. The idea that the Sr may also come from the metasomatic fliud, however, was discarded because Sr contents in all samples of albitite were homogeneous regardless of their proximity to serpentinite. Furthermore, Sr-apatite was restricted to the area around apatite in the albitite core, whereas apatite in rodingite rim does not contain Sr-apatite. The multiple generations of chlorite and analcime were caused by multiple events from the oceanic stage to the retrograde stage just after the high-pressure metamorphism within the deep subduction zone. The chlorite was formed by chloritization of biotite in plagiogranite during rodingitization in the oceanic stage of

metamorphism. It was also formed during prehnite formation on the expense of grossular in the rodingite rim (e.g. ÓHanley et al., 1992). The occurrence of analcime was directly related to the metamorphism of albite or jadeite according to the following reactions:

$NaAlSi_2O_6$ (jadeite) + H_2O = $NaAlSi_2O_6 \cdot H_2O$ (analcime). (19)

$NaAlSi_3O_8$ (albite) + H_2O = $NaAlSi_2O_6 \cdot H_2O$ (analcime) + SiO_2 (Harlow, 1994). (20)

The albitite contains > 63 wt.% SiO_2 and includes considerable amounts of analcime, up to 20 vol%. However, quartz was not found in or near analcime crystals, so the first reaction was preferred to the second. The analcime was suspected to be formed directly from the alteration of jadeite during retrograde metamorphism.

Based on the above interpretations, it can be concluded that the serpentinization, rodingitization, and albitization processes observed in the Mlakawa albitite are complementary processes (Fig. 6 – 18). Each process has a specific effect during a particular time in the evolution of the ultramafic-plagiogranite part of the Penjwin ophiolite sequence, leading to the formation of the Mlakawa albitite. Both serpentinization of peridotite and rodingitization of plagiogranite represent low-temperature and low-pressure conditions during the oceanic stage and the subduction stage before collision of the Arabian plate with the Iranian plate. In contrast, the albitization of plagiogranite represents high-pressure and high-temperature conditions at the collisional stage of the Arabian plate with the Iranian plate during the Late Cretaceous period.

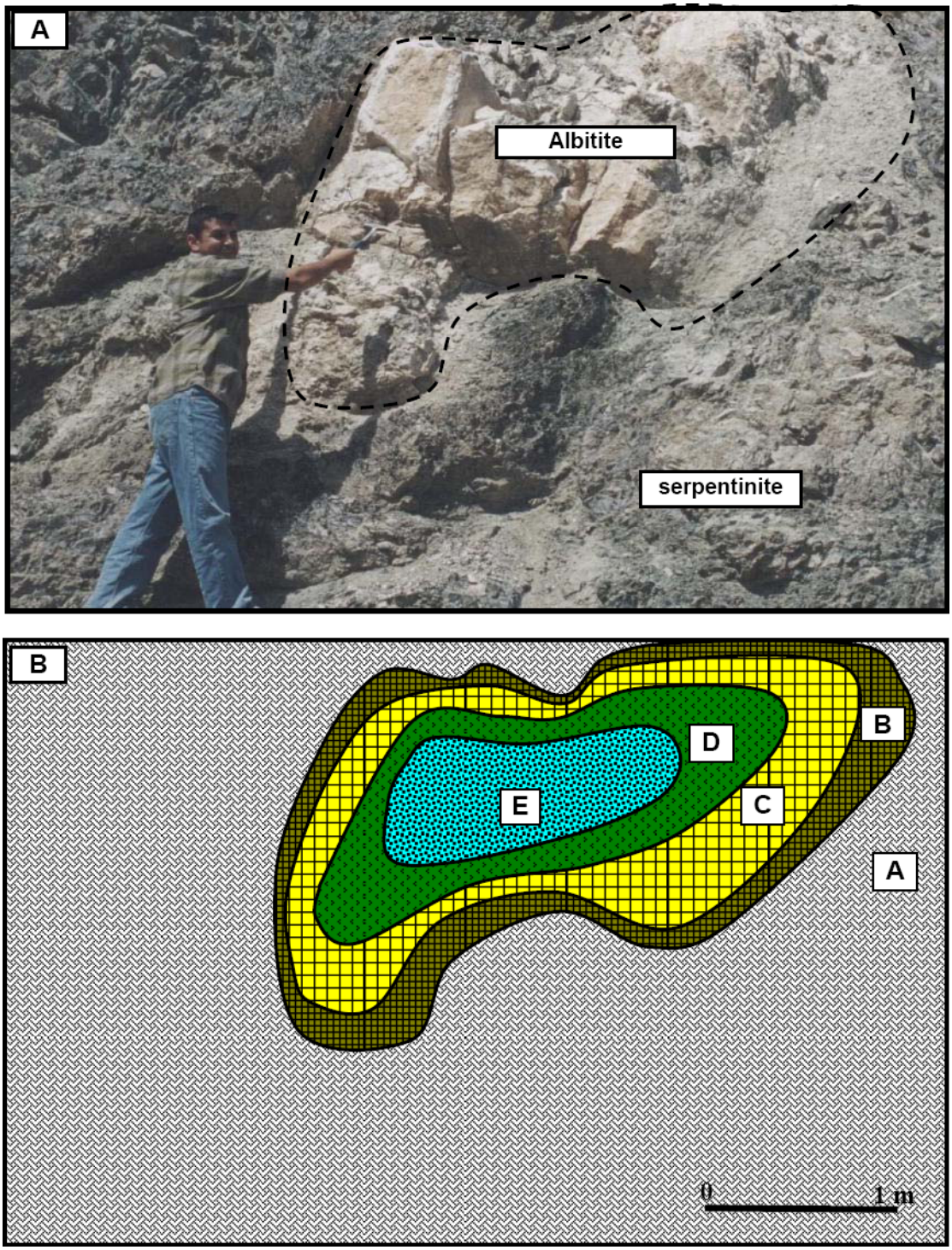

Fig. 6 – 1: A. Mode of occurance of the Albitite pod with massive serpentinite in the Penjwin igneous complex. B. Sketch showing different mineral zones in the metarodingite pod, A = serpentinite host rock, B = blackwall zone, C = grossular – prehnite zone, D = albite – tremolite zone, E = albite zone

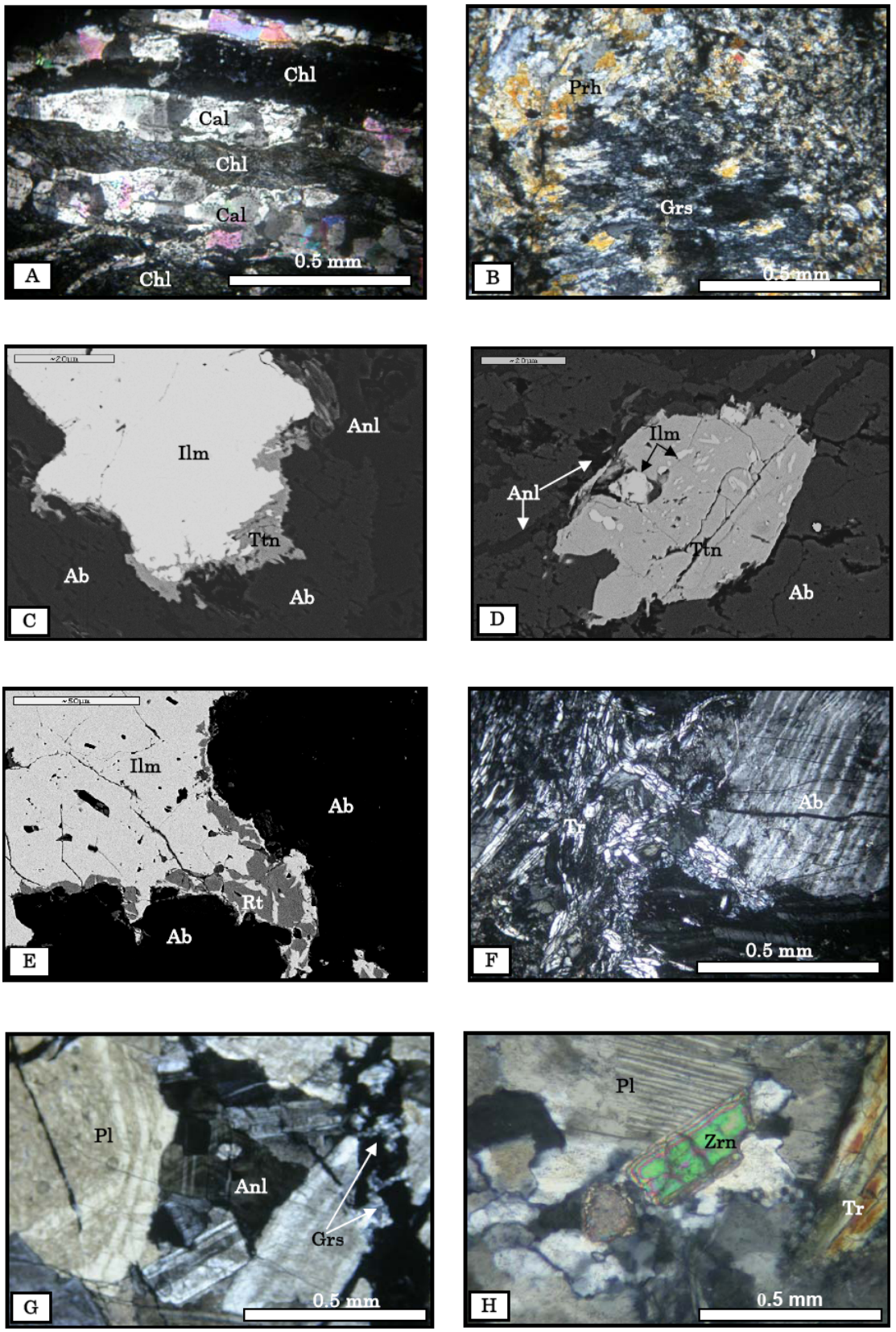

Fig. 6 – 2: Photomicrographs and images of various zones and minerals in the Albitite pod. **A**. Photomicrograph of blackwall zone show alternating bands of clinochlorite and carbonate minerals. **B**. Photomicrograph of grossular–prehnite zone sample showing the replacement of grossular by prehnite. **C**. Backscattered electron (BSE) image of a large grain of ilmenite rimmed by a thin rim of titanite in the albite–tremolite zone. **D**. BSE image of coarse-grained ilmenite, extensively affected by the titanitization process in the albite–tremolite zone. **E**. BSE image of a coarse-grained anhedral ilmenite rimmed by a thin rim of rutile in the albite–tremolite zone. **F**. Photomicrograph of partly mylonitized albite in the albite zone. **G.** Photomicrograph of coarse grain euhedral plagioclase preserving magmatic oscillatory zoning in the albite zone. **H**. Photomicrograph of a coarse-grained euhedral zircon grain, showing typical zoning indicative of magmatic origin. Mineral abbreviations after Kretz (1983), Chl = chlorite; Cal = calcite; Ilm = Ilmenite; Ab = albite; Ttn = titanite; Prh = prehnite; Grs = grossularite; Rt = rutile, Tr = tremolite-actinolite; Zrn = zircon; Pl = plagioclase; Anl = analcime.

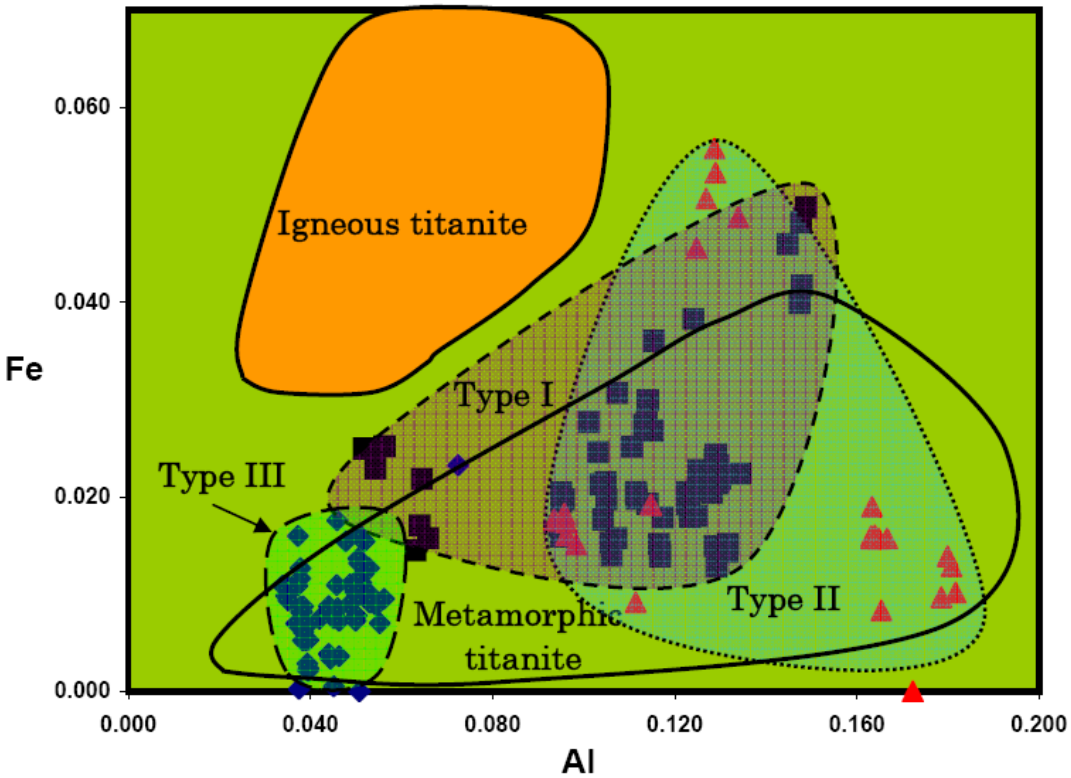

Fig. 6 – 3: Fe (apu) vs. Al (apu) titanite discrimination diagram, showing that all types of titanite (I, II and III) in the samples studied plot in the field of metamorphic titanite. The field of igneous and metamorphic titanites are after Kowallis et al. (1997).Read triangles are type II, black boxes are type I and blue diamonds are type III titanite

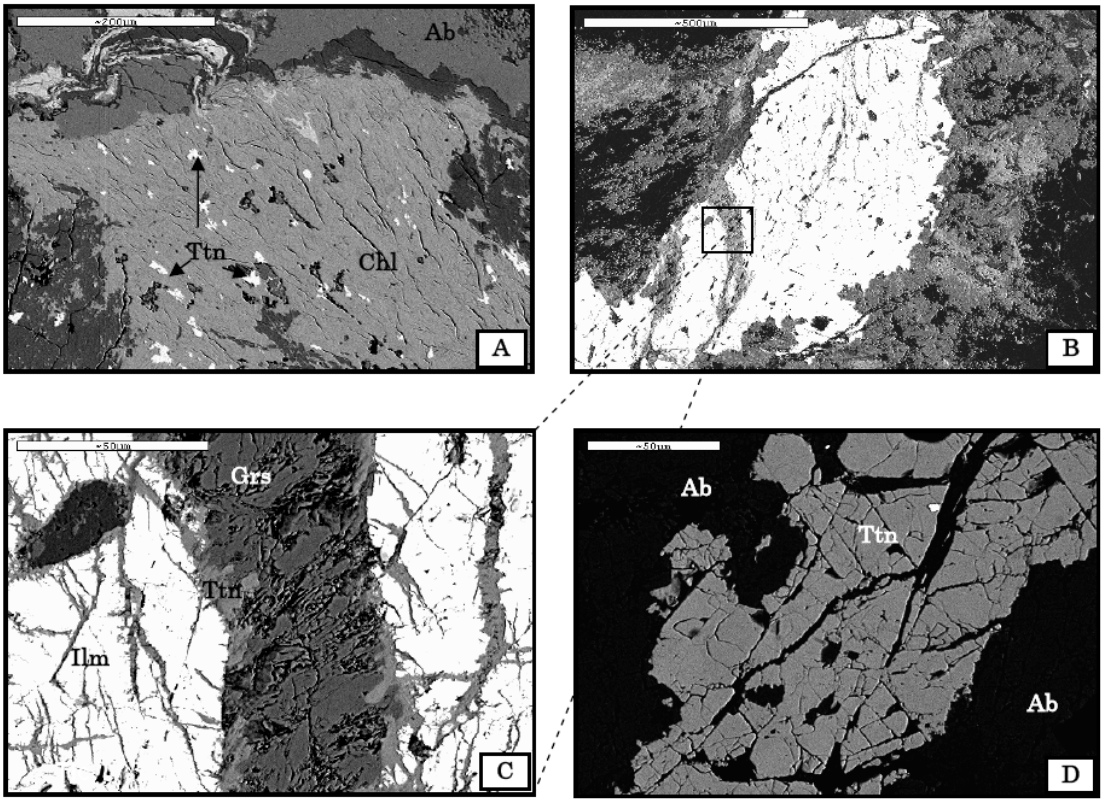

Fig. 6 – 4: Backscattered electron images of titanite and the surrounding phases in different zones of albitite. **A**. Fine grains of anhedral titanite as inclusions in chloritized biotite. **B–C.** Coarse grains of highly fractured ilmenite, rimmed by a thin rim of titanite that is entirely surrounded by grossular garnet. **D**. Coarse-grained, anhedral, highly fractured titanite completely surrounded by albite

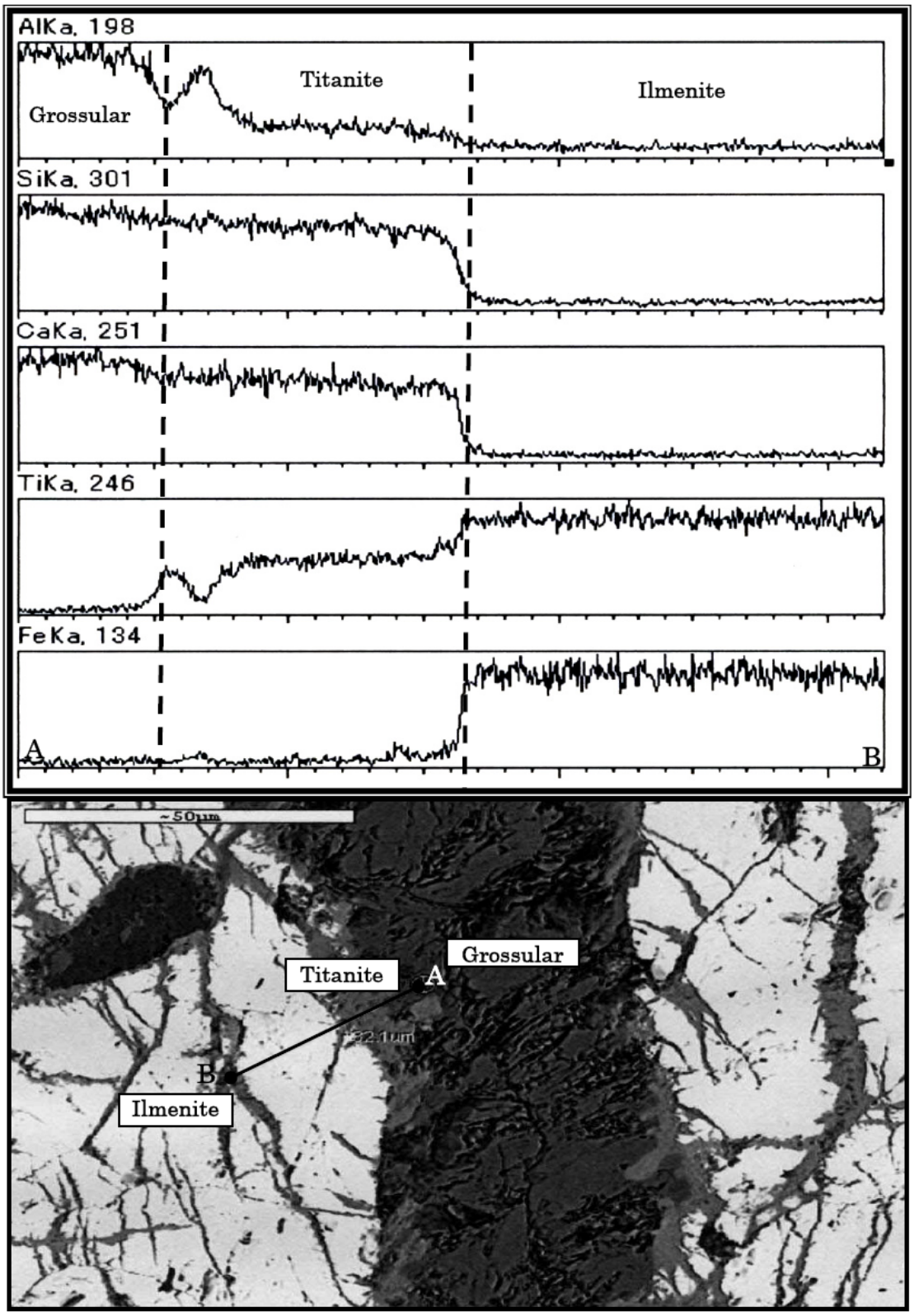

Fig. 6 – 5: Line scan profile across the reaction rim between grossular and ilmenite, illustrating the source of elements that are involved during titanite rim formation.

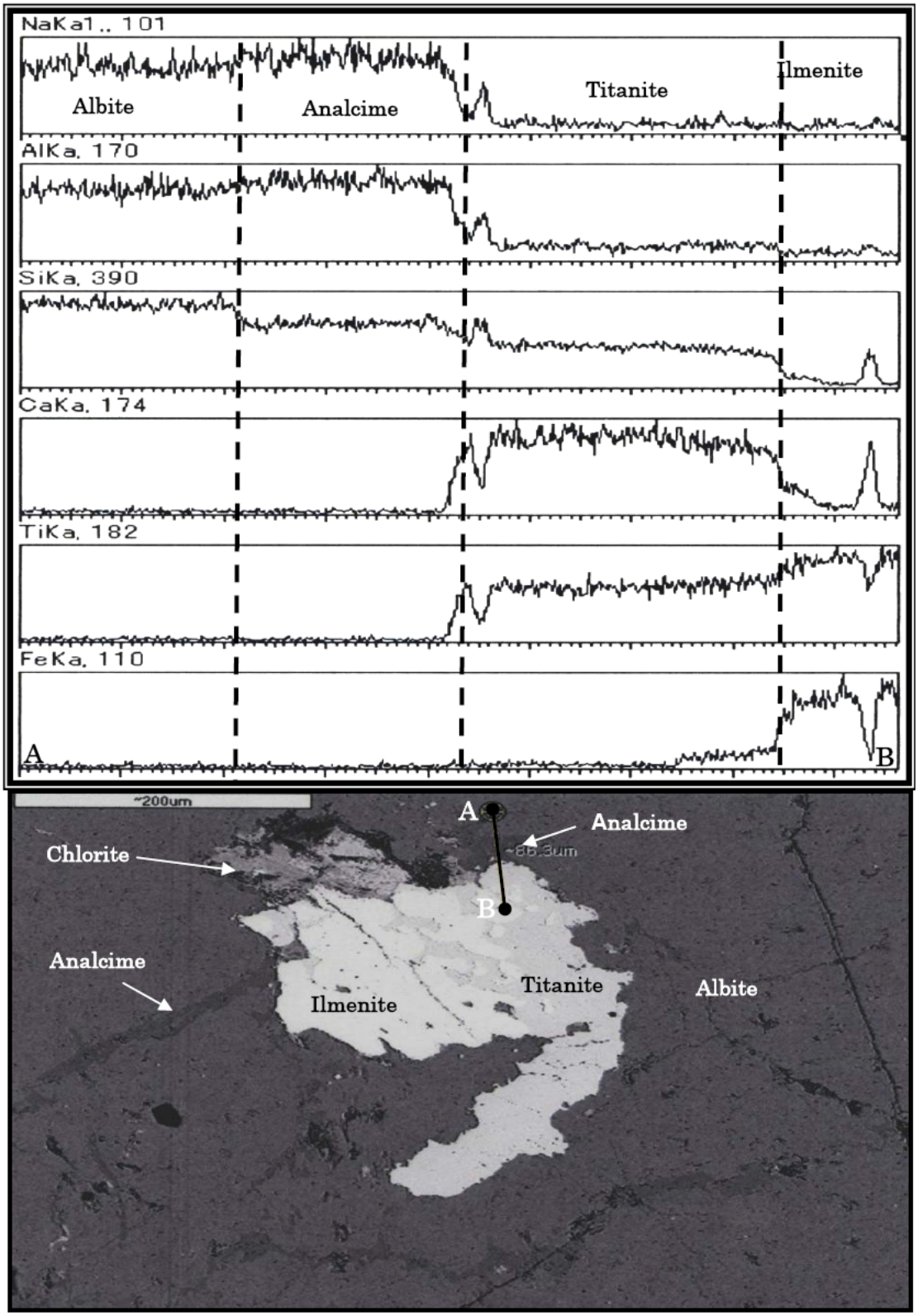

Fig. 6 – 7: Line scan profile across the reaction that leads to the formation of albite, analcime, titanite, and chlorite during interaction between Ca-plagioclase and ilmenite.

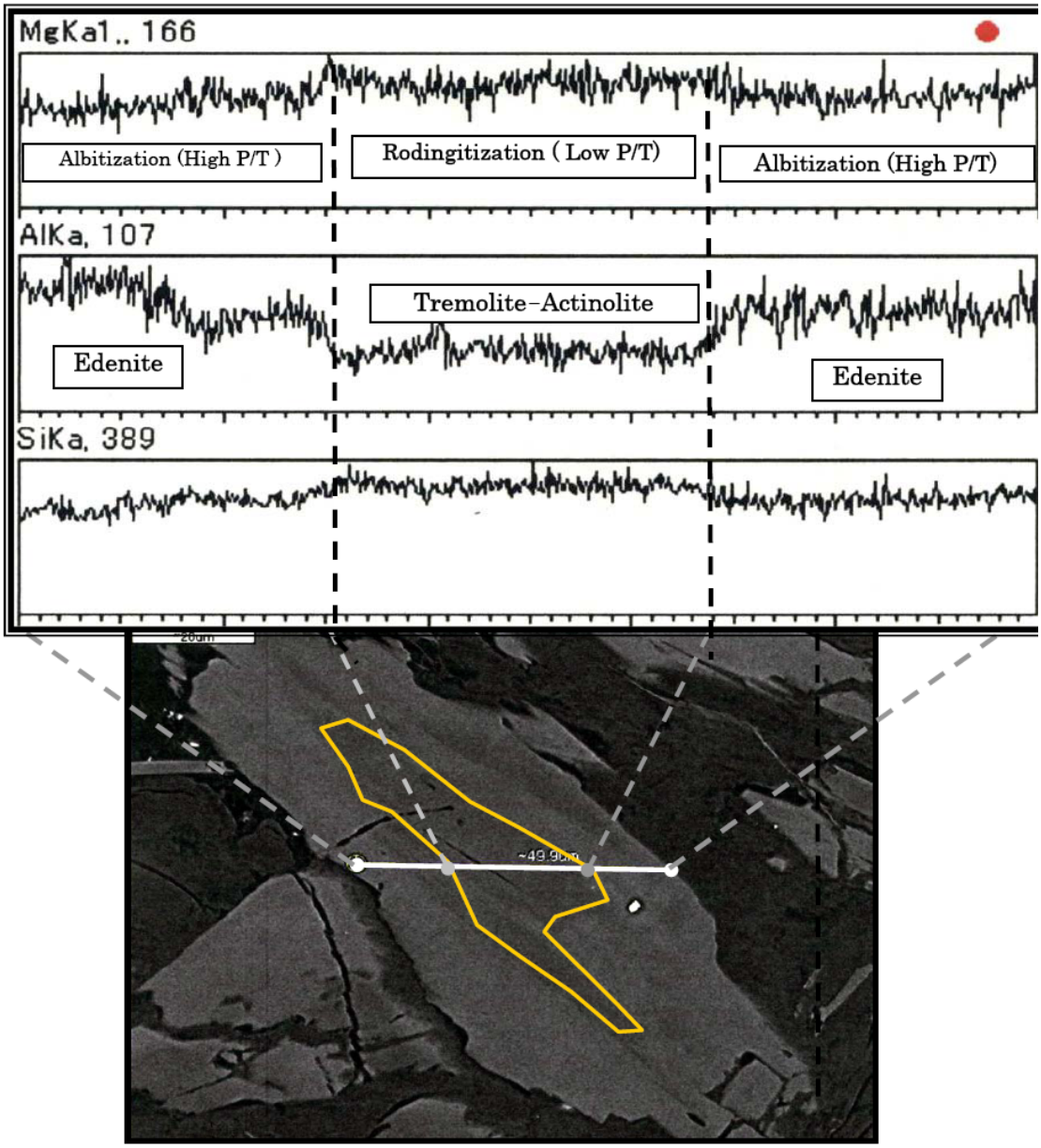

Fig. 6 – 8: Line scan profile of zoned amphibole in Mlakawa albitite, showing Mg-and Si-rich core and Al-rich rim. P/T- pressure-temperature.

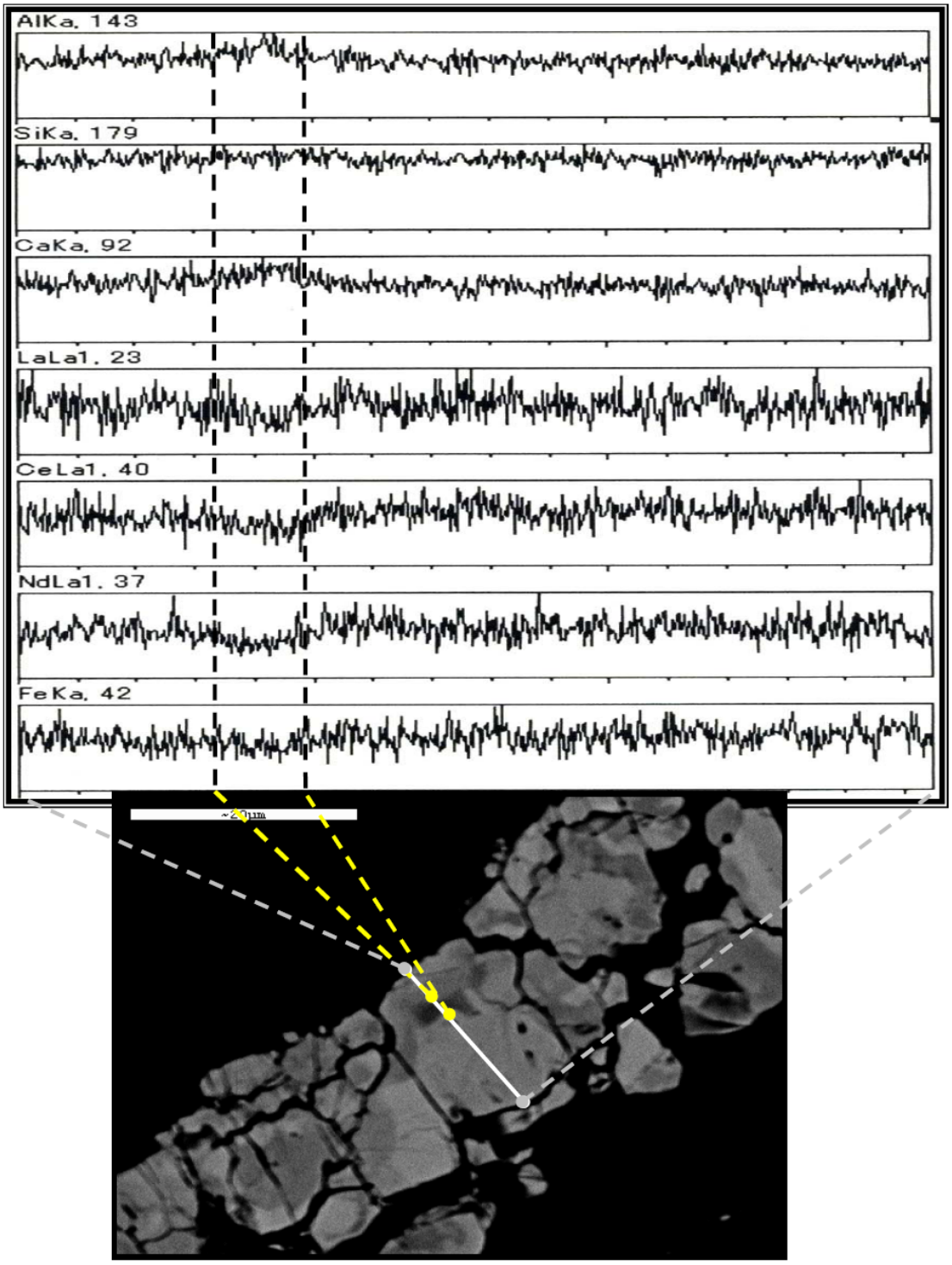

Fig. 6 – 9: Line scan profile of patchy-zoned allanite in Mlakawa albitite showing the substitution between Ca and rare earth elements (REE) in the allanite structure.

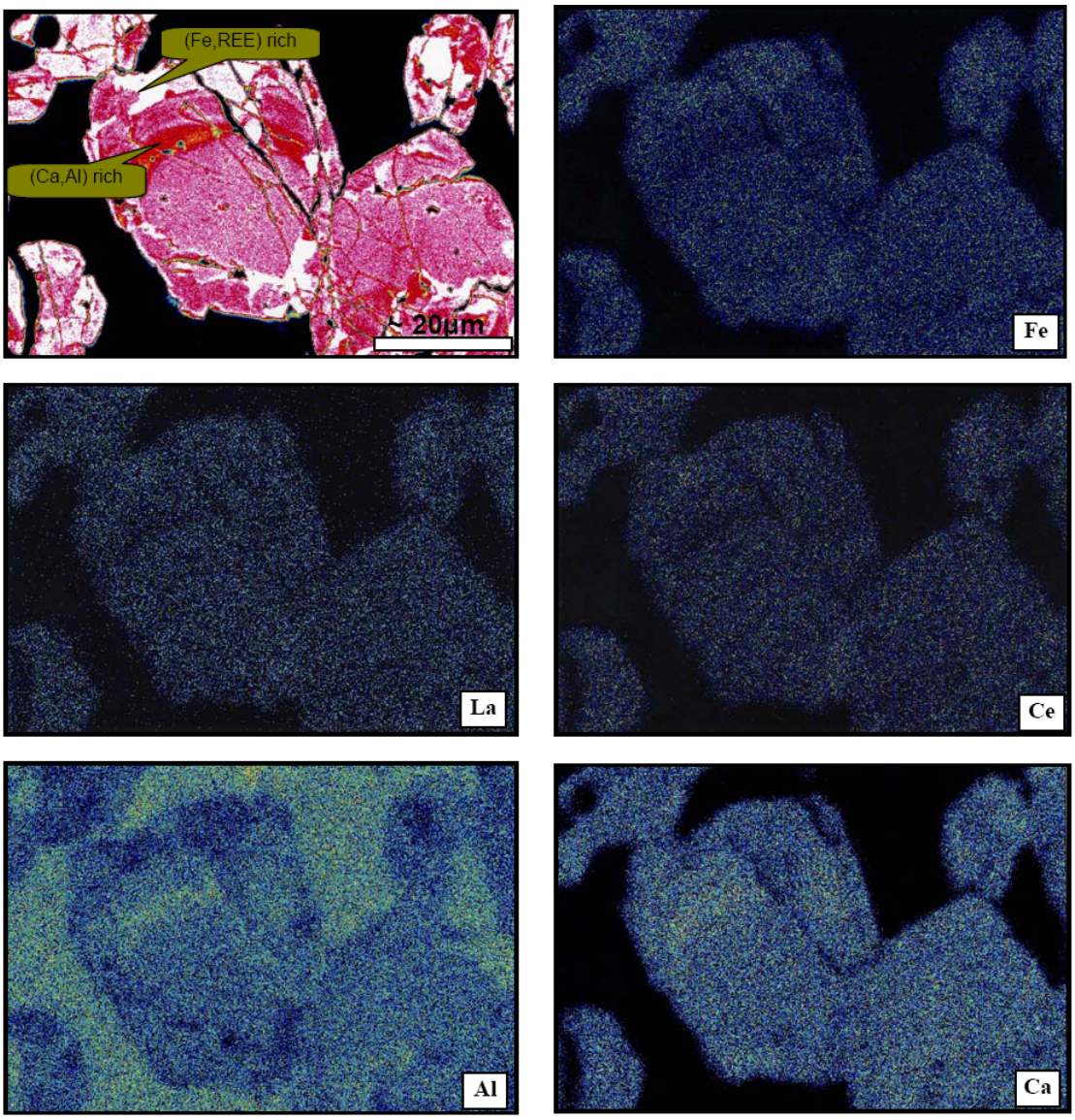

Fig. 6 – 10: X-ray mapping of Fe, Ce, La, Ca, and Al in allanite

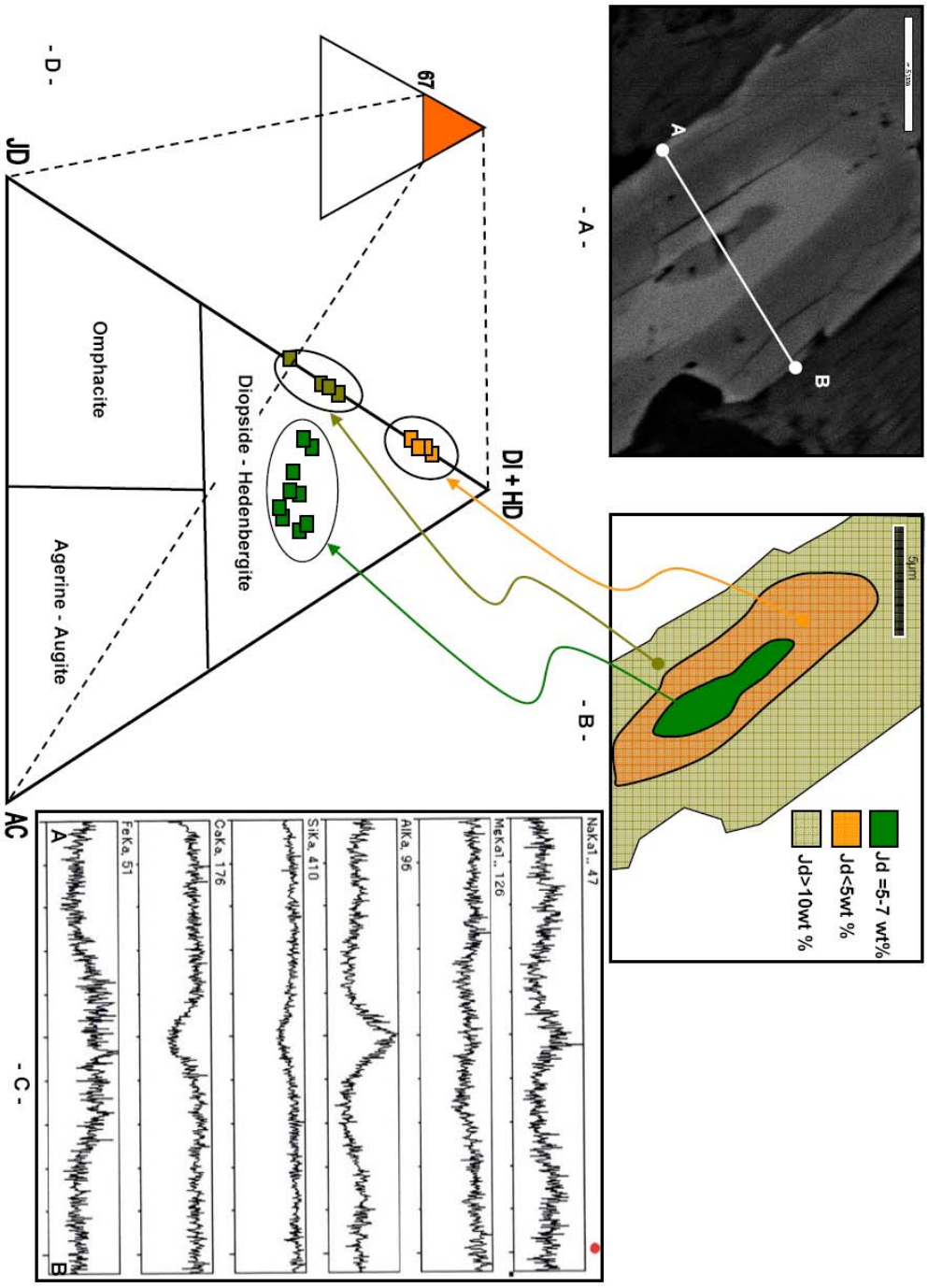

Fig. 6 – 11: (A) Backscatter electron image showing concentric-zoned pyroxene. (B) Sketch showing the variation of jadeite (Jd) content of pyroxene from core to rim. (C) Line scan profile of zoned pyroxene in Mlakawa albitite showing variations from core to rim. (D) Compositions of pyroxene in jadeite-acmite-diopside + hedenbergite ternary diagram. Green solid squares indicate core compositions, yellow solid squares indicate transitional zone compositions, and brown solid square indicates rim compositions.

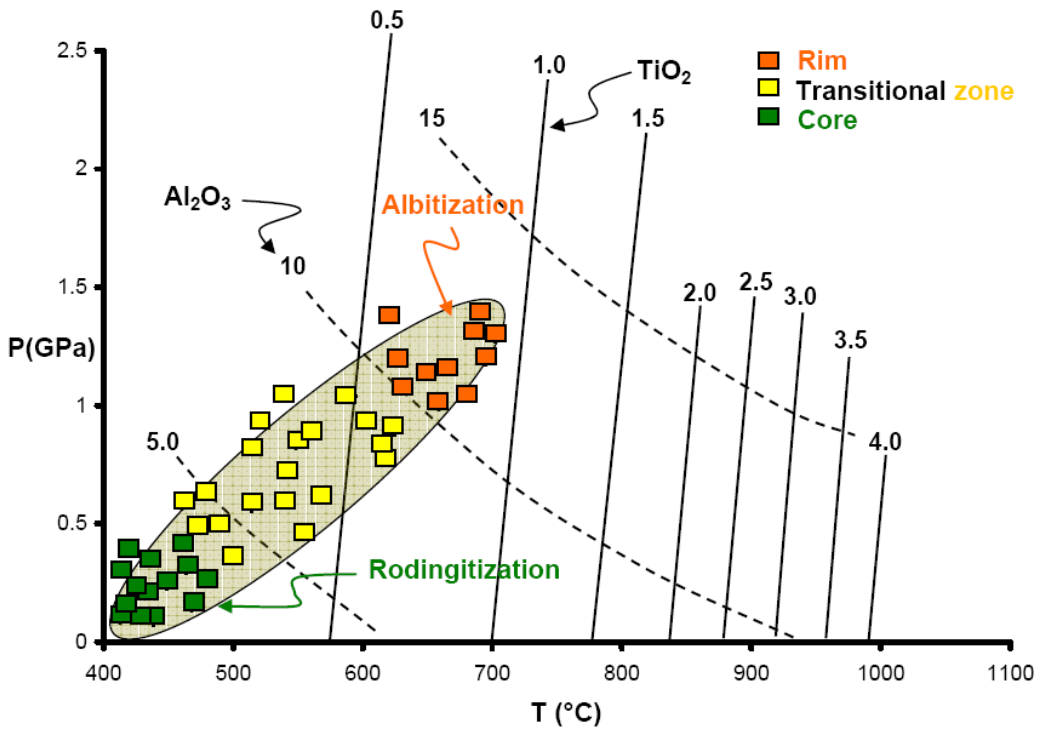

Fig. 6 – 12: Compositions of amphiboles in Mlakawa albitite ploted on an isopleth of Al_2O_3 and TiO_2 diagram of clacic amphibole (after Ernst and Liu, 1998). P-pressure; T-temperature.

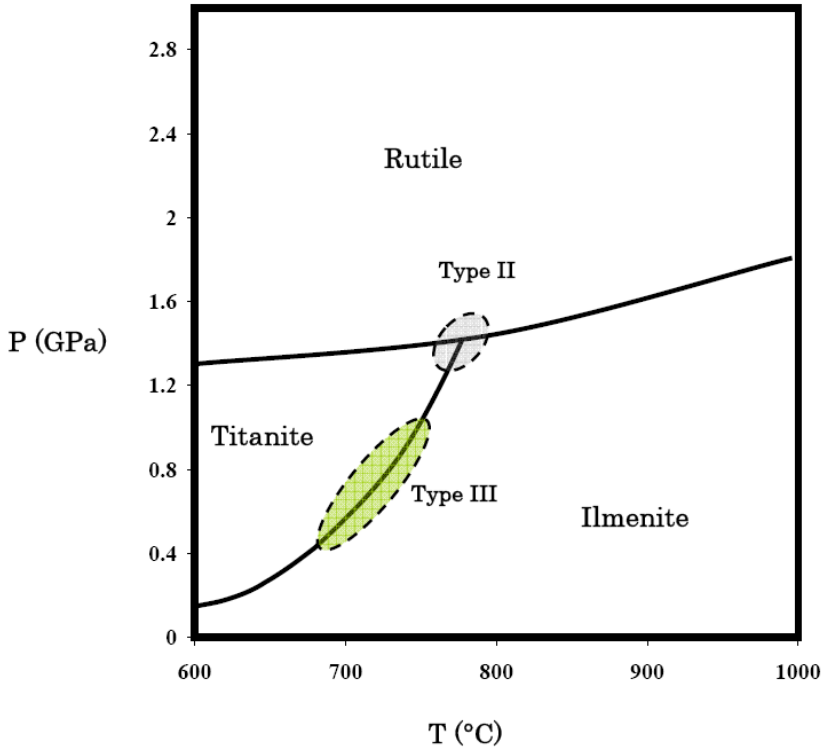

Fig. 6 – 13: Field of the approximate stability ranges of Type II and Type III metamorphic titanite in Mlakawa albitite. Stability fields of Ti-phases after Liu et al. (1996).

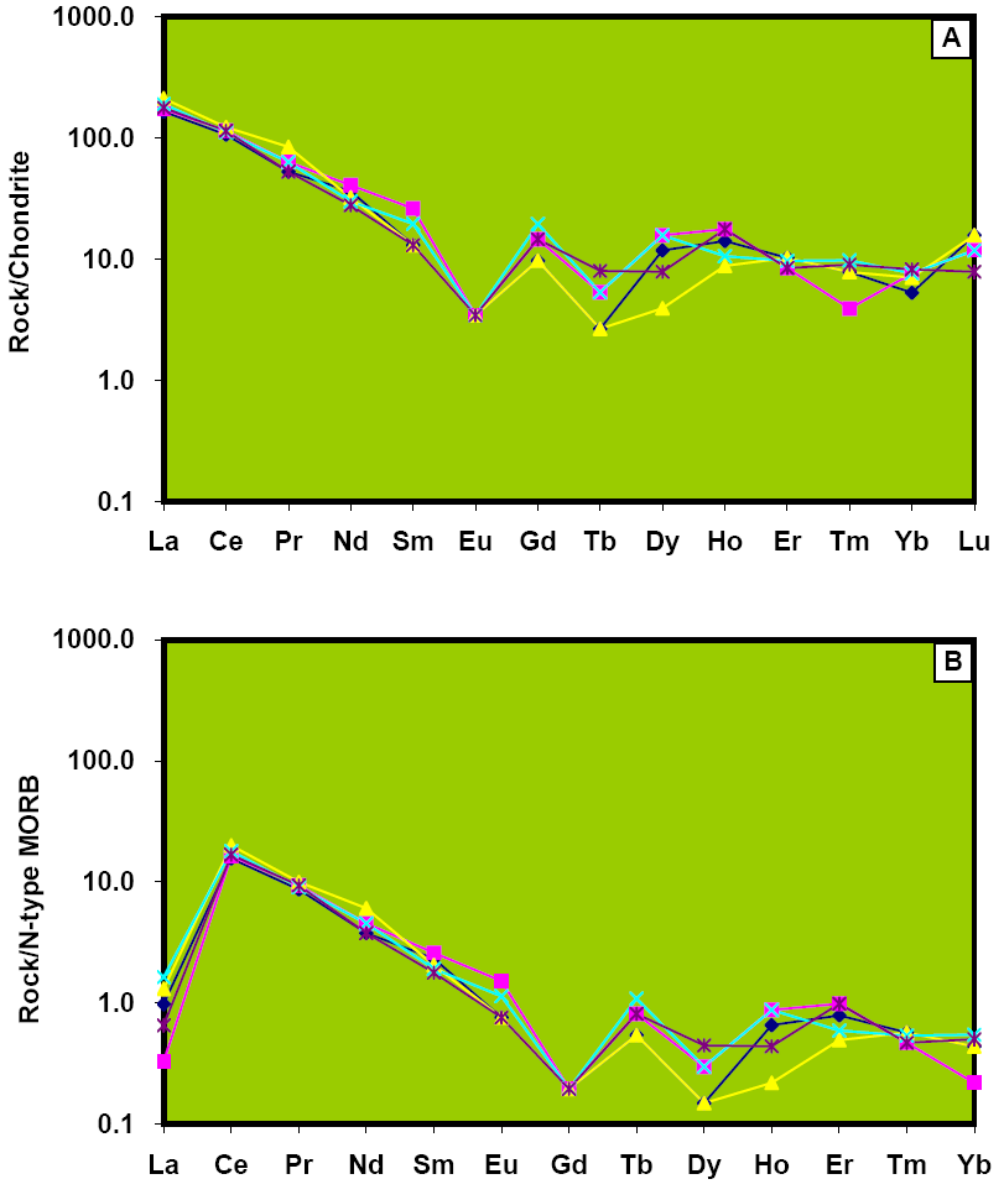

Fig. 6 – 14: (A) Chondrite-normalized rare earth element (REE) diagram for Mlakawa albitite. (B) Normal-type mid-ocean ridge basalt (N-MORB)-normalized REE diagram after Sun and Mc Donough (1989) for Mlakawa albitite.

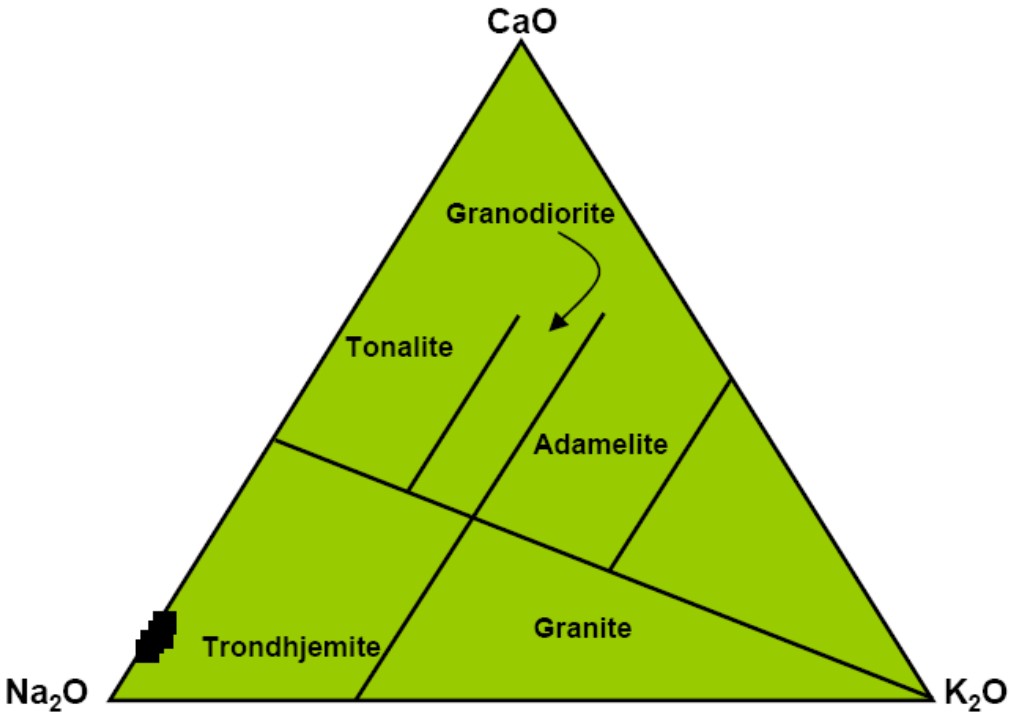

Fig. 6 – 15: Whole rock chemical compositions of Mlakawa albitite plotted on a CNK (CaO Na_2O K_2O) classification diagram (after Glikson, 1979).

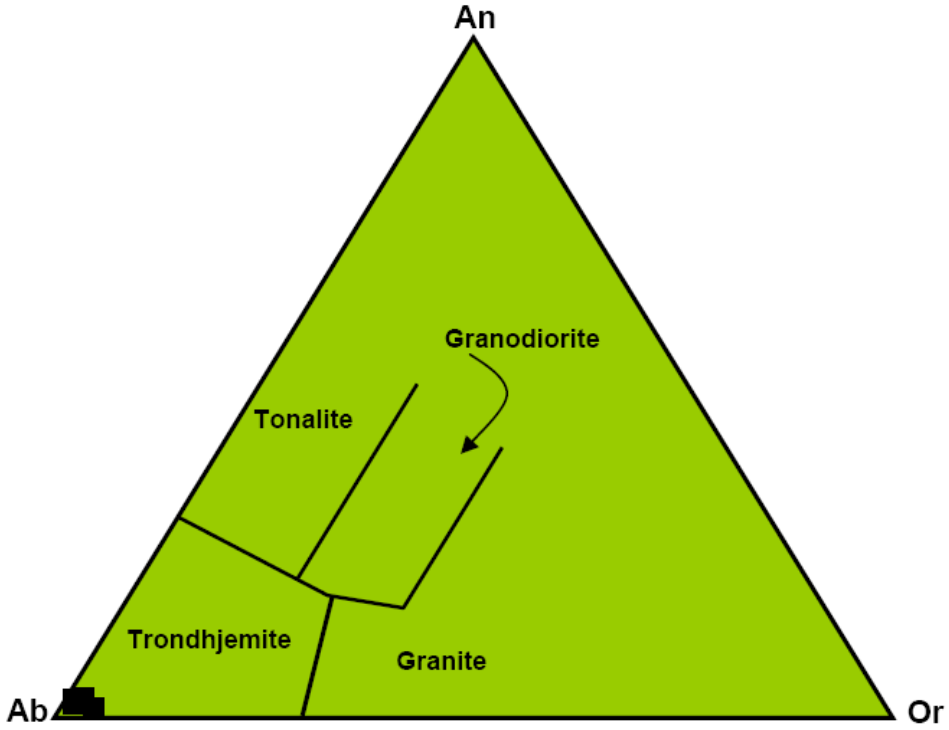

Fig. 6 – 16: Normative compositions of Mlakawa albitite plotted on Ab-An-Or (albite-anorthite-orthoclase) classification diagram (after Barker, 1979).

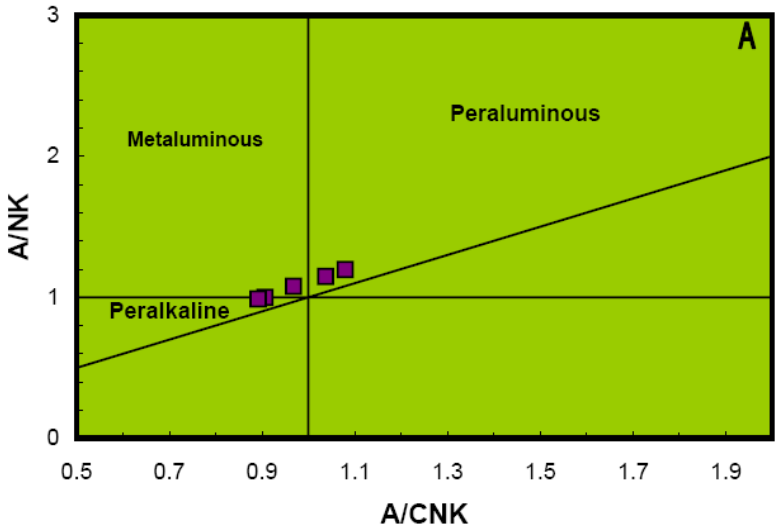

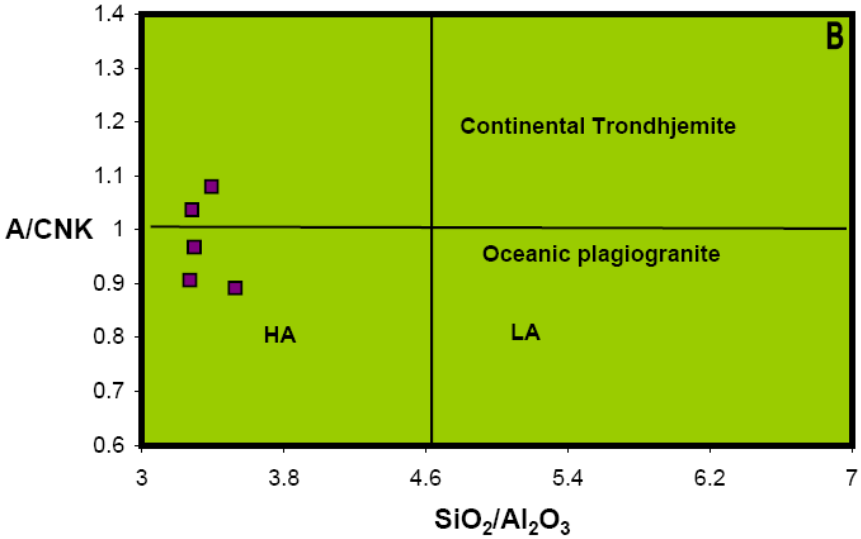

Fig. 6 – 17: Whole rock chemical compositions of Mlakawa albitite. A- Plotted on a molar A/CNK [Al_2O_3/ (CaO Na_2O K_2O)] vs. A/NK diagram (after Shand, 1943). B- Plotted on a molar A/CNK vs. SiO_2/Al_2O_3 diagram (after Sarvothaman, 1993).

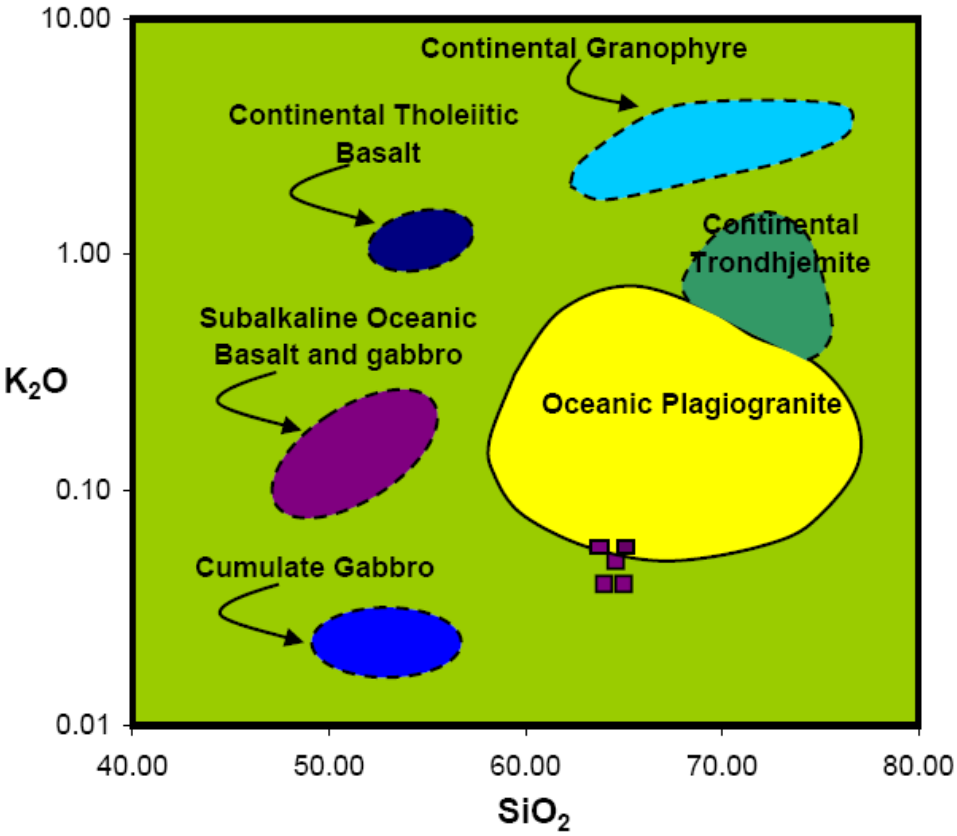

Fig. 6 – 18: Whole rock chemical compositions of Mlakawa albitite plotted on K_2O wt.% vs. SiO_2 wt.% binary diagram; field boundary after Coleman and Peterman (1975)

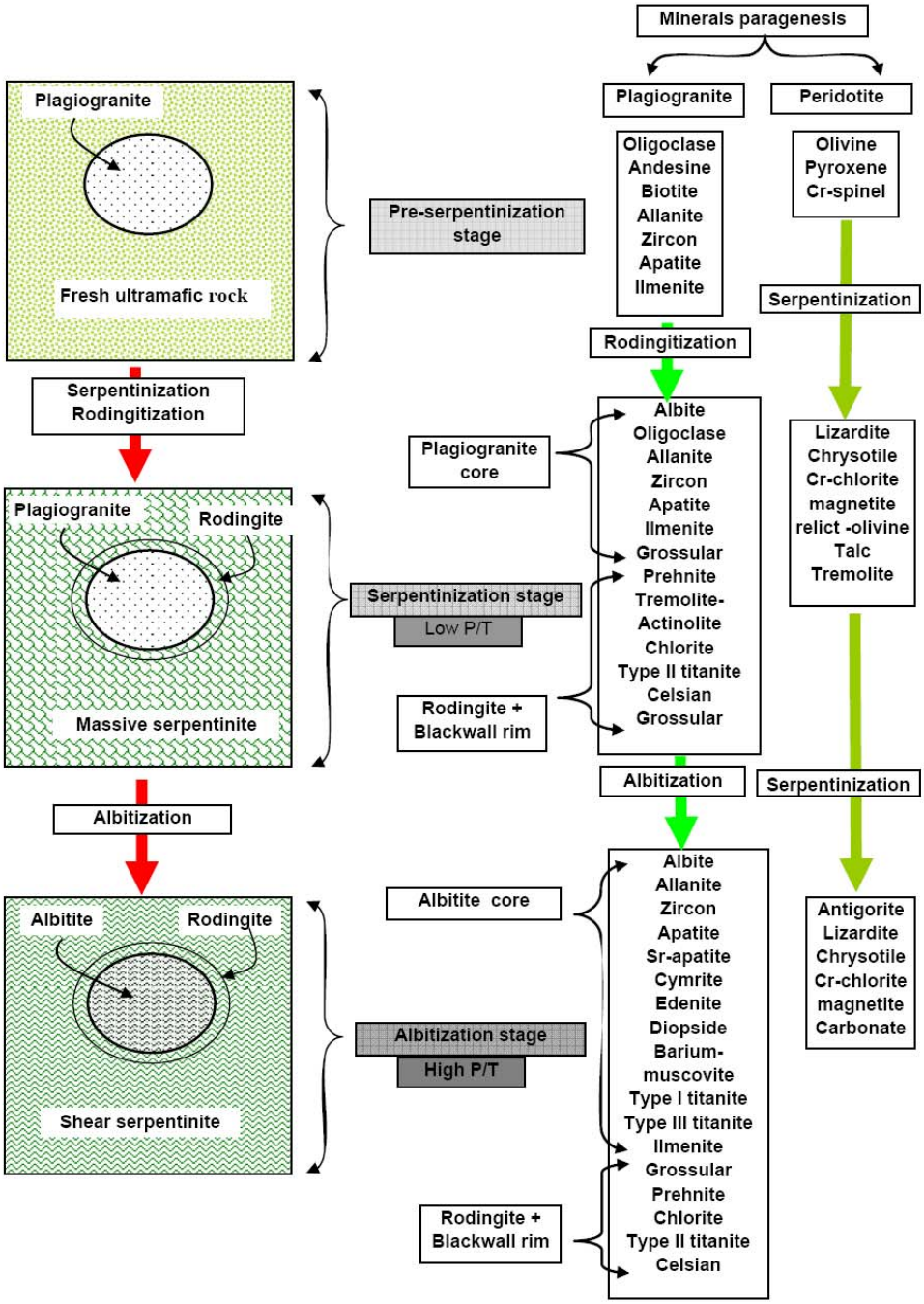

Fig. 6 – 19: Time-paragenesis, albitization, serpentinization, and rodingitization scenario diagram.P/T- pressure-temperature.

Chapter 7

Conclusions and Recommendations

1 Conclusions

1. The Iraqi Zagros Thrust Zone peridotites range from lherzolite to dunite through harzburgite, those of which have mineral compositions similar to those of forearc peridotites. The Iraqi Zagros Thrust Zone peridotites are represented by fertile alpine mantel lherzolite to dunite through depleted tectonite harzburgite rather than cumulate or replacive ones.

2. Abundance of TiO_2 and Al_2O_3 in magmatic spinels are mainly controlled by contents of these oxides in primary melts, and thus can be used to discriminate different magma types, and their tectonic affinities. Chromian spinel from the Iraqi Zagros Thrust Zone peridotite characterized by gradual increasing of TiO_2 and gradual decreasing of Al_2O_3 with increasing the degree of partial melting, suggesting that these ultramafic bodies are fragments of suprasubduction zone residual mantle peridotites.

3. Chromian spinels in the Iraqi Zagros Thrust Zone peridotites were variably altered, providing a good opportunity to evaluate their textural and compositional variation with metamorphism. Chrmoian spinels with normal zoning are typically zoned with unaltered cores to Cr-magnetite rims through ferrichromite transitional zone. Chrmoian spinels with reverse zoning typically have Al-rich rim and Cr-rich core. Retrogressive metamorphism was mainly responsible for the chemical modification in normal zoned chrmian spinel. In contrast the cyclic metamorphism mainly caused chemical modification, and formed reversely zoned chromian spinel

4. Related rocks with the Iraqi Zagros Thrust Zone peridotites are typically represented by both rodingite and albitite. Rodingites are associated with early serpentinization process of peridotite.

Albitites represent high pressure low temperature rock associated with late serpentinization process.

5. Serpentinization, rodingitization, and albitization processes observed in the Mlakawa albitite are complementary processes. Each process has a specific effect during a particular time in the evolution of the ultramafic-plagiogranite part of the Penjwin ophiolite sequence, leading to the formation of the Mlakawa albitite. Both serpentinization of peridotite and rodingitization of plagiogranite represent low-temperature and low-pressure conditions during the oceanic and the subduction stages before collision of the Arabian plate with the Iranian plate. In contrast, the albitization of plagiogranite represents high-pressure and high-temperature conditions at the collisional stage of the Arabian plate with the Iranian plate during the Late Cretaceous period.

2 Recommendations for further works

1. Future studies focusing on the chemical composition and mode of occurrence of hornblendite within Iraqi Zagros Thrust Zone ultramafic belt could help strengthen the correlation between the ultramafic bodies. As well as $^{40}Ar/^{39}Ar$ isotope study of hornblendite will gave the absolute age of ultramafic belt in Iraqi Zagros Thrust Zone, which is still debated due to the absence of critical geochrnological data.

2. SHRIMP-dating of zircon, titanite and allanite in related rocks associated with Iraqi Zagros Thrust Zone peridotites will also increase our knowledge about the absolute ages of these bodies and its relation to serpentinization episodes of peridotites.

3. LA-ICP-MS study of both black and green olivines in dunite will improve our knowledge about the origin of such olivines in terrestrial dunite.

4. Studying magnetite lamellae in black olivine will help us to understand whether they have been formed in grate depth in mantle or formed under the high oxidizing environments in the crust.

5. As the exsolution lamellae of spinel are common in both olivine and orthopyroxene of the harzburgite from the Pauza ultramafic bodies. Genesis and geothermobarometric study of this phenomenon will help to decide whether this phenomenon is due to UHP metamorphism or reflects normal melting process?

References

Adam, M. G., Stewart, K. G., Trupe, C.H., and Willard, R. A., 1995. Tectonic significance of high-pressure metamorphic rocks and dextral strike-slip faulting in the southern Appalachians, in Hibbard J., Van Staal, C. R., Cawood, P., and Colman, S., ed., Current Perspectives in the Appalachian-Caledonian Orogen. Geological Association of Canada Special papar, 41, 21 – 42.

Alavi, M., 2004. Regional stratigraphy of the Zagros Fold-Thrust Belt of the Iran and its proforeland evolution. American Journal of Science, 304, 1–20.

Aldiss, D.T., 1981. Plagiogranite from the oceanic crust and ophiolites. Nature, 289, 577–578.

Al-Hassan, M. I., 1982. Petrology, mineralogy and geochemistry of Penjwin Igneous complex, northeastern Iraq. [Ph.D. Thesis]. Uk, University of Dundee, 300 p.

Al-Mehidi, H. M., 1975. Tertiary nappe in Mawat range. Iraqi Journal of Geological Society, VIII, 31– 44.

Anderson, O., 1982. The genesis of some types of feldspar from granite pegmatite. Norsk Geologisk Tidsskrift, 10, 116–128.

Anhaeusser, C. R., 1979. Rodingite occurrence in some Archean ultramafic complexes in the Barberton Mountain Land, South Africa. Precambrian Research, 36, 649 – 676.

Aqrawi, A. M., 1990. Petrochemistry and petrogenesis of ultramafic and gabbroic around Route Mountain (Mawat ophiolite complex). [M.Sc Thesis], Iraq, University of Mosul, 140 p.

Arai, S., 1994. Characterization of spinel peridotites by olivine-spinel compositional relationships: Review and Interpretation. Chemical Geology, 113, 191–204.

Arai, S., 1987. An estimation of the least depleted spinel peridotite on the basis of olivine–spinel mantle array. Neues Jahrbuch für Mineralogie Monatshefte, 8, 347–354.

Barker, F., 1979. Trondhjemite: definition, environments and hypotheses of the origin, in Barker, F., eds., Trondhjemite, Dacite, and related rocks. Elsevier, Amsterdam, p 1–12.

Barnes, S. J., and Roeder, P. L., 2001. The range of spinel compositions in terrestrial mafic and ultramafic rocks. Journal of Petrology, 42, 2279–2302.

Barnes, S. J., 2000. Chromite in komatiites. II. Modification during greenschist to mid-amphibolite facies metamorphism. Journal of Petrology 41, 387 – 409.

Battey, M.H., 1995. Alkali metasomatism and petrology of some kyratophyres. Geological Magazine, 92, 104–126.

Best, M.G., 2003. Igneous and Metamorphic Petrology. Blackwell Science Ltd., 717 p.

Bolton, C. M., 1957. Explanation of the geological map- Kurdistan series. Scale 1: 100000, sheet KS Choarta. Unpublished report, State Establishment of Geological Survey and Mineral Investigation, Baghdead, Iraq.

Bonatti, E., and Michael, P.J., 1989. Mantle peridotites from continental rifts to ocean basins to subduction zones. Earth and Planetary Science Letters, 91, 297–311.

Borsi, L., Scharer, U., Gaggero, L., and Crispini, L., 1996. Age, origin and geodynamic significance of plagiogranite in lherzolite and gabbros of the Piedmont-Ligurian ocean basin. Earth and Planetary Science Letters, 140, 227–241.

Boulvais, P., Ruffet, G., Cornichet, J., and Mermet, M., 2007. Cretaceous albitization and dequartzification of Hercynian peraluminous granite in the Salvezines Massif (French Pyrénées). Lithos, 93, 89–106.

Brewer, R. C., and Woodward, N. B., 1988. The Amphibole Basment Complex in the Blue Ridge Province of western North Carolina: Proto-Iapetus?. American Journal of Science, 288, 95 – 976.

Buday, T. and Jassim, S.Z., 1987. The regional geology of Iraq, Volume 2, Tectonism, magmatism and metamorphism. Baghdad, Iraq, State Establishment of Geological Survey and Mineral Investigation, 445 p.

Buday, T., 1973. The Regional Geology of Iraq. Unpublished report, State Establishment of Geological Survey and Mineral Investigation, Baghdead, Iraq. 525 p.

Buming, S., Zhou, Y., Deng, W., Han, X., and Zhang, R., 1997. The Texture, Mineral Assemblages and Origin of Metamorphic Peridotite from Kuda Ophiolite. Chines Journal of Geochemistry, 16, 336–345.

Cabanes, N., and Mercier, J.C.C., 1988. Insight into the upper mantle beneath an active extensional zone: the spinel–peridotite xenoliths from San Quentin (Baja California, Mexico). Contributions to Mineralogy and Petrology, 100, 374–382.

Carpedri, S., Garuti, G. and Rossi, S., 1978. Rodingite from Pindos. Constrain on the "rodingite problem". Neues Jahrbuch Für Mineralogie Abhandlungen, 132, 242-263.

Castorina, F., Masi, U., Padalino, G., and Palomba, M., 2006. Constrains from geochemistry and Sr-Nd isotopes for the origin of albitite deposits from Centeral Sardinia (Italy). Mineralium Deposita, 41, 323–338.

Cathelineau, M., 1988. Accessory mineral alteration in peraluminous granites at the hydrothermal stage: a review. Rendiconti della Societá Italiana di Mineralogia Petrologia, v. 43, p. 499 – 508.

Chakhmouradian, A.R., Reguir, E.P., and Mitchell, R.H., 2002. Strontium-apatite: New occurrences and the extent of Sr-for-Ca substitution in apatite group minerals. Canadian Mineralogist, 40, 121–136.

Chhibber, H. L., 1934. The mineral resources of Burma. Macmillan, London.

Coshi, R.A., Gardner, P., 2004. Suprasubduction-zone peridotite in the northern USA Appalachians: evidence from mineral composition. Mineralogical Magazine 68, 699 – 708.

Coleman, R.G., 1980. Tectonic inclusion in serpentinite: Archives des sciences (Societe de Physique et d'Histoire Naturelle de Genéve). 33, 89–102.

Coleman, R. G., 1977. Ophiolites, Ancient Oceanic lithosphere? Springer Verlage, New York.

Coleman, R. G., 1961. Jadeite deposits of the Clear Creek area, New Idria district, San Benito County, California. Journal of Petrology, 2, 209 – 247.

Coleman, R.G. and Peterman, Z.E., 1975. Oceanic plagiogranite. Journal of Geophysical Researches, 80, 1099–1108.

Coleman, R.G. and Donato, M.M., 1979. Oceanic plagiogranite revisted, in Barker. F., eds., Trondhjemites, Dacites, and related rocks. Elsevier, Amsterdam, p. 149–168.

Dewey, J. F., and Bird, J. M., 1970. Mountain belt and the new global tectonics. Journal of Geophysical Research, 75, 2625 – 2647.

Dick, H.J.B., Bullen, T., 1984. Chromium spinel as a petrogenetic indicator in abyssal and alpine-type peridotites and spatially associated lavas. Contributions to Mineralogy and Petrology 86, 54–76.

Ditez, R. S., 1963. Alpine serpentinite as oceanic rind fragments. Geological Society of America Bulletin, 74, 947–952.

Dobretsov, N. L., Ponomareva, L. G., 1965. Comparative characteristics of jadeite and associated rocks from Polar Urals and Near-Balkhash region. Academia Scientifica USSR (Siberian Branch), Trudy, Institute

of Geology and Geophysics, 31, 178–243. (Translation: International Geology Review, 10, 221 – 279).

Dobrzhinetskaya, L., Green, H.W. and Wang, S., 1996. Alpe Arami: a peridotite massif from depths of more than 300 Kilometers. Science, 271, 1841 – 1845.

Downes, H., 2001. Formation and Modification of the Shallow Sub-contenental lithospheric Mantle: a Review of Geochemical Evidence from Ultramafic Xenolith Suites and Tectonically Emplaced Ultramafic Massifs of Western and Central Europe Journal of Petrology, 42, 233–250.

Dubińska, E., Bylina, P., Kozłowski, A., Dörr, W., Nejbert, K., Schhastok, J., and Kuliki, C., 2004. U-Pb dating of serpentinization: hydothermal zircon from a metasomatic rodingite shell (Sudetic ophiolite, SW Poland). Chemical Geology, 203, 183–203.

Duncan, R. A., and Green D. H., 1980. The genesis of refractory melts in the formation of oceanic crust. Contributions to Mineralogy and Petrology, 96, 326–342.

Eggleton, R.A. and Banfield, J. F., 1985. The alteration of granitic biotite to chlorite. American Mineralogist, 70, 902–910.

Enami, M., Suzuki, K., Liou, J.G. and Bird, D.K., 1993. Al-Fe+3 and F-OH substitution in titanite and constraints on their P-T dependence. European Journal of Mineralogy, 5, 219–231.

Engel, C.G. and Fisher, R.L., 1975. Granitic to ultramafic rocks complexes of the Indian oceanic ridge system, western Indian Ocean. Geological Society of America Bulletin, 86, 1553–1578.

Ernst, W.G. and Liu, J., 1998. Experimental phase-equilibrium study of Al and Ti content of calcic amphibole in MORB: A semiquantitative thermobarometer. American Mineralogist, 83, 952–969.

Evans, B.W., Trommsdorf, V., and Richter, W., 1979. Petrology of an eclogite–metarodingite suite at Cima di Gagnone, Ticino, Switzerland. American Mineralogist, 64, 15 – 31.

Evans, B.W., Frost, B.R., 1975. Chrome spinel in progressive metamorphism — a preliminary analysis. Geochimica et Cosmochimica Acta, 39, 959–972.

Forst, B. R., 1975. Contact metamorphism of serpentinite, chlorite blackwall and rodingite at Paddy-Go-Eassy Pass, Central Cascades, Wahington. Journal of Petrology, 16, 272 – 313.

Frondel, C. and Ito, J., 1968. Barium rich phologopite from Långban, Sweden. Arkiv for Mineralogi och Geologi, 4, 445–447.

Gaetani, G., A., and Timothy L., 1998. The influence of water on melting of mantle peridotite. Contributions to Mineralogy and Petrology, 131, 323–346.

Gilluly, J., 1933. Replacement origin of albite granite near Sparta. Oregon: USA Geological Survey Prof Pap, 175C, 65–81.

Gieré, R., and Sorenson, S. S., 2004. Allanite and other REE-rich epidote group minerals. Review in Mineralogy and Geochemistry, 156, 413–493.

Glikson, A.Y., 1979. Early Precambrian tonalite-trondijimite sailic nuclei. Earth Science Reviews, 15, 1–73.

Harcker, B.R., Sharp, T., Zhang, R.Y. and Liou, J.G., 1997. Determing the origin of ultrahigh-pressure lherzolites. Science, 278, 702 – 704.

Harlov, D., Tropper, P., Seifert, W., Nijland, T., and Förster, H., 2006. Formation of Al-rich titanite ($CaTiOSiO_4O$-$CaAlSiO_4OH$) reaction rim on ilmenite in metamorphic rocks as function of fH_2O and fO_2. Lithos, 88, 72–84.

Harlow, G.E., 1994. Jadeitites, albitite and related rocks from the Motagua fault zone, Guatemala. Journal of Metamorphic Geology, 12, 49–68.

Harlow, G.E., 1995. Crystal chemistry of barian enrichment in micas from metasomtized inclusion in serpentinite, Motagua fault zone, Guatemala. European Journal of Mineralogy, 7, 775–789.

Harlow, G.E. and Olds, E.J., 1987. Observation on terrestrial ureyite and ureyitic pyroxene. American Mineralogist, 72, 126–136.

Harte, B., 1977. Rock nomenclature with particular relation to deformation and crystallization textures in olivine bearing xenoliths. Journal of Geology, 85, 279 – 288.

Hatzipanagiotou, K. and Tsikouras, B., 2001. Rodingite formation from diorite in the samothraki ophiolite, NE Aegean, Greece. Geological Journal, 36, 93 –109.

Hellebrand, E., Snow, J.E., Dick, H.J.B., Hofmann, A.W., 2001. Coupled major and trace elements as indicators of the extent of melting in mid-ocean-ridge peridotites. Nature, 410, 677–681.

Hey, M. H., 1954, A new review on the chlorites. Mineralogical Magazine, 224, 277–298.

Holland, T.J.B. and Blundy, J., 1994. Non-ideal interactions in calcic amphiboles and their bearing on the amphibole plagioclase thermometry. Contribution to Mineralogy and Petrology, 116, 433–447.

Honnorez, J. and Kirst, P., 1975. Petrology of rodingite from equatorial Mid-Atlantic fracture zones and their geotectonic sificance. Contribution to Mineralogy and Petrolology, 49, 233 – 257.

Irvine, T.N., 1965. Chrome spinel as a petrogenetic indicator. Part I—Theory. Canadian Journal of Earth Sciences, 2, 648–674.

Irvine, T.N., 1967. Chromian spinel as a petrogenetic indicator. Part II—Petrogenetic applications. Canadian Journal of Earth Sciences, 4, 71–103.

Jameieson, R. A., 1981. Metasomatism during Ophiolite Emplacement-The Petrology of the St. Anthony Complex, Journal of Petrology, 22, 397–449.

Jaques, A. l., and Green, D. H., 1980. Anhydrous melting of peridotite at 10 15 kb pressure and genesis of tholeiitic basalts. Contributions to Mineralogy and Petrology, 73, 287–310.

Johnson, C.A. and Harlow, G.E., 1999. Guatemala jadeitites and albitites were formed by deuterium-rich serpentinizing fluids deep within a subduction zone. Geology, 27, 629 – 632.

Kamenetsky, V., Crawford, A. J., and Meffre, S., 2001. Factors controlling chemistry of magmatic spinel: an empirical study of associated olivine, Cr-spinel and melt inclusions from primitive rocks. Journal of Petrology, 42, 655–671.

Kaur, G. and Mehta, P.K., 2005. The Gothera plagiogranite: evidence for oceanic magmatism in a non-ophiolitic association, North Khetri Copper Belt, Rajasthan, India. Journal of Asian Earth Science, 25, 805–819.

Kobayashi, S., Miyake, H., and Shoji, T., 1987. A jadeitite rock from Oosa-cho, Okyama Prefecture, south western Japan. Mineralogical Journal, 13, 311–327.

Kontinen, A., 1987. An early Proterozoic ophiolite-the Jormua mafic-ultramafic complex, northeastren Finland. Precambrian Research, 35, 313–341.

Kostopoulos, D.K., 1991. Melting of shallow upper mantle: a new perspective. Journal of Petrology, 32, 671–699.

Kovalenko, V.I., 1978. The genesis of rare metal granitoids and related ore deposit, in Stempork, M., Burnol, L., and Tischendorf, G., eds., Metallization associated with acid magmatism. Cezech Geological Survey, 3, 235 – 247.

Kowallis, B.J., Christiansen, E.H. and Griffen, D.T., 1997. Compositional variations in titanite. Geological Society of America Abstracts with Programs, 29, 44.

Krenn, E. and Finger, F., 2004. Metamorphic formation of Sr-apatite and Sr-bearing monzonite in high pressure rock from the Bohemian Massif. American Mineralogist, 89, 1323–1329.

Kretz, R., 1983. Symbols of rock-forming minerals. American Mineralogist, 68, 277–279.

Kubo, K., 2002. Dunite Formation Process in Highly Depleted Peridotite: Case Study of the Iwandake Peridotite, Hokkiado, Japan. Journal of Petrology, 43, 423–448.

Leach, T.M., and Rodgers, K.A., 1978. Metasomatism in the Wairere serpentinite, King Country, New Zealand. Mineralogical. Magazine . 42, 45– 62.

Leake, B.E., and 21 others, 1997. Nomenclature of amphiboles: Report of the subcommittee on amphiboles of the International Mineralogical Association, Commission on New Minerals and Mineral Names. Canadian Mineralogist, 35, 219–246.

Mahmmod, L.A., 1978. Petrology and geochemistry of ultramafics around Penjwin, northeast Iraq with special reference to the genesis of the chromites associated with them [M.Sc Thesis]. Iraq, University of Mousl, 220 p.

Mercier, J.C.C., and Nicolas, A., 1975. Textures and fabrics of the upper mantle peridotites as illustrated by basalt xenoliths. Journal of Petrology, 16, 454 –487.

Mohammad, Y. O., Maekawa, H., and Lawa, F. A., 2007. Mineralogy and origin of Mlakawa albitite from Kurdistan region, northeastern Iraq. Geosphere, 3, 624–645.

Mohammad, Y. O., and H. Maekawa, 2007. Serpentinite and serpentinization events along the Iraqi Zagros Thrust Zone. Proceedings of the second international conference on the geology of Teythes, 85–100.

Mohammad, Y.O., 2004, Petrology and geochemistry of serpentinite and associated rocks in Penjwin and Mawat area, Kurdistan Region, NE Iraq [M.Sc Thesis]. Iraq, Sulaimani University, 210 p.

Moore, D.E. and Liou, J.G., 1979. Chessboard-twinned albite from Franciscan metaconglomerates of the Diblo Range, California. American Mineralogist, 64, 329–336.

Moores, E. M., 1976. Ultramafics and Orogeny, with models of the US Cordillera and the Tethys. Nature, 288, 837 – 842.

Moores, E. M., 1981. Ancient suture zones within continents. Science, 213, 41 – 46.

Morand, V.J., 1990. High chromium and vanadium in andalusite, phengite and retrogressive margerite in contact metamorphosed Ba-rich black slate from the Abercrombie Bed, New South Wales, Australia. Mineralogical Magazine, N54, 381–391

Morimoto, N., Fabries, J., Forguson, A. K., Ginzburg, I. V., Ross, M., Seifert, F. A., Zussman, J., Aoki, K., and Gottradi, G., 1988. Nomenclature of pyroxenes. American Mineralogist, 73, 1123 – 1133.

Morkovkina, V. F., 1960. Jadeitites in the hyperbasities of the Polar Orals. Izvestia Akademian Nauk SSSR, series geologia, 4.

Nesse, W., D., 1999. Introduction to Optical Mineralogy. New York: Oxford University Press.

Numan, N.M., 2001. Dextral transpression in Late Cretaceous continental collision, Sanadaj-Sirjan, western Iran: Discussion. Journal of Structural Geology, 23, 2033–2034.

O'Brien, J.P. and Rötzler, J., 2003. High pressure granulites: Formation, recovery of peak conditions, and implication for tectonics. Journal of Metamorphic Geology, 21, 3–20.

O'Hanley, D.S., Schandl, E.S., and Wicks, F.J., 1992. The origin of rodingites from Cassiar British Columbia, and their use to estimate T and P(H_2O) during serpentinization. Geochimica Cosmochimica and. Acta, 56, 97 – 108.

O'Hanley, D.S., 1996. Serpentinites. Records of Tectonic and Petrological History. Oxford Monographs on Geology and Geophysics, vol. 34. Oxford Univ. Press, New York, pp. 1 – 277.

Osada, Y., Maekawa, H., and Yamamoto, K., 2007. Jadeite-qyartz-K-feldspar rocks in the Kamuikotan zone, Japan. Journal of Mineralogical and Petrological Science, 102, 50 – 56.

Pearce, J.A., Barker, P.F., Edwards, S.J., Parkinson, I.J., and Leat, P.T., 2000. Geochemistry and tectonic significance of peridotites from the

South Sandwich arc-basin system, South Atlantic. Contributions to Mineralogy and Petrology, 139, 36–53.

Rao, D.R., Rai, H., and Kumar, J.S., 2004.Origin of oceanic plagiogranite in Nidar ophiolite sequence of eastern Ladakh, India.Current Science, 87, 999–1005.

Raymond, A., L., 2002. Petrology, the study of igneous sedimentary and metamorphic rocks. McGraw-Hill Higher Education Co. New York, USA. 2002.

Raymond, L. A., Love, A., and McCarter, R., 2001. Petrology of the Hoots ultramafic body, Blue Ridge belt, northwestern north Carolina. Southeastern Geology, 40, 149 –162.

Sarvothaman, H., 1993. The molar Al_2O_3/ ($CaO+Na_2O+K_2O$) ratios as discriminate for oceanic plagiogranites and continental trondhjemites. Journal of the Geological Society of India, 42, 513–522.

Saunders, A.D., Tarney, J., Stern, C.R., and Dalziel, I.W., 1979. Geochemistry of Mesozoic marginal basin floor igneous rocks from southern Chile. Geological Society of America Bulletin, 90, 237–258.

Schandl, E. S., O Hanley, D. S., Wickes, F., and Kyser, T. K., 1989. Rodingite in serpentinized ultramafic rocks of Abitibi Greenstone belt, Ontarion. Canadian Mineralogist, 27, 579 – 591.

Schwartz, M.O., 1992. Geochemical criteria for distinguishing magmatic and metasomaic albite-enrichment in granitoids: examples from Ta-Li granite Yivhun (China) and the Sn-W deposit Tikus (Indonesia).Mineralium Deposita, 27, 101–108.

Shand, S.J., 1943. Eruptive rocks: Their genesis, composition, classification and relation to ore deposits. New York, J. Wiley and Sons, 488 p.

Smith, D.C., 1988. Coesite in clinopyroxene in the Caledonides and its implications for geodynamics. Nature, 310, 641–644.

Smith, J.V., 1974. Feldspar minerals: Volume 2, Chemical and textural properties. New York. Springer-Verlage, 690 p.

Watson, E.B., Wark, D. A. and Thomas, J. B., 2005. Crystallization thermometer for zircon and rutile. Contribution to Mineralogy and Petrology, 151, 413–433.

Winter, J., 2001. An Introduction to Igneous and Metamorphic Petrology. Prentice Hall, New Jersey.

Wyllie, P., J., 1967. Ultramafic and Related Rocks. John Wiley and Sons Inc., New York USA.

Zhang, R.Y., and Liou, J.G., 1998. Ultrahigh-pressure metamorphism of the Sulu terrane, eastern China. a prospective view, Continental Dynamics, 3, 332 – 53.

Zhang, R.Y., and Liou, J.G., 2003. Clinopyroxene from sulu ultrahigh pressure terrain, eastern china, origin and evolution of garnet exsolution in clionpyroxene. American Mineralogist, 88, 1591 – 1600.

Zhang, R. Y., Shu, J. F., Mao, H. K., and Liou, J. G., 1999. Magnetite lamellae in olivine and clinohumite from Dabi UHP ultramafic rocks centeral China. American Mineralogist, 84, 564 – 569.

Appendices

Table 4 - 1: Representative micronalyses of olivine from Penjwin peridotites

	Harzburgite							*Dunite*					
Oxides (wt.%)													
SiO_2	39.97	39.98	39.97	40.23	40.30	40.39	39.98	41.45	40.24	40.26	40.51	40.67	41.45
TiO_2	0.00	0.00	0.00	0.00	0.00	0.00	0.00	0.79	0.00	0.00	0.00	0.00	0.79
Al_2O_3	0.02	0.12	0.16	0.15	0.23	0.24	0.00	0.97	0.13	0.14	0.18	0.32	0.97
Fe_2O_3	0.00	0.00	0.00	0.00	0.00	0.00	0.00	0.00	0.00	0.00	0.00	0.00	0.00
FeO	8.23	8.28	8.39	8.51	8.33	8.40	8.35	7.54	8.67	8.60	8.67	8.53	7.54
MnO	0.34	0.31	0.17	0.22	0.27	0.22	0.32	0.19	0.27	0.25	0.23	0.20	0.19
MgO	50.14	50.16	50.19	50.22	50.07	50.09	50.14	48.34	50.14	50.07	50.11	50.18	48.34
Cr_2O_3	0.00	0.00	0.00	0.00	0.00	0.00	0.10	0.00	0.12	0.11	0.11	0.11	0.00
V_2O_5	0.00	0.00	0.00	0.00	0.00	0.00	0.20	0.00	0.11	0.12	0.04	0.05	0.00
NiO	0.85	0.71	0.78	0.74	0.70	0.67	0.89	0.00	0.83	0.77	0.75	0.75	0.00
Total	99.55	99.56	99.66	100.07	99.9	100.02	99.78	99.28	100.4	100.2	100.56	100.76	99.28
Cation proportions per 4 oxygen atoms													
Si	0.98	0.98	0.98	0.98	0.99	0.99	0.98	1.01	0.98	0.98	0.99	0.99	1.01
Ti	0.00	0.00	0.00	0.00	0.00	0.00	0.00	0.01	0.00	0.00	0.00	0.00	0.01
Al	0.00	0.00	0.00	0.00	0.01	0.01	0.00	0.03	0.00	0.00	0.01	0.01	0.03
Fe^{3+}	0.00	0.00	0.00	0.00	0.00	0.00	0.00	0.00	0.00	0.00	0.00	0.00	0.00
Fe^{2+}	0.17	0.17	0.17	0.17	0.17	0.17	0.17	0.15	0.18	0.18	0.18	0.17	0.15
Mn	0.01	0.01	0.00	0.00	0.01	0.00	0.01	0.00	0.01	0.01	0.00	0.00	0.00
Mg	1.84	1.84	1.84	1.83	1.83	1.83	1.83	1.75	1.82	1.82	1.82	1.82	1.75
Cr	0.00	0.00	0.00	0.00	0.00	0.00	0.00	0.00	0.00	0.00	0.00	0.00	0.00
V	0.00	0.00	0.00	0.00	0.00	0.00	0.00	0.00	0.00	0.00	0.00	0.00	0.00
Ni	0.02	0.01	0.02	0.01	0.01	0.01	0.02	0.00	0.02	0.02	0.01	0.01	0.00
Fo	91.57	91.52	91.43	91.32	91.46	91.40	91.46	91.95	91.16	91.21	91.15	91.29	91.95

Table 4 - 2: Representative micronalyses of spinel from Penjwin peridotites

	Harzburgite						*Dunite*						
Oxides (wt.%)													
SiO_2	0.97	0.92	0.94	0.97	1.02	1.01	1.23	0.65	0.72	0.73	0.69	0.68	0.69
TiO_2	0.15	0.21	0.29	0.26	0.33	0.31	0.00	0.00	0.00	0.00	0.00	0.00	0.00
Al_2O_3	22.96	23.06	23.00	23.10	23.22	23.26	11.38	11.09	11.10	11.29	11.21	11.15	11.21
Fe_2O_3	2.04	1.69	1.62	1.63	1.07	0.90	0.47	2.23	1.86	1.28	1.18	1.41	1.18
FeO	24.41	24.50	24.80	25.07	25.53	25.52	27.86	26.71	27.42	27.73	27.59	27.24	27.59
MnO	0.97	1.03	0.94	0.87	0.73	0.72	0.42	0.00	0.00	0.00	0.00	0.00	0.00
MgO	7.37	7.36	7.30	7.40	7.43	7.44	4.92	5.32	5.18	5.17	5.09	5.09	5.09
Cr_2O_3	40.65	40.99	40.87	41.02	41.12	41.16	53.07	53.52	53.70	53.64	53.53	53.14	53.53
V_2O_5	0.00	0.00	0.00	0.03	0.14	0.23	0.33	0.19	0.32	0.49	0.46	0.39	0.46
NiO	0.39	0.28	0.25	0.14	0.20	0.30	0.00	0.00	0.00	0.05	0.00	0.00	0.00
Total	99.91	100.07	100.02	100.48	100.79	100.90	99.77	99.71	100.30	100.38	99.75	99.10	99.75
Cation proportions per 6 oxygen atoms													
Si	0.03	0.03	0.03	0.03	0.03	0.03	0.04	0.02	0.02	0.02	0.02	0.02	0.02
Ti	0.00	0.01	0.01	0.01	0.01	0.01	0.00	0.00	0.00	0.00	0.00	0.00	0.00
Al	0.86	0.86	0.86	0.86	0.86	0.86	0.46	0.45	0.44	0.45	0.45	0.45	0.45
Fe^{3+}	0.05	0.04	0.04	0.04	0.03	0.02	0.01	0.06	0.05	0.03	0.03	0.04	0.03
Fe^{2+}	0.65	0.65	0.66	0.66	0.67	0.67	0.79	0.76	0.78	0.78	0.79	0.78	0.79
Mn	0.03	0.03	0.03	0.02	0.02	0.02	0.01	0.00	0.00	0.00	0.00	0.00	0.00
Mg	0.35	0.35	0.35	0.35	0.35	0.35	0.25	0.27	0.26	0.26	0.26	0.26	0.26
Cr	1.02	1.03	1.03	1.03	1.02	1.02	1.43	1.44	1.44	1.43	1.44	1.44	1.44
V	0.00	0.00	0.00	0.00	0.00	0.00	0.01	0.00	0.01	0.01	0.01	0.01	0.01
Ni	0.01	0.01	0.01	0.00	0.01	0.01	0.00	0.00	0.00	0.00	0.00	0.00	0.00
Cr#	54.29	54.39	54.38	54.36	54.29	54.28	75.78	76.40	76.44	76.12	76.21	76.17	76.21

Cr# = Cr *100 / (Cr + Al)

Table 4 - 3: Representative micronalyses of pyroxene in harzburgite from Penjwin peridotites

	Enstatite						*Diopside*						
Oxides (wt.%)													
SiO_2	57.15	57.05	57.04	57.09	56.96	56.25	53.93	53.72	54.00	53.99	53.99	54.04	54.46
TiO_2	0.00	0.00	0.00	0.00	0.00	0.32	0.00	0.00	0.00	0.00	0.00	0.00	0.00
Al_2O_3	0.48	0.32	0.33	0.36	0.36	0.00	0.07	0.08	0.11	0.11	0.11	0.09	0.17
Fe_2O_3	0.00	0.00	0.00	0.00	0.00	0.00	0.00	0.00	0.00	0.00	0.00	0.00	0.00
FeO	6.22	6.29	6.30	6.28	6.21	5.39	1.85	1.96	1.86	2.00	2.00	2.03	2.53
MnO	0.00	0.00	0.05	0.03	0.01	0.00	0.23	0.27	0.30	0.31	0.31	0.32	0.40
MgO	34.39	34.32	34.29	34.29	34.23	33.71	17.27	17.36	17.40	17.41	17.41	17.40	17.79
CaO	0.93	0.94	0.92	0.98	0.95	1.26	24.64	24.36	24.22	24.31	24.31	24.23	24.83
Cr_2O_3	0.56	0.51	0.59	0.57	0.56	0.78	1.01	1.16	1.16	1.03	1.03	1.00	1.09
V_2O_5	0.13	0.19	0.23	0.29	0.26	0.20	0.00	0.00	0.00	0.18	0.18	0.18	0.03
NiO	0.22	0.16	0.30	0.29	0.25	1.46	0.31	0.18	0.13	0.03	0.03	0.11	0.00
Total	99.95	99.59	99.82	99.89	99.53	99.17	99.31	99.09	99.18	99.19	99.19	99.22	101.27
Cation proportions per 4 oxygen atoms													
Si	1.97	1.98	1.97	1.97	1.97	1.97	1.98	1.98	1.98	1.98	1.98	1.98	1.97
Ti	0.00	0.00	0.00	0.00	0.00	0.01	0.00	0.00	0.00	0.00	0.00	0.00	0.00
Al	0.02	0.01	0.01	0.01	0.01	0.00	0.00	0.00	0.00	0.00	0.00	0.00	0.01
Fe^{3+}	0.00	0.00	0.00	0.00	0.00	0.00	0.00	0.00	0.00	0.00	0.00	0.00	0.00
Fe^{2+}	0.18	0.18	0.18	0.18	0.18	0.16	0.06	0.06	0.06	0.06	0.06	0.06	0.08
Mn	0.00	0.00	0.00	0.00	0.00	0.00	0.01	0.01	0.01	0.01	0.01	0.01	0.01
Mg	1.77	1.77	1.77	1.77	1.77	1.76	0.95	0.95	0.95	0.95	0.95	0.95	0.96
Ca	0.03	0.03	0.03	0.04	0.04	0.05	0.97	0.96	0.95	0.95	0.95	0.95	0.96
Cr	0.02	0.01	0.02	0.02	0.02	0.02	0.03	0.03	0.03	0.03	0.03	0.03	0.03
V	0.00	0.00	0.01	0.01	0.01	0.00	0.00	0.00	0.00	0.00	0.00	0.00	0.00
Ni	0.01	0.00	0.01	0.01	0.01	0.04	0.01	0.01	0.00	0.00	0.00	0.00	0.00

Table 4 - 4: Representative micronalyses of serpentine from Penjwin peridotites

	Antigorite							*Lizardite/chrysotile*					
Oxides (wt.%)													
SiO_2	38.39	40.68	38.62	40.60	39.47	37.75	37.97	47.10	45.87	47.98	47.96	51.34	42.76
TiO_2	0.00	0.00	0.00	0.04	0.04	0.13	0.08	0.00	0.17	0.05	0.00	0.00	0.09
Al_2O_3	0.04	0.00	0.00	0.01	1.46	0.00	0.00	0.07	0.00	0.00	0.00	0.00	0.10
Fe_2O_3	0.00	0.00	0.00	0.00	0.00	0.00	0.00	0.00	0.00	0.00	0.00	0.00	0.00
FeO	7.59	5.50	7.67	4.39	4.91	7.50	7.79	1.66	1.30	1.70	1.65	1.81	2.68
MnO	0.09	0.04	0.04	0.00	0.12	0.13	0.19	0.01	0.07	0.15	0.00	0.15	0.11
MgO	41.01	40.80	40.70	41.55	39.29	41.73	42.23	37.66	42.25	36.73	36.73	34.03	38.14
V_2O_5	0.04	0.00	0.04	0.10	0.49	0.14	0.00	0.13	0.07	0.00	0.00	0.00	0.12
NiO	0.00	0.13	0.04	0.00	0.13	0.04	0.06	0.00	0.00	0.03	0.00	0.01	0.13
Total	87.30	87.21	87.23	86.75	85.85	87.44	88.37	86.82	89.85	86.82	86.44	87.38	84.14
Cation proportions per 14 oxygen atoms													
Si	3.72	3.87	3.74	3.87	3.81	3.66	3.64	4.33	4.11	4.40	4.41	4.63	4.11
Ti	0.00	0.00	0.00	0.00	0.00	0.01	0.01	0.00	0.01	0.00	0.00	0.00	0.01
Al	0.00	0.00	0.00	0.00	0.17	0.00	0.00	0.01	0.00	0.00	0.00	0.00	0.01
Fe^{3+}	0.00	0.00	0.00	0.00	0.00	0.00	0.00	0.00	0.00	0.00	0.00	0.00	0.00
Fe^{2+}	0.61	0.44	0.62	0.35	0.40	0.61	0.63	0.13	0.10	0.13	0.13	0.14	0.22
Mn	0.01	0.00	0.00	0.00	0.01	0.01	0.02	0.00	0.01	0.01	0.00	0.01	0.01
Mg	5.92	5.78	5.87	5.90	5.65	6.02	6.04	5.16	5.64	5.02	5.04	4.58	5.47
V	0.00	0.00	0.00	0.01	0.04	0.01	0.00	0.01	0.00	0.00	0.00	0.00	0.01
Ni	0.00	0.01	0.00	0.00	0.01	0.00	0.00	0.00	0.00	0.00	0.00	0.00	0.01

Table 4 - 5: Representative micronalyses of chlorite from Penjwin peridotites

	Chromium - chlorite												
Oxides (wt.%)													
SiO_2	31.20	31.55	31.62	31.48	31.50	31.59	31.58	33.20	33.05	32.63	32.71	32.46	32.35
TiO_2	0.32	0.00	0.14	0.06	0.00	0.05	0.01	0.12	0.16	0.05	0.04	0.00	0.00
Al_2O_3	15.61	15.77	15.88	15.95	16.01	15.88	15.74	15.77	15.24	15.23	15.32	15.00	15.13
Fe_2O_3	0.00	0.00	0.00	0.00	0.00	0.00	0.00	0.00	0.00	0.00	0.00	0.00	0.00
FeO	3.24	3.23	3.15	2.98	3.02	2.88	2.79	3.05	2.99	2.95	2.85	2.78	2.81
MnO	0.00	0.22	0.14	0.14	0.23	0.19	0.12	0.24	0.42	0.00	0.07	0.07	0.02
MgO	34.18	34.05	33.98	34.09	34.22	34.10	33.95	34.38	33.87	33.72	33.96	33.75	33.79
CaO	0.15	0.00	0.08	0.06	0.04	0.03	0.03	0.24	0.20	0.11	0.05	0.09	0.07
Cr_2O_3	2.36	2.16	2.13	2.12	2.22	2.27	2.24	1.99	2.11	2.55	2.59	2.55	2.60
Total	87.11	86.98	87.12	86.88	87.24	86.99	86.46	89.27	88.18	87.32	87.65	86.72	86.81
Cation proportions per 28 oxygen atoms													
Si	5.94	6.00	6.00	5.99	5.97	6.00	6.03	6.10	6.16	6.15	6.15	6.16	6.14
Ti	0.05	0.00	0.02	0.01	0.00	0.01	0.00	0.02	0.02	0.01	0.01	0.00	0.00
Al	3.50	3.54	3.55	3.57	3.58	3.55	3.54	3.41	3.35	3.38	3.40	3.36	3.38
Fe^{3+}	0.00	0.00	0.00	0.00	0.00	0.00	0.00	0.00	0.00	0.00	0.00	0.00	0.00
Fe^{2+}	0.52	0.51	0.50	0.47	0.48	0.46	0.45	0.47	0.47	0.46	0.45	0.44	0.45
Mn	0.00	0.04	0.02	0.02	0.04	0.03	0.02	0.04	0.07	0.00	0.01	0.01	0.01
Mg	9.69	9.66	9.61	9.66	9.67	9.65	9.66	9.41	9.41	9.47	9.52	9.55	9.56
Ca	0.03	0.00	0.02	0.01	0.01	0.01	0.01	0.05	0.04	0.02	0.01	0.02	0.01
Cr	0.36	0.32	0.32	0.32	0.33	0.34	0.34	0.29	0.31	0.38	0.39	0.38	0.39

Table 4 - 6: Representative micronalyses of amphibole from Penjwin peridotites

	Anthopyllite												
Oxides (wt.%)													
SiO_2	60.19	60.33	60.31	59.92	59.83	59.85	59.50	59.41	59.65	59.45	59.45	59.06	58.80
TiO_2	0.00	0.00	0.00	0.00	0.00	0.24	0.27	0.22	0.22	0.00	0.00	0.00	0.00
Fe_2O_3	0.00	0.00	0.00	0.00	0.00	0.00	0.00	0.00	0.00	0.00	0.00	0.00	0.00
FeO	5.84	6.10	6.03	5.88	5.90	6.29	6.07	6.14	6.34	5.00	5.00	4.80	4.96
MnO	0.16	0.23	0.25	0.24	0.25	0.05	0.10	0.17	0.17	0.22	0.11	0.10	0.02
MgO	31.38	31.18	31.29	31.06	31.01	30.98	30.81	30.69	30.65	30.92	30.94	30.82	30.73
CaO	0.36	0.41	0.38	0.34	0.31	0.25	0.23	0.14	0.15	0.04	0.09	0.08	0.12
Cr_2O_3	0.04	0.13	0.14	0.11	0.11	0.17	0.11	0.19	0.16	0.13	0.12	0.01	0.09
V_2O_5	0.00	0.00	0.00	0.00	0.00	0.00	0.09	0.12	0.13	0.00	0.00	0.07	0.00
NiO	0.00	0.00	0.00	0.04	0.01	0.18	0.27	0.29	0.22	0.34	0.43	0.32	0.32
Total	97.97	98.38	98.40	97.59	97.42	98.01	97.36	97.25	97.56	96.10	96.14	95.19	95.04
Cation proportions per 23 oxygen atoms													
Si	8.02	8.02	8.01	8.02	8.02	8.00	7.99	7.99	8.00	8.05	8.05	8.06	8.05
Ti	0.00	0.00	0.00	0.00	0.00	0.02	0.03	0.02	0.02	0.00	0.00	0.00	0.00
Fe^{3+}	0.00	0.00	0.00	0.00	0.00	0.00	0.00	0.00	0.00	0.00	0.00	0.00	0.00
Fe^{2+}	0.65	0.68	0.67	0.66	0.66	0.70	0.68	0.69	0.71	0.57	0.57	0.55	0.57
Mn	0.02	0.03	0.03	0.03	0.03	0.01	0.01	0.02	0.02	0.03	0.01	0.01	0.00
Mg	6.23	6.18	6.20	6.20	6.20	6.17	6.17	6.15	6.13	6.24	6.24	6.27	6.27
Ca	0.05	0.06	0.05	0.05	0.04	0.04	0.03	0.02	0.02	0.01	0.01	0.01	0.02
Cr	0.00	0.01	0.01	0.01	0.01	0.02	0.01	0.02	0.02	0.01	0.01	0.00	0.01
V	0.00	0.00	0.00	0.00	0.00	0.00	0.01	0.01	0.01	0.00	0.00	0.01	0.00
Ni	0.00	0.00	0.00	0.00	0.00	0.02	0.03	0.03	0.02	0.04	0.05	0.03	0.04

Table 4 - 7: Representative micronalyses of olivine from Mawat peridotites

	Harzburgite						*Dunite*						
							green olivine				*black olivine*		
Oxides (wt.%)													
SiO_2	39.92	39.83	39.79	40.89	40.86	40.77	40.18	40.06	39.93	40.25	40.15	40.18	40.19
TiO_2	0.00	0.00	0.00	0.07	0.04	0.08	0.00	0.00	0.00	0.00	0.00	0.00	0.00
FeO	9.56	9.24	9.02	7.85	8.12	8.28	8.67	8.93	8.97	9.14	7.88	7.94	7.87
MnO	0.00	0.00	0.00	0.47	0.41	0.32	0.11	0.03	0.00	0.02	0.41	0.33	0.24
MgO	49.66	49.53	49.57	50.21	50.51	50.35	50.58	50.71	50.56	50.80	50.85	50.92	50.75
CaO	0.19	0.21	0.16	0.02	0.01	0.02	0.05	0.04	0.02	0.00	0.07	0.05	0.04
Cr_2O_3	0.22	0.20	0.20	0.00	0.00	0.00	0.00	0.00	0.00	0.00	0.12	0.07	0.14
V_2O_5	0.20	0.25	0.34	0.00	0.00	0.00	0.29	0.16	0.21	0.08	0.00	0.09	0.01
NiO	0.65	0.53	0.35	0.30	0.48	0.54	1.04	0.90	0.77	0.78	0.00	0.11	0.18
Total	100.85	100.23	99.80	100.15	100.91	100.75	100.63	100.67	100.25	100.99	99.56	99.63	99.41
Cation proportions per 4 oxygen atoms													
Si	0.97	0.97	0.97	0.99	0.99	0.99	0.98	0.98	0.98	0.98	0.98	0.98	0.99
Ti	0.00	0.00	0.00	0.00	0.00	0.00	0.00	0.00	0.00	0.00	0.00	0.00	0.00
Fe^{2+}	0.19	0.19	0.18	0.16	0.16	0.17	0.18	0.18	0.18	0.19	0.16	0.16	0.16
Mn	0.00	0.00	0.00	0.01	0.01	0.01	0.00	0.00	0.00	0.00	0.01	0.01	0.00
Mg	1.80	1.80	1.81	1.82	1.82	1.82	1.83	1.84	1.84	1.84	1.86	1.86	1.85
Ca	0.00	0.01	0.00	0.00	0.00	0.00	0.00	0.00	0.00	0.00	0.00	0.00	0.00
Cr	0.00	0.00	0.00	0.00	0.00	0.00	0.00	0.00	0.00	0.00	0.00	0.00	0.00
V	0.00	0.00	0.01	0.00	0.00	0.00	0.00	0.00	0.00	0.00	0.00	0.00	0.00
Ni	0.01	0.01	0.01	0.01	0.01	0.01	0.02	0.02	0.02	0.02	0.00	0.00	0.00
Fo	90.25	90.53	90.74	91.94	91.73	91.55	91.23	91.01	90.95	90.83	92.00	91.96	92.00

Table 4 - 8: Representative micronalyses of pyroxene in harzburgite from Mawat peridotites

	Enstatite							*Diopside*					
Oxides (wt.%)													
SiO_2	58.17	58.22	58.11	57.97	58.05	57.11	57.14	53.57	53.73	53.67	53.47	53.44	53.64
TiO_2	0.15	0.17	0.23	0.13	0.11	0.13	0.16	0.01	0.00	0.00	0.05	0.00	0.01
Al_2O_3	0.28	0.29	0.12	0.00	0.05	0.00	0.00	0.31	0.28	0.36	0.30	0.35	0.50
Fe_2O_3	0.00	0.00	0.00	0.00	0.00	0.00	0.00	0.00	0.00	0.00	0.00	0.00	0.00
FeO	5.98	6.01	5.77	5.82	5.86	6.34	6.21	3.96	4.16	4.34	4.17	4.17	4.14
MnO	0.20	0.13	0.09	0.18	0.19	0.23	0.17	0.18	0.11	0.17	0.12	0.12	0.09
MgO	34.97	34.95	34.67	34.70	34.78	34.73	34.55	17.09	17.10	17.02	16.93	17.01	17.03
CaO	1.09	1.12	1.13	1.13	1.14	1.29	1.22	23.37	23.24	23.29	23.17	23.19	23.41
Cr_2O_3	0.43	0.34	0.32	0.38	0.36	0.68	0.73	0.58	0.67	0.50	0.54	0.47	0.45
V_2O_5	0.00	0.00	0.00	0.00	0.00	0.00	0.00	0.28	0.22	0.27	0.25	0.28	0.20
Total	101.27	101.23	100.44	100.31	100.54	100.51	100.18	99.07	99.29	99.35	98.75	98.75	99.27
Cation proportions per 6 oxygen atoms													
Si	1.98	1.98	1.99	1.99	1.99	1.97	1.98	1.97	1.98	1.97	1.98	1.98	1.97
Ti	0.00	0.00	0.01	0.00	0.00	0.00	0.00	0.00	0.00	0.00	0.00	0.00	0.00
Al	0.01	0.01	0.00	0.00	0.00	0.00	0.00	0.01	0.01	0.02	0.01	0.02	0.02
Fe^{3+}	0.00	0.00	0.00	0.00	0.00	0.00	0.00	0.00	0.00	0.00	0.00	0.00	0.00
Fe^{2+}	0.17	0.17	0.17	0.17	0.17	0.18	0.18	0.12	0.13	0.13	0.13	0.13	0.13
Mn	0.01	0.00	0.00	0.01	0.01	0.01	0.00	0.01	0.00	0.01	0.00	0.00	0.00
Mg	1.78	1.78	1.77	1.78	1.78	1.79	1.78	0.94	0.94	0.93	0.93	0.94	0.93
Ca	0.04	0.04	0.04	0.04	0.04	0.05	0.05	0.92	0.92	0.92	0.92	0.92	0.92
Cr	0.01	0.01	0.01	0.01	0.01	0.02	0.02	0.02	0.02	0.01	0.02	0.01	0.01
V	0.00	0.00	0.00	0.00	0.00	0.00	0.00	0.01	0.01	0.01	0.01	0.01	0.00

Table 4 - 9: Representative micronalyses of spinel from Mawat pertidotites

	Harzburgite							*Dunite*					
Oxides (wt.%)													
SiO_2	0.95	0.87	0.79	0.79	0.93	0.92	2.69	0.75	0.71	0.79	0.73	0.93	0.66
TiO_2	0.12	0.13	0.00	0.00	0.00	0.01	0.00	0.25	0.09	0.20	0.16	0.37	0.10
Al_2O_3	19.37	19.51	19.40	19.42	19.69	19.84	18.73	9.19	9.21	9.28	9.30	9.48	9.75
Fe_2O_3	0.00	0.00	0.00	0.00	0.00	0.00	0.00	0.00	0.00	0.00	0.00	0.00	0.00
FeO	19.08	18.98	18.57	18.79	18.88	18.77	21.64	22.21	22.37	22.49	22.53	22.03	21.54
MnO	0.00	0.00	0.13	0.17	0.15	0.14	0.16	0.83	0.88	0.80	0.82	1.08	1.53
MgO	8.19	8.21	8.18	8.28	8.33	8.34	4.86	5.52	5.53	5.57	5.54	5.14	5.52
Cr_2O_3	52.13	51.75	51.68	51.62	51.60	51.62	50.73	60.01	59.75	59.87	60.06	59.56	58.52
V_2O_5	0.10	0.23	0.38	0.44	0.52	0.49	0.78	0.32	0.47	0.42	0.31	1.13	1.46
NiO	0.00	0.00	0.00	0.00	0.00	0.00	0.00	0.00	0.00	0.00	0.00	0.43	0.04
Total	99.94	99.68	99.13	99.51	100.10	100.14	99.91	99.14	99.01	99.43	99.53	100.15	99.12
Cation proportions per 4 oxygen atoms													
Si	0.03	0.03	0.03	0.03	0.03	0.03	0.09	0.03	0.02	0.03	0.02	0.03	0.02
Ti	0.00	0.00	0.00	0.00	0.00	0.00	0.00	0.01	0.00	0.01	0.00	0.01	0.00
Al	0.72	0.73	0.73	0.73	0.73	0.74	0.70	0.37	0.37	0.37	0.37	0.38	0.39
Fe^{3+}	0.00	0.00	0.00	0.00	0.00	0.00	0.00	0.00	0.00	0.00	0.00	0.00	0.00
Fe^{2+}	0.50	0.50	0.49	0.50	0.50	0.49	0.58	0.63	0.64	0.64	0.64	0.62	0.61
Mn	0.00	0.00	0.00	0.00	0.00	0.00	0.00	0.02	0.03	0.02	0.02	0.03	0.04
Mg	0.39	0.39	0.39	0.39	0.39	0.39	0.23	0.28	0.28	0.28	0.28	0.26	0.28
Ca	0.00	0.00	0.00	0.00	0.00	0.00	0.01	0.00	0.00	0.00	0.00	0.00	0.00
Cr	1.30	1.30	1.30	1.30	1.28	1.28	1.28	1.62	1.61	1.61	1.61	1.58	1.57
V	0.00	0.00	0.01	0.01	0.01	0.01	0.02	0.01	0.01	0.01	0.01	0.03	0.03
Cr#	64.35	64.02	64.12	64.07	63.74	63.57	64.50	81.41	81.31	81.23	81.25	80.82	80.10

Cr# = Cr * 100 / (Cr + Al)

Table 4 -10: Representative micronalyses of serpentine from Mawat pertidotites

	Lizardite/ chrysotile												
Oxides (wt.%)													
SiO_2	44.60	45.76	45.96	44.84	44.25	44.35	44.35	44.09	44.96	45.02	44.95	44.10	45.39
TiO_2	0.01	0.00	0.08	0.00	0.00	0.04	0.04	0.04	0.02	0.02	0.00	0.00	0.02
Al_2O_3	0.00	0.00	0.00	0.04	0.00	0.00	0.00	0.00	0.00	0.00	0.00	0.00	0.00
Fe_2O_3	0.00	0.00	0.00	0.00	0.00	0.00	0.00	0.00	0.00	0.00	0.00	0.00	0.00
FeO	1.86	2.07	2.66	2.39	2.84	2.64	2.64	2.35	2.70	2.35	2.14	2.61	2.35
MnO	0.12	0.04	0.20	0.01	0.07	0.16	0.16	0.25	0.19	0.11	0.16	0.01	0.08
MgO	40.65	41.03	41.68	40.45	38.55	38.91	38.91	39.86	39.81	39.85	39.18	39.07	41.92
CaO	0.00	0.15	0.06	0.07	0.02	0.08	0.08	0.07	0.04	0.06	0.14	0.06	0.02
Cr_2O_3	0.38	0.00	0.07	0.05	0.00	0.00	0.00	0.00	0.00	0.19	0.12	0.42	0.05
V_2O_5	0.00	0.14	0.06	0.15	0.00	0.05	0.05	0.05	0.00	0.00	0.00	0.11	0.00
Total	87.66	89.05	90.78	87.93	85.75	86.18	86.18	86.66	87.75	87.64	86.71	86.28	90.73
Cation proportions per 14 oxygen atoms													
Si	4.11	4.14	33.40	4.12	4.17	4.16	4.16	4.12	4.15	4.15	4.18	4.13	4.07
Ti	0.00	0.00	0.04	0.00	0.00	0.00	0.00	0.00	0.00	0.00	0.00	0.00	0.00
Al	0.00	0.00	0.00	0.00	0.00	0.00	0.00	0.00	0.00	0.00	0.00	0.00	0.00
Fe^{3+}	0.00	0.00	0.00	0.00	0.00	0.00	0.00	0.00	0.00	0.00	0.00	0.00	0.00
Fe^{2+}	0.14	0.16	1.62	0.18	0.22	0.21	0.21	0.18	0.21	0.18	0.17	0.20	0.18
Mn	0.01	0.00	0.12	0.00	0.01	0.01	0.01	0.02	0.01	0.01	0.01	0.00	0.01
Mg	5.58	5.53	45.15	5.54	5.42	5.44	5.44	5.55	5.47	5.48	5.43	5.46	5.60
Ca	0.00	0.01	0.05	0.01	0.00	0.01	0.01	0.01	0.00	0.01	0.01	0.01	0.00

Table 4 -11: Representative micronalyses of olivine from Pauza pertidotites

	Lherzolite				*Harzburgite*				*Dunite*				
Oxides (wt.%)													
SiO_2	39.68	39.19	39.20	39.24	39.33	39.11	39.35	39.15	40.93	40.75	40.68	40.57	40.72
TiO_2	0.08	0.16	0.12	0.07	0.12	0.10	0.02	0.02	0.01	0.00	0.00	0.00	0.00
Al_2O_3	0.02	0.00	0.02	0.00	0.52	0.03	0.00	0.03	0.44	0.40	0.21	0.14	0.39
FeO	8.85	8.84	8.82	8.91	8.42	8.41	8.00	7.93	7.69	7.64	7.45	7.52	7.40
MnO	0.15	0.44	0.43	0.40	0.00	0.00	0.00	0.00	0.08	0.13	0.13	0.13	0.31
MgO	52.47	52.07	51.63	51.27	52.16	52.46	52.46	52.33	50.92	50.84	50.63	50.47	50.78
CaO	0.00	0.04	0.08	0.11	0.00	0.00	0.00	0.00	0.07	0.08	0.08	0.04	0.00
Cr_2O_3	0.00	0.00	0.00	0.00	0.17	0.14	0.12	0.07	0.00	0.00	0.00	0.00	0.00
V_2O_5	0.00	0.00	0.00	0.00	0.00	0.00	0.00	0.00	0.02	0.07	0.00	0.00	0.32
NiO	0.00	0.00	0.00	0.00	0.00	0.00	0.14	0.05	0.37	0.37	0.39	0.32	0.46
Total	101.25	100.74	100.30	100.00	100.72	100.25	100.97	100.53	100.51	100.21	99.57	99.19	100.06
Cation proportions per 4 oxygen atoms													
Si	0.96	0.96	0.96	0.96	0.95	0.96	0.96	0.95	0.99	0.99	0.99	0.99	0.99
Ti	0.00	0.00	0.00	0.00	0.00	0.00	0.00	0.00	0.00	0.00	0.00	0.00	0.00
Al	0.00	0.00	0.00	0.00	0.01	0.00	0.00	0.00	0.01	0.01	0.01	0.00	0.01
Fe^{2+}	0.18	0.18	0.18	0.18	0.17	0.17	0.16	0.16	0.16	0.15	0.15	0.15	0.15
Mn	0.00	0.01	0.01	0.01	0.00	0.00	0.00	0.00	0.00	0.00	0.00	0.00	0.01
Mg	1.89	1.89	1.88	1.88	1.89	1.91	1.90	1.90	1.83	1.84	1.84	1.84	1.83
Ca	0.00	0.00	0.00	0.00	0.00	0.00	0.00	0.00	0.00	0.00	0.00	0.00	0.00
Cr	0.00	0.00	0.00	0.00	0.00	0.00	0.00	0.00	0.00	0.00	0.00	0.00	0.00
V	0.00	0.00	0.00	0.00	0.00	0.00	0.00	0.00	0.00	0.00	0.00	0.00	0.01
Ni	0.00	0.00	0.00	0.00	0.00	0.00	0.00	0.00	0.01	0.01	0.01	0.01	0.01
Fo	91.36	91.30	91.25	91.12	91.70	91.75	92.12	92.16	92.19	92.22	92.37	92.29	92.44

Table 4 -12: Representative micronalyses of pyroxene in harzburgite from Pauza pertidotites

	Enstatite							*Augite*					
Oxides (wt.%)													
SiO_2	55.56	55.53	55.41	55.53	55.72	54.80	54.66	54.30	54.51	54.56	54.88	55.24	54.94
TiO_2	0.00	0.00	0.00	0.00	0.00	0.00	0.00	0.05	0.00	0.12	0.00	0.04	0.13
Al_2O_3	1.21	1.07	0.98	0.99	0.97	1.27	1.09	6.96	6.60	6.71	6.66	6.61	6.60
FeO	5.34	5.94	6.02	6.01	6.02	6.16	6.08	3.24	2.46	2.81	2.82	2.98	3.00
MnO	0.00	0.00	0.00	0.00	0.00	0.00	0.00	0.00	0.15	0.19	0.12	0.23	0.20
MgO	37.01	36.99	36.85	37.01	37.11	36.71	36.19	21.12	22.33	22.06	22.11	22.16	22.23
CaO	0.07	0.11	0.13	0.15	0.17	0.07	0.05	12.81	13.63	12.55	12.69	12.47	12.48
Na_2O	0.66	0.88	0.93	0.95	0.93	0.55	0.50	0.00	0.00	0.00	0.00	0.00	0.00
Cr_2O_3	0.16	0.12	0.04	0.06	0.07	0.20	0.24	0.78	0.05	0.22	0.48	0.58	0.59
NiO	0.11	0.15	0.08	0.08	0.17	0.15	0.47	0.00	0.00	0.00	0.00	0.00	0.00
Total	100.12	100.79	100.44	100.78	101.16	99.97	99.28	99.26	99.73	99.22	99.76	100.31	100.17
Cation proportions per 6 oxygen atoms													
Si	1.92	1.91	1.91	1.91	1.91	1.90	1.91	1.28	1.28	1.28	1.28	1.28	1.28
Ti	0.00	0.00	0.00	0.00	0.00	0.00	0.00	0.00	0.00	0.00	0.00	0.00	0.00
Al	0.05	0.04	0.04	0.04	0.04	0.05	0.04	0.19	0.18	0.19	0.18	0.18	0.18
Fe^{2+}	0.15	0.17	0.17	0.17	0.17	0.18	0.18	0.06	0.05	0.06	0.06	0.06	0.06
Mn	0.00	0.00	0.00	0.00	0.00	0.00	0.00	0.00	0.00	0.00	0.00	0.00	0.00
Mg	1.90	1.90	1.90	1.90	1.90	1.90	1.89	0.74	0.78	0.77	0.77	0.77	0.77
Ca	0.00	0.00	0.00	0.01	0.01	0.00	0.00	0.32	0.34	0.32	0.32	0.31	0.31
Na	0.04	0.06	0.06	0.06	0.06	0.04	0.03	0.00	0.00	0.00	0.00	0.00	0.00
Cr	0.00	0.00	0.00	0.00	0.00	0.01	0.01	0.01	0.00	0.00	0.01	0.01	0.01
Ni	0.00	0.00	0.00	0.00	0.00	0.00	0.01	0.00	0.00	0.00	0.00	0.00	0.00

Table 4 -13: Representative micronalyses of spinel from Pauza pertidotites

	Harzburgite							*Dunite*					
Oxides (wt.%)													
SiO_2	0.16	0.06	0.16	0.11	0.11	0.13	0.14	0.49	0.46	0.42	1.12	0.42	0.29
TiO_2	0.01	0.09	0.21	0.28	0.18	0.11	0.11	0.00	0.00	0.00	0.21	0.37	0.29
Al_2O_3	20.09	20.23	20.08	20.11	19.99	20.01	20.11	7.48	7.44	7.43	6.94	6.53	6.94
Fe_2O_3	0.00	0.00	0.00	0.00	0.00	0.00	0.00	1.76	2.16	2.21	4.24	2.82	3.07
FeO	26.64	27.61	27.27	27.62	27.49	27.55	27.66	26.54	26.37	26.37	27.05	26.83	26.49
MnO	0.00	0.00	0.00	0.00	0.00	0.00	0.00	0.47	0.41	0.38	1.01	0.67	0.53
MgO	10.07	9.89	9.48	9.53	9.36	9.36	9.41	4.96	5.05	5.06	5.06	4.66	4.90
Cr_2O_3	42.19	41.92	41.96	42.11	42.11	42.35	42.43	57.12	57.01	57.00	56.24	57.25	57.93
V_2O_5	0.00	0.00	0.00	0.00	0.00	0.00	0.00	0.66	0.61	0.61	0.27	0.44	0.32
NiO	0.00	0.00	0.00	0.00	0.00	0.00	0.00	0.21	0.17	0.09	0.00	0.00	0.00
Total	99.37	99.92	99.21	99.92	99.33	99.57	99.93	99.70	99.68	99.57	102.21	99.99	100.76
Cation proportions per 4 oxygen atoms													
Si	0.01	0.00	0.01	0.00	0.00	0.00	0.00	0.02	0.02	0.01	0.04	0.01	0.01
Ti	0.00	0.00	0.01	0.01	0.00	0.00	0.00	0.00	0.00	0.00	0.01	0.01	0.01
Al	0.77	0.77	0.77	0.77	0.77	0.77	0.77	0.31	0.30	0.30	0.28	0.27	0.28
Fe^{3+}	0.00	0.00	0.00	0.00	0.00	0.00	0.00	0.05	0.06	0.06	0.11	0.07	0.08
Fe^{2+}	0.72	0.75	0.74	0.75	0.75	0.75	0.75	0.77	0.77	0.77	0.77	0.78	0.76
Mn	0.00	0.00	0.00	0.00	0.00	0.00	0.00	0.01	0.01	0.01	0.03	0.02	0.02
Mg	0.49	0.48	0.46	0.46	0.45	0.45	0.45	0.26	0.26	0.26	0.26	0.24	0.25
Cr	1.08	1.07	1.08	1.08	1.08	1.09	1.09	1.57	1.57	1.57	1.51	1.58	1.58
V	0.00	0.00	0.00	0.00	0.00	0.00	0.00	0.02	0.01	0.01	0.01	0.01	0.01
Ni	0.00	0.00	0.00	0.00	0.00	0.00	0.00	0.01	0.00	0.00	0.00	0.00	0.00
Cr #	58.48	58.16	58.36	58.41	58.56	58.67	58.60	83.67	83.71	83.73	84.46	85.47	84.85

Cr # = Cr * 100 / (Cr + Al)

Table 4 -14: Representative micronalyses of spinel in spinel lherzolite from Pauza pertidotites

	Spinel lherzolite												
Oxides (wt.%)													
SiO_2	0.00	0.00	0.00	0.00	0.00	0.16	0.08	0.13	0.14	0.10	0.15	0.15	0.16
TiO_2	0.02	0.18	0.09	0.00	0.00	0.00	0.00	0.00	0.00	0.00	0.00	0.02	0.03
Al_2O_3	37.10	36.69	36.52	36.62	36.63	35.75	35.56	35.46	35.38	35.45	35.53	35.33	35.41
Fe_2O_3	0.00	0.00	0.00	0.00	0.00	0.00	0.00	0.00	0.00	0.00	0.00	0.00	0.00
FeO	21.77	22.58	23.22	23.01	22.76	24.89	24.51	24.15	23.75	23.73	23.60	23.59	23.59
MnO	0.00	0.00	0.00	0.00	0.00	0.00	0.00	0.00	0.00	0.00	0.00	0.00	0.00
MgO	13.46	13.43	13.53	13.63	13.58	13.36	13.34	13.22	13.16	13.04	13.09	13.06	13.08
Cr_2O_3	26.75	26.45	26.20	25.95	26.17	27.44	27.56	27.55	27.68	27.47	27.36	27.30	27.20
V_2O_5	0.00	0.00	0.00	0.00	0.00	0.00	0.00	0.00	0.00	0.00	0.00	0.00	0.00
NiO	0.00	0.00	0.00	0.00	0.00	0.00	0.00	0.00	0.00	0.00	0.00	0.00	0.00
Total	99.14	99.39	99.65	99.27	99.16	101.82	101.21	100.66	100.28	100.01	99.90	99.58	99.61
Cation proportions per 4 oxygen atoms													
Si	0.00	0.00	0.00	0.00	0.00	0.00	0.00	0.00	0.00	0.00	0.00	0.00	0.00
Ti	0.00	0.00	0.00	0.00	0.00	0.00	0.00	0.00	0.00	0.00	0.00	0.00	0.00
Al	1.29	1.28	1.27	1.28	1.28	1.23	1.23	1.23	1.23	1.24	1.24	1.24	1.24
Fe^{3+}	0.00	0.00	0.00	0.00	0.00	0.00	0.00	0.00	0.00	0.00	0.00	0.00	0.00
Fe^{2+}	0.54	0.56	0.57	0.57	0.56	0.61	0.60	0.60	0.59	0.59	0.58	0.59	0.59
Mn	0.00	0.00	0.00	0.00	0.00	0.00	0.00	0.00	0.00	0.00	0.00	0.00	0.00
Mg	0.59	0.59	0.60	0.60	0.60	0.58	0.58	0.58	0.58	0.58	0.58	0.58	0.58
Cr	0.62	0.62	0.61	0.61	0.61	0.63	0.64	0.64	0.65	0.64	0.64	0.64	0.64
V	0.00	0.00	0.00	0.00	0.00	0.00	0.00	0.00	0.00	0.00	0.00	0.00	0.00
Ni	0.00	0.00	0.00	0.00	0.00	0.00	0.00	0.00	0.00	0.00	0.00	0.00	0.00
Cr #	32.60	32.60	32.49	32.22	32.40	33.99	34.21	34.26	34.42	34.20	34.06	34.14	34.00

Cr # = Cr * 100 / (Cr + Al)

Table 6 - 1: Representative micronalyses of albite from Mlakawa albitite

	Albite							
Oxides (wt. %)								
SiO_2	64.77	64.85	64.60	65.67	65.70	66.45	66.00	65.88
TiO_2	0.52	0.11	0.04	0.01	0.00	0.00	0.00	0.00
Al_2O_3	20.61	20.40	20.20	20.25	20.22	20.44	20.41	20.26
Fe_2O_3	0.00	0.00	0.00	0.00	0.00	0.00	0.00	0.00
FeO	0.21	0.29	0.17	0.40	0.00	0.00	0.00	0.00
MnO	0.01	0.07	0.16	0.17	0.00	0.07	0.04	0.00
MgO	0.00	0.00	0.00	0.00	0.00	0.00	0.00	0.00
CaO	0.79	0.76	0.71	0.53	0.11	0.14	0.07	0.08
Na_2O	13.34	12.97	13.04	13.00	13.28	13.38	13.25	13.13
K_2O	0.11	0.03	0.00	0.05	0.02	0.04	0.07	0.02
P_2O_5	0.00	0.00	0.00	0.00	0.00	0.00	0.00	0.00
Cr_2O_3	0.00	0.00	0.00	0.00	0.03	0.00	0.00	0.00
V_2O_5	0.02	0.21	0.11	0.04	0.00	0.02	0.03	0.00
Total	100.38	99.69	99.03	100.12	99.36	100.54	99.87	99.37
Cation proportions per 8 oxygen atoms								
Si	2.87	2.88	2.89	2.90	2.92	2.92	2.92	2.92
Ti	0.02	0.00	0.00	0.00	0.00	0.00	0.00	0.00
Al	1.07	1.07	1.06	1.06	1.06	1.06	1.06	1.06
Fe^{3+}	0.00	0.00	0.00	0.00	0.00	0.00	0.00	0.00
Fe^{2+}	0.01	0.01	0.01	0.01	0.00	0.00	0.00	0.00
Mn	0.00	0.00	0.01	0.01	0.00	0.00	0.00	0.00
Mg	0.00	0.00	0.00	0.00	0.00	0.00	0.00	0.00
Ca	0.04	0.04	0.03	0.03	0.01	0.01	0.00	0.00
Na	1.14	1.12	1.13	1.11	1.14	1.14	1.13	1.13
K	0.01	0.00	0.00	0.00	0.00	0.00	0.00	0.00
P	0.00	0.00	0.00	0.00	0.00	0.00	0.00	0.00
Cr	0.00	0.00	0.00	0.00	0.00	0.00	0.00	0.00
V	0.00	0.01	0.00	0.00	0.00	0.00	0.00	0.00
Ab	96.00	97.00	97.00	98.00	99.00	99.00	99.00	100.00
An	3.00	3.00	3.00	2.00	1.00	1.00	0.00	0.00
Or	1.00	0.00	0.00	0.00	0.00	0.00	0.00	0.00

Table 6 - 2: Representative micronalyses of titanite from Mlakawa albitite

	Titanite							
	Type I			*Type II*			*Type III*	
Oxides (wt. %)								
SiO_2	32.97	32.91	32.89	32.47	32.46	32.51	32.02	32.37
TiO_2	34.29	34.11	34.12	32.96	33.05	33.21	36.60	36.92
Al_2O_3	3.61	3.63	3.62	4.54	4.59	4.50	1.41	1.26
FeO_{total}	0.96	0.86	0.87	0.61	0.61	0.62	0.59	0.68
MnO	0.02	0.05	0.00	0.12	0.13	0.14	0.03	0.08
MgO	0.31	0.30	0.29	0.07	0.08	0.07	0.03	0.03
CaO	28.60	28.46	28.36	28.48	28.53	28.58	28.68	28.71
Na_2O	0.01	0.00	0.02	0.00	0.00	0.00	0.00	0.05
K_2O	0.03	0.02	0.01	0.03	0.05	0.00	0.07	0.04
F	ND	ND	ND	ND	ND	ND	ND	ND
Total	100.82	100.44	100.18	99.28	99.50	99.63	99.43	100.24
Cation proportions per 4 oxygen atoms								
Si	1.00	1.00	1.00	1.00	1.00	1.00	1.00	1.00
Ti	0.78	0.78	0.78	0.77	0.77	0.77	0.86	0.86
Al	0.13	0.13	0.13	0.16	0.17	0.16	0.05	0.05
Fe^{2+}	0.02	0.02	0.02	0.02	0.02	0.02	0.02	0.02
Mn	0.00	0.00	0.00	0.00	0.00	0.00	0.00	0.00
Mg	0.01	0.01	0.01	0.00	0.00	0.00	0.00	0.00
Ca	0.93	0.93	0.92	0.94	0.94	0.94	0.96	0.95
Na	0.00	0.00	0.00	0.00	0.00	0.00	0.00	0.00
K	0.00	0.00	0.00	0.00	0.00	0.00	0.00	0.00

Table 6 - 3: Representative micronalyses of analcime from Mlakawa albitite

	Analcime							
Oxides (wt. %)								
SiO_2	55.08	54.98	54.89	55.22	55.17	55.13	55.17	55.24
TiO_2	0.00	0.00	0.00	0.00	0.00	0.00	0.00	0.00
Al_2O_3	23.39	23.43	23.29	23.27	23.46	23.46	23.53	23.30
Fe_2O_3	0.00	0.00	0.00	0.00	0.00	0.00	0.00	0.00
FeO	0.12	0.23	0.13	0.12	0.06	0.02	0.04	0.17
MnO	0.00	0.00	0.00	0.00	0.00	0.00	0.00	0.00
MgO	0.04	0.00	0.00	0.00	0.00	0.00	0.01	0.00
CaO	0.15	0.00	0.00	0.00	0.02	0.00	0.00	0.09
Na_2O	14.78	14.25	14.20	14.10	13.83	13.59	13.53	15.75
K_2O	0.15	0.25	0.24	0.22	0.21	0.19	0.20	0.28
P_2O_5	0.00	0.00	0.00	0.00	0.00	0.00	0.00	0.00
Cr_2O_3	0.07	0.10	0.08	0.05	0.06	0.00	0.00	0.00
V_2O_5	0.00	0.01	0.01	0.00	0.00	0.00	0.01	0.33
Total	93.78	93.24	92.83	92.98	92.81	92.39	92.48	94.83
Cation proportions per 8 oxygen atoms								
Si	1.99	1.99	1.99	2.00	2.00	2.00	2.00	1.97
Ti	0.00	0.00	0.00	0.00	0.00	0.00	0.00	0.00
Al	0.99	1.00	1.00	0.99	1.00	1.01	1.01	0.98
Fe^{3+}	0.00	0.00	0.00	0.00	0.00	0.00	0.00	0.00
Fe^{2+}	0.00	0.01	0.00	0.00	0.00	0.00	0.00	0.01
Mn	0.00	0.00	0.00	0.00	0.00	0.00	0.00	0.00
Mg	0.00	0.00	0.00	0.00	0.00	0.00	0.00	0.00
Ca	0.01	0.00	0.00	0.00	0.00	0.00	0.00	0.00
Na	1.03	1.00	1.00	0.99	0.97	0.96	0.95	1.09
K	0.01	0.01	0.01	0.01	0.01	0.01	0.01	0.01
P	0.00	0.00	0.00	0.00	0.00	0.00	0.00	0.00
Cr	0.00	0.00	0.00	0.00	0.00	0.00	0.00	0.00
V	0.00	0.00	0.00	0.00	0.00	0.00	0.00	0.01

Table 6 - 4: Representative micronalyses of apatite from Mlakawa albitite

				Apatite				
Oxides (wt. %)								
CaO	53.61	52.91	53.00	52.00	6.53	6.42	6.22	6.25
P_2O_5	46.81	46.70	47.00	47.69	35.00	34.00	34.52	34.73
SrO	0.00	0.00	0.00	0.00	52.00	54.00	53.00	53.00
SiO_2	0.00	0.00	0.00	0.00	5.30	4.33	4.14	5.00
Na_2O	0.00	0.03	0.03	0.04	0.14	0.11	0.19	0.14
Total	100.42	99.64	100.03	99.73	98.97	98.86	98.07	99.12
Cation proportions per 25 oxygen atoms								
Ca	9.17	9.11	9.08	8.89	1.43	1.45	1.40	1.39
P	6.33	6.35	6.36	6.44	6.07	6.05	6.22	6.04
Sr	0.00	0.00	0.00	0.00	6.18	6.58	6.35	6.40
Si	0.00	0.00	0.00	0.00	1.09	0.91	0.87	1.04
Na	0.00	0.01	0.01	0.01	0.05	0.05	0.08	0.05

Table 6 - 5: Representative micronalyses of allanite from Mlakawa albitite

	Allanite							
Oxides (wt. %)								
SiO_2	34.01	33.92	32.82	32.94	32.58	32.43	32.48	33.99
TiO_2	0.47	0.51	0.73	0.75	0.86	1.09	1.06	0.18
Al_2O_3	18.65	18.42	15.87	15.94	15.09	15.15	15.07	20.00
Fe_2O_3	0.00	0.00	0.00	0.00	0.00	0.00	0.00	0.00
FeO	10.81	10.90	12.14	12.17	13.66	13.74	13.46	10.26
MnO	0.19	0.16	0.39	0.43	0.50	0.37	0.42	0.00
MgO	0.55	0.43	0.70	0.69	0.52	0.54	0.58	0.29
CaO	13.83	13.85	12.01	11.97	11.62	11.81	11.60	14.80
Na_2O	0.00	0.00	0.00	0.00	0.00	0.00	0.00	0.00
K_2O	0.05	0.12	0.00	0.00	0.00	0.00	0.00	0.00
P_2O_5	0.00	0.00	0.00	0.00	0.00	0.00	0.00	0.00
Cr_2O_3	0.00	0.00	0.00	0.00	0.00	0.09	0.22	0.00
V_2O_5	0.37	0.26	0.00	0.00	0.14	0.00	0.00	0.35
La_2O_3	8.40	8.47	9.24	9.22	8.47	8.77	8.92	7.46
Ce_2O_3	10.88	10.75	11.72	11.87	13.50	13.39	13.10	9.47
Nd_2O_3	0.89	0.77	1.88	1.92	2.01	2.04	2.28	1.28
Total	99.10	98.56	97.50	97.90	98.95	99.42	99.19	98.08
Cation proportions per 11.5 oxygen atoms								
Si	3.08	3.09	3.17	3.17	3.16	3.14	3.16	3.03
Ti	0.03	0.03	0.05	0.05	0.06	0.08	0.08	0.01
Al	1.99	1.97	1.80	1.81	1.73	1.73	1.73	2.10
Fe^{3+}	0.00	0.00	0.00	0.00	0.00	0.00	0.00	0.00
Fe^{2+}	0.82	0.83	0.98	0.98	1.11	1.11	1.09	0.76
Mn	0.01	0.01	0.03	0.04	0.04	0.03	0.03	0.00
Mg	0.07	0.06	0.10	0.10	0.08	0.08	0.08	0.04
Ca	1.34	1.35	1.24	1.23	1.21	1.23	1.21	1.41
Na	0.00	0.00	0.00	0.00	0.00	0.00	0.00	0.00
K	0.01	0.01	0.00	0.00	0.00	0.00	0.00	0.00
P	0.00	0.00	0.00	0.00	0.00	0.00	0.00	0.00
Cr	0.00	0.00	0.00	0.00	0.00	0.01	0.02	0.00
V	0.02	0.02	0.00	0.00	0.01	0.00	0.00	0.02

Table 6 - 6: Representative micronalyses of muscovite from Mlakawa albitite

	Muscovite							
	Core			*Transitional*			*Rim*	
Oxides (wt. %)								
SiO_2	41.41	41.47	41.57	39.37	39.24	39.15	39.16	39.35
TiO_2	0.01	0.00	0.03	0.00	0.00	0.00	0.00	0.03
Al_2O_3	41.46	41.43	41.46	41.93	41.77	41.94	39.20	39.25
Fe_2O_3	0.00	0.00	0.00	0.00	0.00	0.00	0.00	0.00
FeO	0.14	0.11	0.12	0.00	0.00	0.00	0.00	0.00
MnO	0.12	0.04	0.05	0.00	0.00	0.00	0.00	0.00
MgO	0.11	0.12	0.12	0.14	0.11	0.13	0.42	0.28
CaO	0.13	0.15	0.12	0.11	0.15	0.14	0.02	0.08
Na_2O	0.75	0.79	0.80	0.62	0.57	0.56	0.22	0.23
K_2O	10.06	9.94	9.91	8.12	7.97	7.96	8.23	8.23
P_2O_5	0.00	0.00	0.00	0.00	0.00	0.00	0.00	0.00
Cr_2O_3	0.00	0.00	0.00	0.07	0.04	0.06	0.00	0.00
V_2O_5	0.00	0.03	0.03	0.00	0.00	0.06	0.10	0.02
BaO	1.43	1.41	1.33	5.16	5.20	5.15	9.28	9.14
Total	94.19	94.05	94.18	90.36	89.85	89.94	87.25	87.45
Cation proportions per 22 oxygen atoms								
Si	5.56	5.57	5.57	5.45	5.45	5.43	5.60	5.62
Ti	0.00	0.00	0.00	0.00	0.00	0.00	0.00	0.00
Al	6.56	6.56	6.55	6.84	6.84	6.86	6.60	6.60
Fe^{3+}	0.00	0.00	0.00	0.00	0.00	0.00	0.00	0.00
Fe^{2+}	0.02	0.01	0.01	0.00	0.00	0.00	0.00	0.00
Mn	0.01	0.00	0.01	0.00	0.00	0.00	0.00	0.00
Mg	0.02	0.02	0.02	0.03	0.02	0.03	0.09	0.06
Ca	0.02	0.02	0.02	0.02	0.02	0.02	0.00	0.01
Na	0.20	0.21	0.21	0.17	0.15	0.15	0.06	0.06
K	1.72	1.70	1.70	1.43	1.41	1.41	1.50	1.50
P	0.00	0.00	0.00	0.00	0.00	0.00	0.00	0.00
Cr	0.00	0.00	0.00	0.01	0.00	0.01	0.00	0.00
V	0.00	0.00	0.00	0.00	0.00	0.01	0.01	0.00
Ba	0.07	0.07	0.07	0.28	0.28	0.28	0.51	0.50

Table 6 - 7: Representative micronalyses of barium feldsbar from Mlakawa albitite

	Cymerite				*Celesian*			
Oxides (wt. %)								
SiO_2	30.84	30.84	30.78	30.78	32.30	33.00	32.30	32.11
TiO_2	0.00	0.00	0.00	0.00	0.00	0.00	0.00	0.00
Al_2O_3	25.21	25.21	25.20	25.20	26.40	26.20	25.97	26.00
Fe_2O_3	0.00	0.00	0.00	0.00	0.00	0.00	0.00	0.00
FeO	0.00	0.00	0.00	0.00	0.06	0.00	0.00	0.36
MnO	0.00	0.00	0.00	0.00	0.00	0.00	0.00	0.00
MgO	0.07	0.07	0.12	0.12	0.00	0.00	0.00	0.07
CaO	0.10	0.10	0.07	0.07	0.08	0.09	0.09	0.23
Na_2O	0.39	0.39	0.39	0.39	0.63	0.65	0.56	0.67
K_2O	0.88	0.88	0.84	0.84	0.31	0.30	0.31	1.02
P_2O_5	0.00	0.00	0.00	0.00	0.00	0.00	0.00	0.00
Cr_2O_3	0.00	0.00	0.01	0.01	0.15	0.12	0.14	0.11
V_2O_5	0.48	0.48	0.36	0.36	0.09	0.14	0.09	0.23
BaO	36.90	38.72	37.82	36.82	39.50	40.00	40.10	40.56
Total	94.87	96.69	95.59	94.59	99.52	100.50	99.56	101.36
Cation proportions per 8 oxygen atoms								
Si	2.28	2.28	2.28	2.28	2.30	2.31	2.31	2.29
Ti	0.00	0.00	0.00	0.00	0.00	0.00	0.00	0.00
Al	2.20	2.20	2.20	2.20	2.20	2.19	2.20	2.16
Fe^{3+}	0.00	0.00	0.00	0.00	0.00	0.00	0.00	0.00
Fe^{2+}	0.00	0.00	0.00	0.00	0.00	0.00	0.00	0.02
Mn	0.00	0.00	0.00	0.00	0.00	0.00	0.00	0.00
Mg	0.01	0.01	0.01	0.01	0.00	0.00	0.00	0.01
Ca	0.01	0.01	0.01	0.01	0.01	0.01	0.01	0.02
Na	0.06	0.06	0.06	0.06	0.09	0.09	0.08	0.10
K	0.08	0.08	0.08	0.08	0.03	0.03	0.03	0.10
P	0.00	0.00	0.00	0.00	0.00	0.00	0.00	0.00
Cr	0.00	0.00	0.00	0.00	0.01	0.01	0.01	0.01
V	0.02	0.02	0.02	0.02	0.00	0.01	0.00	0.01
Ba	1.02	1.00	0.99	0.99	0.97	0.99	0.98	1.03

Table 6 -8: Representative micronalyses of amphibole from Mlakawa albitite

	Amphibole							
	Core			*Transitional*			*Rim*	
Oxides (wt. %)								
SiO_2	54.72	54.56	54.42	49.14	49.02	45.85	45.75	46.02
TiO_2	0.20	0.19	0.16	0.32	0.30	1.10	1.00	0.95
Al_2O_3	3.86	3.80	3.79	8.24	8.15	10.38	10.39	10.39
Fe_2O_3	0.00	0.00	0.00	0.00	0.00	0.00	0.00	0.00
FeO	8.46	8.13	8.11	11.35	11.32	11.08	11.18	11.19
MnO	0.25	0.28	0.22	0.24	0.27	0.46	0.39	0.44
MgO	17.56	17.42	17.46	14.80	14.68	13.81	13.87	13.99
CaO	11.69	11.64	11.71	11.75	11.72	11.60	11.68	11.68
Na_2O	1.74	1.76	1.74	2.75	2.67	3.34	3.33	3.35
K_2O	0.11	0.12	0.11	0.31	0.27	0.02	0.08	0.05
P_2O_5	0.00	0.00	0.00	0.00	0.00	0.00	0.00	0.00
Cr_2O_3	0.00	0.00	0.00	0.00	0.00	0.22	0.22	0.09
V_2O_5	0.00	0.00	0.00	0.15	0.20	0.00	0.03	0.00
Total	98.59	97.90	97.72	98.90	98.40	97.86	97.89	98.15
Cation proportions per 23 oxygen atoms								
Si	7.66	7.68	7.68	7.03	7.04	6.68	6.67	6.69
Ti	0.02	0.02	0.02	0.03	0.03	0.12	0.11	0.10
Al	0.64	0.63	0.63	1.39	1.38	1.78	1.78	1.78
Fe^{3+}	0.00	0.00	0.00	0.00	0.00	0.00	0.00	0.00
Fe^{2+}	0.99	0.96	0.96	1.36	1.36	1.35	1.36	1.36
Mn	0.03	0.03	0.03	0.03	0.03	0.06	0.05	0.05
Mg	3.66	3.66	3.67	3.16	3.14	3.00	3.01	3.03
Ca	1.75	1.76	1.77	1.80	1.80	1.81	1.82	1.82
Na	0.47	0.48	0.48	0.76	0.74	0.94	0.94	0.94
K	0.02	0.02	0.02	0.06	0.05	0.00	0.01	0.01
P	0.00	0.00	0.00	0.00	0.00	0.00	0.00	0.00
Cr	0.00	0.00	0.00	0.00	0.00	0.03	0.03	0.01
V	0.00	0.00	0.00	0.01	0.02	0.00	0.00	0.00

Table 6 - 9: Representative micronalyses of pyroxene from Mlakawa albitite

	Pyroxene							
Oxides (wt. %)								
SiO_2	53.61	52.98	53.42	53.88	54.19	55.29	54.78	53.95
TiO_2	0.04	0.50	0.21	0.10	0.00	0.41	0.48	0.21
Al_2O_3	3.43	3.44	3.43	3.45	3.39	3.42	0.92	1.05
Fe_2O_3	5.04	3.95	2.25	0.00	0.00	0.00	0.00	0.00
FeO	2.51	2.55	3.90	7.38	7.60	7.16	12.18	12.26
MnO	0.35	0.33	0.26	0.29	0.26	0.20	0.42	0.42
MgO	12.10	11.68	11.98	12.05	12.20	11.59	9.26	9.11
CaO	22.41	22.54	21.59	21.53	21.46	21.61	23.12	23.16
Na_2O	2.30	2.49	2.35	1.16	1.20	1.81	0.21	0.26
K_2O	0.11	0.00	0.12	0.04	0.09	0.02	0.16	0.10
P_2O_5	0.00	0.00	0.00	0.00	0.00	0.00	0.00	0.00
Cr_2O_3	0.00	0.04	0.00	0.08	0.02	0.20	0.38	0.15
V_2O_5	0.00	0.20	0.23	0.09	0.26	0.00	0.00	0.00
Total	101.90	100.70	99.74	100.05	100.67	101.71	101.91	100.67
Cation proportions per 23 oxygen atoms								
Si	1.94	1.94	1.97	1.99	1.99	2.00	2.03	2.03
Ti	0.00	0.01	0.01	0.00	0.00	0.01	0.01	0.01
Al	0.15	0.15	0.15	0.15	0.15	0.15	0.04	0.05
Fe^{3+}	0.14	0.11	0.06	0.00	0.00	0.00	0.00	0.00
Fe^{2+}	0.08	0.08	0.12	0.23	0.23	0.22	0.38	0.39
Mn	0.01	0.01	0.01	0.01	0.01	0.01	0.01	0.01
Mg	0.65	0.64	0.66	0.66	0.67	0.63	0.51	0.51
Ca	0.87	0.88	0.85	0.85	0.84	0.84	0.92	0.93
Na	0.16	0.18	0.17	0.08	0.09	0.13	0.02	0.02
K	0.01	0.00	0.01	0.00	0.00	0.00	0.01	0.00
P	0.00	0.00	0.00	0.00	0.00	0.00	0.00	0.00
Cr	0.00	0.00	0.00	0.00	0.00	0.01	0.01	0.00
V	0.00	0.00	0.01	0.00	0.01	0.00	0.00	0.00
Jd	6.22	7.39	11.00	9.07	9.60	13.24	2.41	2.48
Ac	9.86	9.27	5.92	0.00	0.00	0.00	0.00	0.00
Di+Hd	83.92	83.34	83.08	90.93	90.40	86.76	97.59	97.52

Table 6 - 10: Bulk rock major, trace, and REE compositions of representative albitite samples

	Sample No.						
	Ml1	Ml2	Ml3	Ml4	Ml5	SAL 03-17	Abo8
Oxides (wt. %)							
SiO_2	64.60	63.70	65.00	64.00	65.00	64.63	68.52
TiO_2	0.02	0.01	0.10	0.15	0.01	0.01	0.18
Al_2O_3	19.60	19.48	18.43	19.50	19.16	20.74	18.70
Fe_2O_3	0.15	0.43	0.23	0.33	0.03	0.34	0.11
MnO	0.00	0.00	0.01	0.01	0.01	0.01	0.01
MgO	0.87	0.78	0.15	0.10	0.02	0.37	0.03
CaO	1.14	1.10	1.12	1.00	0.95	0.90	1.87
Na_2O	11.02	11.81	11.30	10.30	9.70	9.45	10.30
K_2O	0.05	0.06	0.04	0.04	0.06	1.22	0.14
P_2O_5	0.07	0.07	0.03	0.07	0.04	0.20	0.01
BaO	0.03	0.03	0.03	0.03	0.03	1.29	0.24
SrO	0.05	0.06	0.05	0.05	0.05	nd	nd
LOI	1.40	0.50	0.50	0.50	0.00	nd	nd
Total	100.00	100.29	99.90	100.77	100.06	99.10	100.01
A/NK(molar)	1.08	1.00	0.99	1.14	1.20		
A/CNK(molar)	0.97	0.91	0.89	1.03	1.07		
Trace (ppm)							
Cr	7.00	10.00	15.00	7.00	8.00	9.26	nd
Ni	2.00	5.00	3.00	2.00	4.00	nd	nd
Co	2.00	2.00	2.00	2.00	2.00	0.21	nd
Zn	1.00	1.00	1.00	1.00	1.00	1.57	nd
Sc	3.00	6.00	4.00	6.00	7.00	nd	nd
Ga	11.00	10.00	8.00	15.00	9.00	17.70	nd
V	3.00	5.00	4.00	6.00	7.00	nd	10.00
Pb	7.00	6.00	8.00	9.00	10.00	3.24	nd
Yb	3.00	1.00	4.00	5.00	2.00	0.07	nd
U	0.01	0.01	0.01	0.01	0.01	0.52	1.40
Th	8.00	10.00	7.00	8.00	14.00	0.48	57.90
Hf	0.70	1.00	0.50	0.50	1.00	0.04	nd
REE (ppm)							
La	39.00	41.00	50.00	45.00	42.00	0.69	82.70
Ce	65.00	70.00	75.00	68.00	70.00	1.83	198.00
Pr	5.00	6.00	8.00	6.00	5.00	0.23	23.00
Nd	17.00	19.00	15.00	14.00	13.00	0.97	87.60
Sm	2.00	4.00	2.00	3.00	2.00	0.23	14.50
Eu	0.20	0.20	0.20	0.20	0.20	0.06	1.10
Gd	2.00	3.00	2.00	4.00	3.00	0.22	6.10
Tb	0.10	0.20	0.10	0.20	0.30	0.03	0.60
Dy	3.00	4.00	1.00	4.00	2.00	0.16	2.70
Ho	0.80	1.00	0.50	0.60	1.00	0.02	0.50
Er	1.70	1.40	1.70	1.60	1.40	0.08	1.40
Tm	0.20	0.10	0.20	0.25	0.23	0.01	0.30
Yb	0.90	1.30	1.20	1.30	1.40	0.07	1.20
Lu	0.40	0.30	0.40	0.30	0.20	0.01	0.30

Research public activity

Peer-reviewed papers

Mohammad Y. O., Maekawa, H. and Lawa, F. A. 2007. Mineralogy and origin of Mlakawa albitite from Kurdistan region, northeastern Iraq. *Geosphere*, 3, 624-645.

Aqrawi, A. M. Elias, M. E.,and Mohammad, Y. O., 2007. Oxygen and hydrogen isotope study of serpentinized peridotite rocks, Thrust Zone, northeast Iraq. *Iraqi Journal of Science*, 7, 13-20.

Mohammad, Y. O., Maekawa, H. Origin of titanite in metarodingite from the Zagros Thrust Zone, Iraq. American Mineralogist (in-press)

Mohammad, Y. O., Maekawa, H., and Karim, K., in review. Origin of spinel lamellae and octahedral inclusions in olivine of harzburgite from the Pauza ultramafic rocks, Kurdistan region, north-eastern Iraq. Geology. (submitted)

Non-reviewed papers

Mohammad Y. O., Maekawa, H., 2007. Serpentinite and Serpentinization events along the Iraqi Zagros Thrust Zone (IZTZ). Proceeding of Second International Conference on the Geology of the Tethys, Cairo University, P. 85-100